Spring 5-16-2018

Development of Metallic Magnetic Calorimeters and Paramagnetic Alloys of Ag and Er for Gamma-Ray Spectroscopy

Linh N. Le
University of New Mexico

Linh N. Le

Candidate

Physics and Astronomy

Department

This dissertation is approved, and it is acceptable in quality and form for publication:

Approved by the Dissertation Committee:

Stephen T. Boyd , Chairperson

Robin Cantor

Francisco Elohim Becerra-Chavez

Adam A. Hecht

Development of Metallic Magnetic Calorimeters and Paramagnetic Alloys of Ag and Er for Gamma-Ray Spectroscopy

by

Linh N. Le

B.S., Physics, University of New Mexico, 2009
M.S., Physics, University of New Mexico, 2013

DISSERTATION

Submitted in Partial Fulfillment of the
Requirements for the Degree of

Doctor of Philosophy
Physics

The University of New Mexico

Albuquerque, New Mexico

July, 2018

Dedication

To my family, for their love, support, and encouragement.
To my friends, for all the long nights with laughs and tears.
To caffeine, because life and science cannot happen without it.

"Sometimes science is a lot more art than science. A lot of people don't get that."
– R. Sanchez

Acknowledgments

I would like to thank my advisor, Professor Stephen Boyd, for taking a chance on me and for his support throughout this degree. My lab work would not have been possible without my other lab mates. In no particular order, a big thanks goes out to: Felix Jaeckel, Arianna Pregenzer-Wenzler, Kyle Martin, Emran Quassim, Mike Hasselbeck, Skylar Scott, Randy Lafler, Behshad Roshanzadeh, and Ruslan Hummatov.

I would also like to thank our various collaborators. Dr. Robin Cantor and the entire crew at STAR Cryoelectronics, for not only for fabrication and SQuID support, but for also making me feel like I was part of the family. Dr. Stephan Friedrich and his team at LLNL for the MPMS measurements and discussions that were crucial to the work. Last, but not least, the UNM machine shop: John DeMoss, Anthony Gravange, and Robert Chavez, for their support not only in manufacturing of components but for great jokes and conversation as well.

A big shoutout to the great community that is fostered in the physics department. Having the students, both graduate and undergraduate, and the professors so close builds a sense of camaraderie and a support network that is invaluable in not only school, but throughout life.

Special thanks to the Defense Threat Reduction Agency (DTRA) and the National Nuclear Security Administration (NNSA) for funding the project. Special thanks also goes out to David Petersen, Arden Dougan, for their help and support.

Development of Metallic Magnetic Calorimeters and Paramagnetic Alloys of Ag and Er for Gamma-Ray Spectroscopy

by

Linh N. Le

B.S., Physics, University of New Mexico, 2009
M.S., Physics, University of New Mexico, 2013

Ph.D, Physics, University of New Mexico, 2018

Abstract

A Metallic Magnetic Calorimeter (MMC) is a cryogenic calorimetric particle detector that employs a metallic paramagnetic alloy as the temperature sensor material. MMCs are used in many different applications, but this work will focus on their uses in high energy resolution γ-ray spectroscopy. This technology is of great interest to the field of Nuclear Forensics and Nuclear Safeguards as a non-destructive assay for isotopic analysis of nuclear samples. The energy resolution of MMCs is an order of magnitude higher than the benchmark High Purity Germanium (HPGe) detectors that are currently used in the field and MMCs are also poised to outperform the current leading microcalorimeter, the Transition Edge Sensor (TES). This dissertation

will cover the work in development of paramagnetic alloys of Ag and Er as the sensor material, and testing of two generations of devices.

The heart of the MMC is the paramagnetic sensor material. The workhorse paramagnet for MMCs is currently an alloy of Au and Er. Although Au:Er is a high performing alloy, it starts to falter at the temperatures below 100 mK which are desirable to maximize the performance of the MMC. Au has a nuclear electric quadrupole moment, which at low temperatures, has its energy levels split by the radial electric fields created by the Er ions. This effect causes the specific heat of the alloy to increase as temperature is lowered, which diminishes device performance. A promising alternate paramagnet is an alloy of Ag and Er. Ag, with both naturally occuring isotopes having a nuclear spin of $I = 1/2$, does not have a nuclear electric quadrupole moment. A technical challenge to working with Ag is that it has such a high affinity for oxygen that the usual method of creating Au:Er alloys may not be sufficient for Ag:Er. Much greater care has to be taken in removing oxygen from the alloy, as during creation the oxygen could adversely alter the Er dopant, thus degrading performance. To combat this, a vacuum induction furnace was developed to achieve the best possible control over synthesis process parameters. Description of the new furnace and test results from a successful synthesis of a Ag:Er alloy are discussed.

The other half of the MMC is a high-performing Superconducting Quantum Interfence Device (SQUID) magnetometer. In previously reported devices, it was standard to have the sensing coil, magnetizing circuit, and paramagnet be on a separate chips from the SQUID magnetometer. The approach taken at UNM has been to integrate the SQUID magnetometer and paramagnetic sensor onto a single chip. Having an integrated device increases the performance of the MMC, at the cost of a more difficult fabrication process. Two exploratory wafers of magnetometers have been fabricated and tested for use as MMCs. The first wafer is a set of exploratory two-pixel devices,

varying almost every aspect of the device to search for optimal device parameters. The second wafer consists of 14-pixel MMC arrays. A process of electroplating gold absorbers to the devices that now contain sensitive SQUIDs has been developed, using a two-mold system to define the legs and body of the absorbers. An initial Fe-55 spectrum from one of the new arrays is shown as a proof of concept measurement.

Contents

List of Figures

Glossary

ADR	Adiabatic Demagnetization Refrigerator
AWG	American Wire Gauge
CPA	Chromium Potassium Alum
DMSO	Dimethyl Sulfoxide
FAA	Ferrous Ammonium Alum
HPGe	High Purity Germanium Detector
KID	Kinetic Inductance Detector
MMC	Metallic Magnetic Calorimeter
PCB	Printed Circuit Board
PECVD	Plasma Enhanced Chemical Vapor Deposition
PPM	Parts Per Million
Piranha	Chemical etchant - 3:1 H_2SO_4:H_2O_2
PTR	Pulse Tube Refrigerator
RIE	Reactive Ion Etch

RTU	Ready to Use
RRR	Residual Resistivity Ratio
STJ	Superconducting Tunneling Junction
SQUID	Superconducting QUantum Interference Device
TES	Transition Edge Sensor
TVS	Transient Voltage Suppressor
UNM	University of New Mexico
XGV	Exchange Gas Volume

Chapter 1

Introduction

This dissertation will cover work done on the development and construction of Metallic Magnetic Calorimeter particle detectors (MMC) for use in recording high energy resolution γ-ray spectra from radioactive sources. These detectors, which are operated at cryogenic temperatures, precisely record the energy of captured x-rays and γ-rays, in order to determine the composition of the emitting material. This technology is of great interest to the fields of nuclear forensics and nuclear safeguards, as high energy resolved γ-ray spectra of radioactive sources can be used to determine the isotopic composition of a sample non-destructively. The design, construction, and testing of two generation of devices will be discussed along with an induction furnace system created for the fabrication of paramagnetic sensor alloys of Ag and Er.

1.1 Motivation: High Resolution Spectroscopy

Ascertaining the isotopic content of a sample of nuclear material is of extreme importance to the cataloging and control of fissile materials. A measurement of great

interest and importance is the ratio of Pu-239 to Pu-240 within a radioactive sample. Pu-239 is created as a byproduct in nuclear reactors, while Pu-240 is created when Pu-239 absorbs a neutron and does not fission. Since Pu-240 is prone to spontaneously fission, it is not fit for use in weapons, as it may cause them to detonate prematurely. Due to the volatility of Pu-240, material that is intended for weapon creation spends less time in a nuclear reactor than material that is meant as fuel. Weapons grade plutonium is therefore, typically 93% Pu-239 [7].

The highest resolution technique for determining the isotopic concentration of a sample is mass spectrometry. Here, the sample is chemically separated, ionized, then accelerated through a magnetic field to measure the charge-to-mass ratio. The major drawbacks of using mass spectrometry are samples being consumed during the process, and the high expense and time required, up to a week, to gather results [8]. These complications have pushed for the use of non-destructive assays (NDA).

An alternative NDA that alleviates the high cost and long wait times of mass spectrometry is γ-ray spectroscopy. This technique can produce results in about 24 hours without the need to destroy the sample during measurements. γ-ray spectra are used to identify the isotopic composition of samples by detecting the unique energy signature of each radioisotope's decay products. These signatures, called lines, are then compared to each other in order to find isotopic ratios. In order to obtain precise ratios, it is important to compare lines that are close in energy. Lines that have vastly different energies would experience a differing amounts of self shielding, which would introduce a systematic error to the measurement.

The benchmark detector used in nuclear forensics and safeguards for γ-ray spectrometry is high-purity germanium (HPGe). This detector consists of a purified germanium crystal which is n and p doped on two opposite sides, and held between two electrodes in a reverse biased diode configuration. γ-ray impacts on the crystal create electron-hole pairs, which are collected by the electrodes. The quantity of

electron-hole pairs collected is proportional to the energy of the absorbed γ-ray, thus energy can be estimated from the electrical current measured by the detector. HPGe detectors can be made with a large collection area, on the order of cm^2, have fast count rates, about 50 kCounts/s, and are cooled with liquid nitrogen, avoiding the need for complex cryogenics.

Even though HPGe is a successful NDA, the technology has a fundamental limitation: an energy resolution floor. HPGe detectors are non-equilibrium detectors that attempt to collect as many electron-hole pairs as possible, before that energy decays into forms not accessible to this detection scheme. The generation of electron-hole pairs only accounts for 1/3 of the total energy of the particle [9]. Statistical fluctuations of the electron-hole pair production, from event to event, also produce a fundamental constraint on the resolution. This restraint, called the "Fano Limit", causes the energy resolution to take the form

$$\Delta E_{\mathrm{FWHM}} = 2.36\sqrt{\epsilon_0 E_\gamma F} \tag{1.1}$$

where ΔE_{FWHM} is the full width at half maximum of the energy resolution, ϵ_0 is the average energy per ionization, 2.9 eV, E_γ is the energy of the original γ-ray, and F is the Fano Factor, which for Ge at 77 K is about 0.1. A HPGe detector operating at liquid nitrogen temperatures, detecting a 100 keV γ-ray, would have an maximum energy resolution of 400 eV, which would be insufficient to distinguish isotopes of Pu.

The need to detect lines that are very close in energy has pushed for the development of detectors with higher energy resolution. In order to increase energy resolution and reduce statistical variations, more of the particle's energy needs to measured. Instead of detecting only one mode of particle-matter interaction, such as the production of electron-hole pairs, the entirety of the particle's energy can be

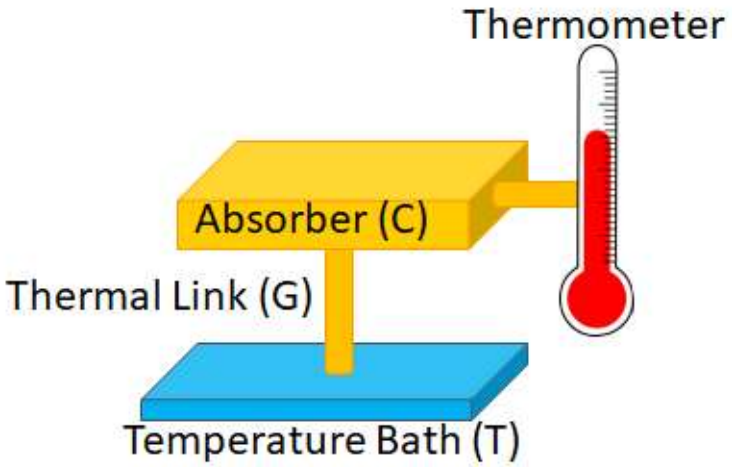

Figure 1.1: A schematic view of a calorimeter. The absorber with heat capacity C, in gold, is in strong thermal contact to a thermometer. Both the absorber and thermometer are attached to a temperature bath of temperature T, through a weak thermal link with a conductance of G. An absorbed particle will cause a temperature rise in the absorber, which is recorded by the thermometer.

allowed to completely thermalize and the entire energy can be measured as a change of temperature of the absorber that intercepted the particle. This kind of detector is called a calorimeter, and forms the focus of the work in this dissertation.

A calorimeter consists of an absorber in strong thermal contact to a thermometer and a weak thermal link to a thermal bath, as seen in Figure 1.1. When a particle impacts the absorber, the temperature of the absorber will rise. By measuring this temperature change, the energy of the particle can be calculated from

$$E_{\text{particle}} = mC_{\text{total}}\Delta T \tag{1.2}$$

where m is the mass of the absorber, C_{total} is the specific heat of both the absorber and the thermometer, and ΔT is the change in temperature measured by the thermometer.

To maximize the amount of signal detected, a large ΔT is desired. This can be achieved by decreasing the mass of the absorber and using absorber material with a small specific heat. The specific heat of a metal, which is the usual choice for γ-ray absorbers, is a combination of the lattice vibrations and energy states of the electrons. These specific heats are temperature dependent and take on the form of:

$$C_{Metals} = \gamma T + \beta T^3 \tag{1.3}$$

Where γT is the electronic specific heat and βT^3 is the phononic specific heat [10]. γ is the Sommerfeld Constant which depends on the Fermi Energy and β is a constant that depends on the Debye Temperature. For room temperature, the phononic contribution dominates, but below 1 K, where all of the detectors operate, the electronic contribution dominates. As the specific heat of these absorbers falls linearly with the temperature, it promotes these detectors to be operated at lower and lower temperatures.

By going to low temperatures and using very small absorbers, these cryogenic microcalorimeters have proven to be a technique that can non-destructively resolve the closely spaced lines that HPGe cannot. The trade-off for this higher energy resolution are the following:

1. Smaller collection areas, due to small absorbers
2. Slow count rates, to allow thermalization
3. Complex cryogenics, to achieve miliKelvin temperatures

To overcome items 1 and 2, these detectors are assembled into an array. Stacking several small detectors side by side allows the collection area to be much larger than

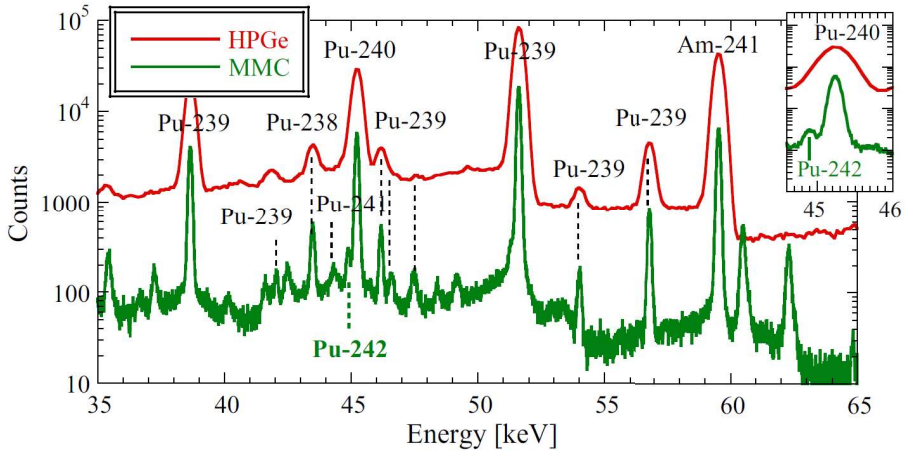

Figure 1.2: Two γ-ray spectra of the same radioactive source, taken with a HPGe detector (Top-Red) and an MMC (Bottom-Green) respectively. The MMC resolves much more detail than the benchmark HPGe detector. The inset shows the MMC resolving the Pu-242 line that is lost in the HPGe plot. Figure adapted from Bates *et al.* [1].

any individual small absorber. The use of multiple detectors also allows more events to be recorded in aggregate, allowing the array to have a high count rate, even if each individual device is slow.

Figure 1.2 shows two γ-ray spectra of a mixed Pu sample, taken with a HPGe detctor (in red) and with an MMC (in green). The MMC spectrum shows much more detail that the HPGe spectrum does not resolve. The inset in the upper right corner demonstrates the MMC resolving a Pu-242 line that is completely lost in the HPGe spectrum.

1.2 Brief History of Microcalorimetry

In order to give some overall context to the work in this dissertation, a brief history of cryogenic particle detection will be provided. This history will be directed

towards thermal detectors, highlighting the "arms race" between two rival technologies: Transition Edge Sensors and Metallic Magnetic Calorimeters.

In 1974, Niinikowski published the first data of a thermistor at cryogenic temperatures, responding to cosmic rays impinging on it [11]. The use of cryogenic calorimeters gained more traction after 1984, with the work of McCammon, Moseley, and Mather, establishing the theory of these detectors and the feasibility of their use [12].

Initial work with cryogenic calorimeters relied on resistive semiconductor thermistors for readout. Doped germanium was found to be a suitable material all the way down to 1 K, and by 1961, the technology had matured enough to create a low noise thermometer at liquid helium temperatures [13]. Although a working thermometer was created, the difficulty of fabricating these thermistors creates problems with their uniformity and hinders their optimization towards certain problems [14], encouraging the use of other technologies at low temperatures.

Two alternative, high precision techniques for cryogenic temperature measurement are to monitor the sharp rise in the resistance of a superconducting thin film across its transition temperature [2] and the measurement of the change in magnetization of a paramagnetic material in an applied magnetic field [3].

The first technology is called a Transition Edge Sensor (TES). The detector uses a superconducting thin film which is electrically biased within its superconducting-to-normal transition temperature. In this region, any small change in temperature of the film will cause a large change in its electrical resistance, as shown in Figure 1.3. The sharp change in resistance allows a very precise measurement of the temperature change. This technology is quite old, the first microcalorimeter employing a TES being created in 1949 [15] to measure alpha particles at sub-Kelvin temperatures. TESs did not gain much traction for use in microcalorimetry, as reading the small

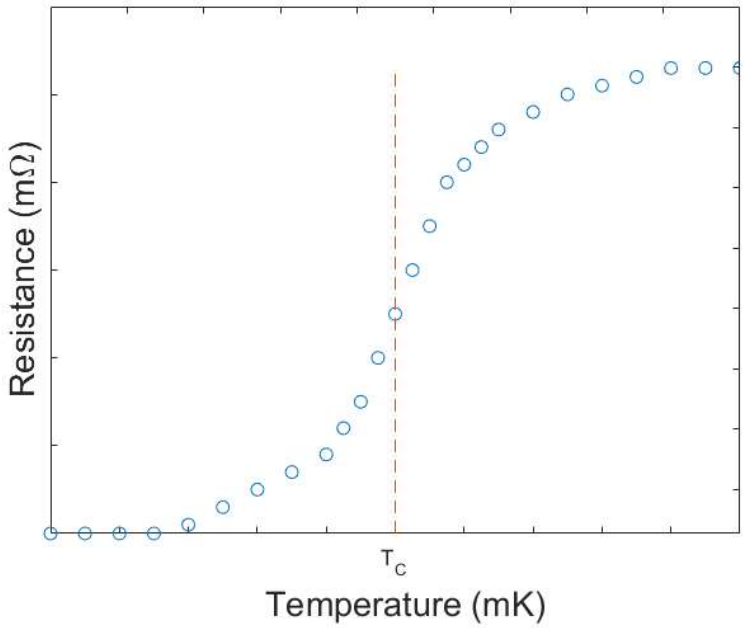

Figure 1.3: A sketch of typical behavior of the electrical resistance a superconducting thin film near its superconducting transition temperature. The sharpness of the transition allows films that are biased to stay within the transition to be used as very sensitive thermometers. Image adapted from Iwrin *et al.* [2].

change in resistance was quite difficult, until 1990, when the TES was paired with superconducting quantum interference devices (SQUIDs) for readout [16].

To prepare a TES for measurements, it is cooled below its transition temperature, then a current is applied to heat the TES to stay within the transition temperature range. The temperature is kept stable by balancing Joule heating from the applied current to the cooling of the film to the bath. TESs that are current biased suffer performance degradation to fluctuations in the bath temp and the positive feedback of the joule heating can cause thermal runaway of the system. These problems were solved in 1995 when Irwin *et al.* switched to a voltage bias scheme that creates a negative thermal feedback loop in the TES [17]. With this setup, when the resistance of the film increased, the voltage bias caused the current to drop, casing the TES to be self-regulating, and preventing thermal runaway.

The second technology, which is the main focus of this dissertation, is the use of a paramagnetic system to measure the temperature. Placing a paramagnetic system into an external magnetizing field will polarize the internal magnetic moments. Any change in the temperature will result in a change of the magnetization of the system. Since this magnetization is a function of the temperature of the paramagnet, a precise measurement of this magnetization can be used to measure the temperature. Inorganic paramagnetic crystals have been used in high resolution thermometers for temperatures below 0.1 K since the 1970's [18], but it wasn't until 1988 that Bühler and Umlauf published the first paper describing a cryogenic particle detector using a paramagnetic crystal, Y(Er)Al-garnet at 350 mK, readout by a very sensitive SQUID magnetometer [19].

The Y(Er)Al-garnet crystal used by Bühler and Umlauf had a thermal response time of 500 ms, much too slow to be used in a practical detector. To try to solve this slow response, Bandler *et al.* investigated the use of a metallic paramagnetic system in 1993 [20]. Their calculations of erbium doped gold lead to the conclusion that magnetization response times on the order of microseconds should be possible. A test detector was constructed, using a paramagnetic metal alloy of palladium doped with iron. Their experimental system was able to achieve response times on the order of 100 microseconds, an improvement of three orders of magnitude over the dielectric crystal used by Bühler and Umlauf.

The 2000's saw rapid development of both the TES and MMC. It was during this time that MMC capabilities improved to be on par with the TES. In 1999, Adams *et al.* published the first paper describing a paramagnetic calorimeter using gold doped with 600 parts per million of erbium as the sensor material [21]. This sensor was able to resolve 6 keV x-rays with an energy resolution of 90 eV FWHM. In 2001, a Mo/Cu TES created by Hilton *et al.* was able to resolve 6 keV x-rays with a FWHM of 4.5eV [22]. TESs dominated the field, reporting a resolution of 2.38 eV FWHM

in 2005 [2], with the paramagnetic approach only starting to catch up in 2009 with a resolution of 2.7 eV FWHM [23].

The paramagnetic approach finally broke through and in 2014 a detector with the best energy resolution to date was reported. Kempf *et al.* used a paramagnetic detector with erbium doped gold to measure a 6 keV X-ray with an energy resolution of 1.6 eV FWHM [24]. The paramagnetic approach, which had promised to surpass the TES in resolution, had pulled to the forefront of energy resolution. The work in this dissertation continues on this trend to improve the MMC and push the boundaries even further. As described in the next chapter, the detection physics of MMCs may create important advantages for some applications.

1.3 Dissertation Outline

This dissertation follows the work in developing MMCs at the University of New Mexico. The main topics covered will be the creation of a induction furnace system to fabricate paramagnetic alloys of Ag and Er and the fabrication and testing of a first generation of magnetometer devices that combine the paramagnetic sensor with the SQUID readout onto a single chip and the fabrication and testing of a second generation of devices which are 14-pixel MMC arrays.

Chapter 2 will review calorimetry, the physics of MMCs, and comparison of other detectors. Chapter 3 will describe the vacuum induction furnace, created for the fabrication of paramagnetic alloys of Ag and Er, with test results of a sample produced in the system. Chapter 4 will be a description of the microfabrication layers used for the creation of both generation of devices, including discussion of the two-mold setup used to electroplate Au absorbers onto the MMCs. Chapter 5 will outline the first generation of devices, including design features and initial performance. Chapter 6 will outline the second generation of devices, which are 14-pixel MMC arrays,

including an initial Fe-55 spectra.

Chapter 7 will describe the testing equipment, including the cryostat, ADR, and device testing setup. Chapter 8 will conclude the dissertation, with discussion and future work.

Chapter 2

Physics of Microcalorimeters

2.1 Overview

This chapter will describe the physics that governs the performance and operation of microcalorimeters. There will be some discussion between the differences of non-thermal and thermal devices with a more detailed comparison between Metallic Magnetic Microcalorimeters and Transition Edge Sensors, which are both thermal detectors. Special focus will be given to Metallic Magnetic Microcalorimeters, specifically the paramagnetic sensor material.

2.2 Thermal vs Non-thermal Detectors

There are two major classes of devices that are being used for particle detection: thermal and non-thermal devices. Non-thermal devices rely on secondary effects of a particle impact, such as ionizations or the creation of quasi-particles, to measure the energy of the incident particle. Notable detectors in this class are: High

Purity Germanium (HPGe), scintillators, superconducting tunnel junction devices (STJ) and kinetic inductance detectors (KID). In scintillators and HPGe, an incoming particle ionizes the detector material as it passes through, creating electron-hole pairs, as in the case with HPGe, or low energy photons, as in the case with scintillators, which are then amplified and detected [25]. The STJ detects quasi-particles created by particle impacts. These quasi-particles tunnel across a superconducting-insulator-superconducting barrier in a number that is proportional to the particle energy [26]. The KID monitors the resonance frequency and Q of a superconducting L-C tank circuit operating at microwave frequencies. When a particle impacts one of these superconducting elements, it changes its kinetic inductance and damping, which changes the resonance peaks in the microwave circuit [27].

The second device class, which is the main focus of this dissertation, are thermal detectors. After a particle impact, many different processes can occur, such as nuclear recoil, electron-hole pair creation, and other quasi-particle generation. Thermal detectors allow all these different processes to resolve and thermalize before a measurement is performed. The end measurement is the total change in temperature of an absorber that stops the incoming particle, which recovers the highest energy resolution at the cost of waiting for all the processes to complete. The two major technologies that will be discussed here are the Transition Edge Sensor (TES) and the Metallic Magnetic Microcalorimeter (MMC). The TES uses a superconducting film, biased near its superconducting transition temperature, that measures any change in temperature of the absorber as a change in the resistance of the film [2]. An MMC uses a paramagnetic alloy which is polarized in a small external magnetic field. A change in temperature of the absorber is reflected as a change in magnetization of the paramagnet, which is detected with a magnetometer.

2.2.1 Thermal Detector Energy Resolution Limits

The fundamental energy resolution of thermal detectors is limited by the heat capacity and temperature of the detector. Thermal detectors allow any deposited energy is to come to thermal equilibrium before a measurement is made. This allows the fundamental limits of measurement accuracy to be be calculated from first principles.

Consider the model of a microcalorimeter, shown in Figure 1.1, that has an absorber with heat capacity C, with an internal energy E, that is in thermal contact with a temperature bath T. If the measurement of the energy follows Gaussian statistics, then the variance of this energy measurement is

$$\sigma_E^2 = \langle E^2 \rangle - \langle E \rangle^2 \tag{2.1}$$

where $\langle E \rangle$ is the expectation value of the energy E which is defined as

$$\langle E \rangle = \frac{\sum_i E_i P(E_i)}{\sum_i P(E_i)} \tag{2.2}$$

where $P(E_i)$ is the probability that the system is in the energy state E_i. For a thermodynamic system at temperature T, this probability takes on the form of

$$Z = P(E_i) = \sum_i e^{-\frac{E_i}{k_B T}} \tag{2.3}$$

where k_B is Boltzmann's Constant. This probability is in the same form as the partition function, Z, from statistical mechanics. For simplicity, Z will be used going forward.

Equation 2.2 can be simplified with the definition of Z as

$$\langle E \rangle = \frac{1}{Z} \sum_i E_i e^{-\frac{E_i}{k_B T}} \tag{2.4}$$

Notice the term inside the sum can be generated by taking a partial derivative of only the exponential term, with respect to $\frac{1}{k_B T}$. Rather than keep track of all of these fractional quantities, another substitution of $\beta = \frac{1}{k_B T}$ will be used to simplify bookkeeping. Making these substitutions

$$\langle E \rangle = -\frac{1}{Z} \sum_i \frac{\partial}{\partial \beta} e^{-\beta E_i} \tag{2.5}$$

By exchanging the partial derivative and the sum, the partition function, Z, is recovered, simplifying $\langle E \rangle$ even further

$$\langle E \rangle = -\frac{1}{Z} \frac{\partial}{\partial \beta} Z \tag{2.6}$$

and following these steps for $\langle E^2 \rangle$, it is also reduced to a similarly simple form

$$\langle E^2 \rangle = \frac{1}{Z} \frac{\partial^2}{\partial \beta^2} Z \tag{2.7}$$

A few more mathematical manipulations are needed to shape these differential forms of partition functions into physical quantities. Taking two partial derivatives of $\ln(Z)$ with respect to β generates

$$\frac{\partial^2}{\partial \beta^2} \ln(Z) = \frac{1}{Z} \frac{\partial^2}{\partial \beta^2} Z - \frac{1}{Z^2} (\frac{\partial Z}{\partial \beta})^2 \tag{2.8}$$

The first term is Equation 2.7, allowing Equation 2.7 to be rewritten in terms of a natural log. Returning to Equation 2.1 and substituting in the appropriate terms yields

$$\sigma_E^2 = \frac{\partial^2}{\partial\beta^2}\ln(Z) + \frac{1}{Z^2}(\frac{\partial Z}{\partial\beta})^2 - \frac{1}{Z^2}(\frac{\partial Z}{\partial\beta})^2 \tag{2.9}$$

Notice that the clever rearrangement of $\langle E^2\rangle$ generates a term that perfectly cancels out $\langle E\rangle^2$ leaving only the natural log term. Taking one of the derivatives yields

$$\sigma_E^2 = \frac{\partial}{\partial\beta}(\frac{1}{Z}\frac{\partial Z}{\partial\beta}) \tag{2.10}$$

The term inside the single partial derivative is a known quantity in statistical mechanics: the negative of the internal energy of a system U. Applying the chain rule, the partial derivative with respect to β can be rewritten in terms of just the temperature T

$$\sigma_E^2 = \frac{\partial}{\partial\beta}(-U) = -\frac{dT}{d\beta}\frac{\partial}{\partial T}U \tag{2.11}$$

The partial derivative of the internal energy, U, with respect to the temperature T is another physical quantity from statistical mechanics: the specific heat of the system C. With the final steps of taking the derivative of T with respect to β, making the substitution for C and taking the square root, we finally arrive at the fundamental limit. The standard deviation of the energy of a thermal detector is

$$\sigma_E = \sqrt{k_B T^2 C} \tag{2.12}$$

Where k_B is Boltzmann's Constant, T is the temperature of the calorimeter, and C is the heat capacity of the system. For particle detectors, the FHWM is usually used for energy resolution:

$$\Delta E_{\mathrm{FWHM}} = 2.36\sqrt{k_B T^2 C} \tag{2.13}$$

2.3 Comparison of MMCs to TESs

For many years, the TES has been the dominant sensor for microcalorimeter based high energy resolution γ-ray spectroscopy. This technology is mature, has shown great resolution, and has been scaled up to large arrays. The MMC, on the other hand, is a newer technology that has only recently caught up to the TES in terms of energy resolution, with large scale arrays still in development. Despite the success of the TES, it has a few fundamental restrictions that will limit its performance compared to the MMC.

As shown in Equation 2.12, as the temperature decreases, the energy resolution of the device increases. Due to the electrothermal feedback that is used to bias the TES within its superconducting transition temperature [17, 2], heat is dissipated during operation. This Joule heating pushes the practical operating temperature of the TES to around 100 mK. The MMC does not require any bias power at the sensor, so it can be operated at the base temperature of the cryostat, which for a dilution refrigerator is around 10 mK. Referring back to Equation 2.12, this shows that for equal heat capacities, the MMC will have a higher possible energy resolution.

Due to the nature of balancing a TES within its superconducting transition temperature, a particle of unusually high energy can cause the TES to transition into its normal state. The saturation of resistance both decreases the sensitivity and

introduces strong non-linearity into the response. The need to use absorbers with low heat capacity and the sensitivity of the transition range can limit the energy range of a TES. While the linear region of the paramagnetic response of an MMC does have a finite temperature range, the effective energy range of the MMC can be extended by modifying the heat capacity of the detector. Although MMCs also strive to use absorbers with small heat capacities to increase energy resolution, it is more important to match the specific heats of the absorber and the paramagnetic sensor material to maximize sensitivity. When attempting to stop high energy particles, a thick absorber is needed. These thicker absorbers have a large specific heat, but this is compensated by increasing the specific heat of the paramagnet, either by increasing the magnetic dopant or by using a larger amount of paramagnet. With this extra flexibility, MMCs can be designed to detect particles of greater energy than a TES.

In order to extract the energy of a particle, the signal from the device must be well understood. To calibrate a device, it is exposed to particles with a known energy from a standardized check source. The response to this known input is recorded and extrapolated to different energies. Since the TES is biased to stay within the sharp transition between its superconducting and normal state, its response to a particle impact is a non-linear transport phenomenon. Attempting to understand the complexity of this response in order to achieve high accuracy calibrations is an ongoing area of research itself [28, 29]. The MMC, on the other hand, relies on the change in magnetization of a system of spins, which can be modeled and understood analytically from basic principles. The MMC response can be quite linear over a very wide energy range and exhibits only a small quadratic correction at high energies, which is easily understood. This gives the MMC a simpler and more easily attained calibration curve.

In order to create a high quality array from either TES or MMC detectors, each

individual detector in the array should be identical to each other. Any non-uniformity in the devices causes the signal collected to be position dependent, since each individual pixel will behave differently, which complicates the calibration of the entire array and degrades the overall resolution. Despite success with TES arrays, the underlying physics governing the response of the devices is not fully understood. This causes each pixel to require a unique calibration, requiring complex calibration procedures [30]. The TES relies on biasing the superconducting film near its transition temperature. The transition temperature of thin films is sensitive to processing conditions such as the film thickness [31], and the different thicknesses and overlap of normal metal to superconducting metal [32], that is used in the Mo/Cu bilayer TES. The MMC uses a paramagnetic system, which is understood analytically as a thermodynamic equilibrium process. The magnetic properties are determined during the bulk fabrication of paramagnetic alloy. This alloy is sputter deposited onto the MMC at thicknesses such that the paramagnet film has properties of the bulk material. This lends itself to the creation of an array of MMCs on a single wafer that are more uniform in performance.

The MMC, although still a young technology, promises to eventually outperform the TES. MMCs are able to be operated at much lower base temperatures than the TES as there is no power dissipation from the sensor, unlike the TES that requires bias power to stay withing its transition temperature. Combined with the much simpler physics that allows more precise calibration of the devices, will enable the MMC to surpass the TES in single pixel energy resolution. The MMC relies on bulk properties of magnetism, as opposed to the sensitive nature of superconducting transition temperatures in thin films, which aid the creation of uniform devices across a wafer. This uniformity combined with the ease of calibration of the pixels will allow the construction of MMC arrays that have much better array-wide performance, compared to the TES. Finally, the ability to customize the absorber and matching paramagnetic alloy specific heats gives the MMC additional design flex-

ibility for different applications and allows the creation of detectors with excellent energy resolution over a very wide range of energies.

2.4 Physics of MMCs

The defining characteristic of an MMC is the use of a metal paramagnetic alloy as the temperature varying sensing material. In a detector, a metal paramagnetic is preferable to one made from a dielectric as the conduction electrons in the metal are coupled much more strongly to the magnetic moments, dramatically shortening the response times compared to a dielectric [20]. The paramagnet, which is strongly thermally anchored to the absorber, is placed within an external magnetic field, which polarizes the magnetic moments. When the absorber's temperature rises, the magnetic moments in the paramagnet depolarize in response, changing the magnetization of the paramagnet. This change in magnetization causes a change in magnetic flux which is coupled into a nearby SQUID. The change in flux is then read out at room temperature as a voltage signal. This technique, which has been previously used in magnetic thermometry, is extremely sensitive and can resolve temperature changes in the paramagnetic temperature to within 1 part in 10^{10} [33].

2.4.1 Magnetization of the Paramagnet

The magnetic response of a paramagnetic system can be derived from basic physical principles. Consider the simple model of a chain of N magnetic particles in 1-D, evenly spaced and non-interacting, placed in an external magnetizing field B. A Hamiltonian for the system can be written as:

$$H = \sum_i^N \mu_i B \tag{2.14}$$

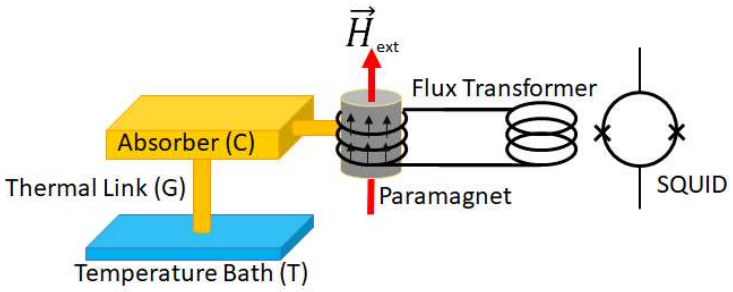

Figure 2.1: A schematic of a typical MMC. An MMC has all the same features as a typcial microcalorimeter (see Figure 1.1) except for the defining feature of the thermometer being a paramagnetic material in an external magnetic field. When a particle is absorbed, the change in temperature of the absorber will cause the spins in the paramagnet to depolarize. This change in magnetization is coupled into a SQUID through a superconducting flux transformer, where it is read out as a voltage signal.

Where for spin ½ particles, $\mu_i = \pm\mu$. Defining the partition function Z, as was previously done in Equation 2.3, the single particle partition function can be written as:

$$Z_1 = e^{\beta\mu B} + e^{-\beta\mu B} = 2\cosh(\beta\mu B) \tag{2.15}$$

Where $\beta = \frac{1}{k_B T}$ and k_B is Boltzmann's constant, is used as a substitution for convenient arithmetic. Since all of the particles are identical, the partition function of the ensemble is the partition function of the single particle raised to the N^{th} power.

The Helmholtz Free Energy, A, of the system of N particles can be obtained by raising Equation 2.15 to the N^{th} power, then taking its natural log:

$$A = -\frac{N}{\beta}\ln 2\cosh(\beta\mu B) \tag{2.16}$$

The average magnetization of the system is the change of the Helmholtz Free En-

ergy with respect to the magnetic field. Taking the partial derivative of Equation 2.16 with respect to B:

$$\langle M \rangle = N\mu \tanh(\beta\mu B) \tag{2.17}$$

This form of the magnetization is not very familiar, but taking a high temperature approximation (small β), $\tanh(\beta\mu B) \approx \beta\mu B$. Making this substitution and replacing β with $\frac{1}{k_B T}$, produces the more familiar form of the magnetization:

$$\langle M \rangle = \frac{N\mu^2}{k_B}\frac{B}{T} \tag{2.18}$$

Where the magnetization, has a $\frac{1}{T}$ dependence and is called the Curie Law with a Curie Constant, $\chi = \frac{N\mu^2}{k_B}$.

An important physics parameter to take a take note of is the ratio of $\frac{\mu B}{k_B T}$. This demonstrates the competition of the magnetizing field to polarize the spins being opposed by the thermal energy $k_B T$ attempting to randomize the spins.

2.4.2 Heat Capacity of the Paramagnet

To derive the heat capacity of the paramagnet, the model and equations formulated in the previous section can be used. Starting with the partition function found in Equation 2.15, the internal energy of the system U can be found by first taking the natural log of the partition function, Z and then taking the partial derivative of that quantity by β

$$U = -\frac{\partial}{\partial\beta} \ln Z = -N\mu \tanh \beta\mu B \tag{2.19}$$

The heat capacity is defined as the change of the internal energy with respect to temperature. Thus, taking the partial derivate of U with respect to T:

$$C = \frac{\partial}{\partial T}(-N\mu \tanh \mu B/k_B T) = \frac{N\mu^2 B}{k_B T^2 \cosh^2(\mu B/k_B T)} \tag{2.20}$$

This form of the equation is a bit cumbersome and not very enlightening, therefore a rearrangement of the equation with a substitution of the hyperbolic cosine with its exponential form yields:

$$C = Nk_B(\frac{\mu B}{k_B T})^2 \frac{e^{\mu B/k_B T}}{(e^{E/k_B T}+1)^2} \tag{2.21}$$

Which shows the $\frac{1}{T^2}$ and magnetic field dependence of the heat capacity. This effect is much more pronounced at lower temperatures where the heat capacity of the lattice is ignorable. For a metallic paramagnet, there the contributions to the heat capacity are from the electrons, as previously shown in Equation , and the magnetic moments, to give:

$$C_{MetalPM} = \gamma T + \delta T^{-2} \tag{2.22}$$

Where γT is the contribution from the electrons and δT^{-2} is the contribution from the magnetic moments [34].

2.4.3 Paramagnetic Sensor Material

The paramagnetic material of choice for MMCs is a metal base, gold or silver, that is lightly doped with the rare earth element, erbium. At concentrations of erbium

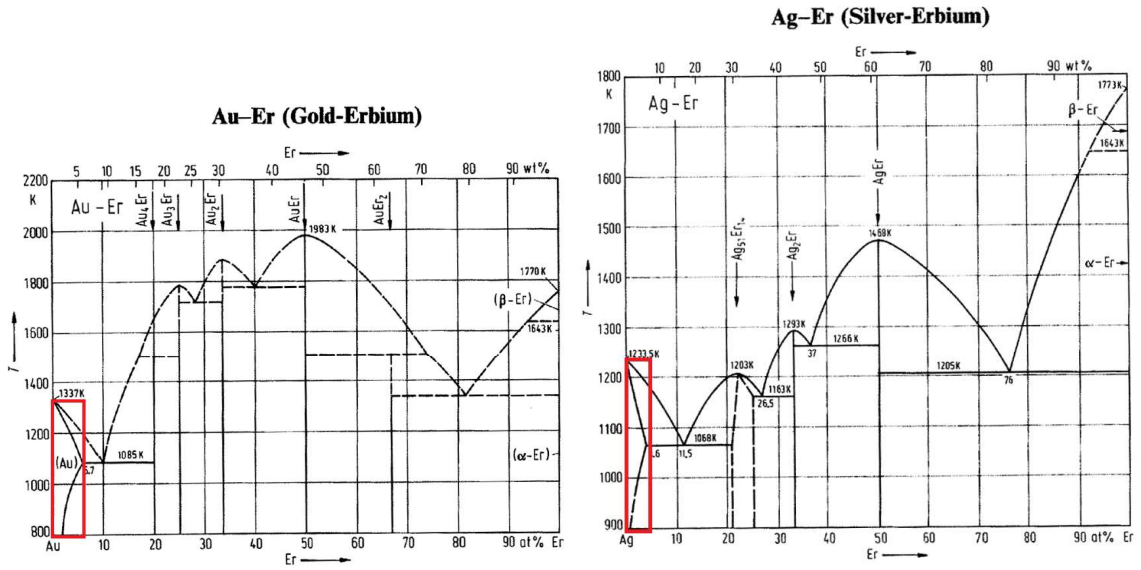

(a) Au-Er Binary Phase Diagram (b) Ag-Er Binary Phase Diagram

Figure 2.2: **Left**: Binary Phase diagram for the Au-Er system. **Right**: Binary Phase diagram for the Ag-Er system. Erbium concentration increases from left to right and temperature increases from bottom to top. The diagrams show the different intermetallic compounds and their phase as a function of temperature and erbium concentration. A triangular section is present in both diagrams, highlighted by red boxes, showing that at low temperatures and erbium concentrations below a few percent, erbium exists as a solid solution in both gold and silver.

below a couple percent, the erbium forms a solid solution within both gold and silver [5], as seen in Fig 2.2. In solid solution, the erbium atoms substitute for gold atoms at lattice sites. Erbium is a good choice for a paramagnetic dopant, as it has unpaired electrons within its $4f$ orbital shell which allow erbium to have a large magnetic moment while being shielded them from interactions with other conduction electrons within the host metal [35].

The interactions of erbium while in gold, as it pertains to MMCs, has been well studied [35]. The paramagnetic response of MMCs is able to be modeled as erbium in gold behaves very closely to a two-level system. This allows the performance of

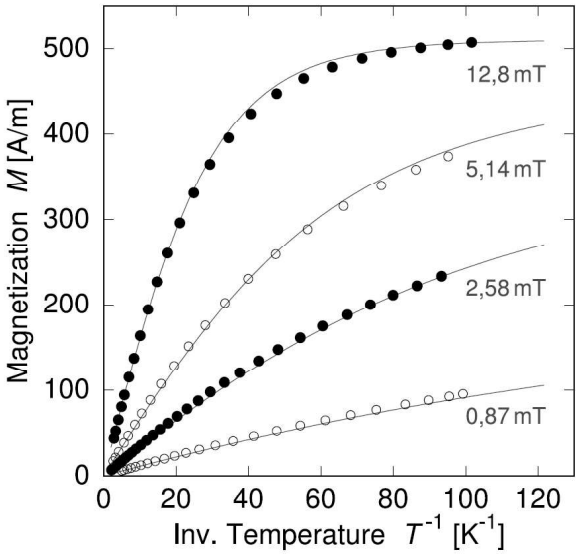

Figure 2.3: A plot of the magnetic response versus inverse temperature of a 300ppm Au:Er sample, measured at different magnetizing fields. The circles are recorded data and the solid line is the predicted value. Figure reproduced from Flesichmann *et al.* [3].

the detectors to be predicted and optimized before construction. Figure 2.3 is a plot of the magnetization of sample of Au:Er with 300ppm of enriched ^{166}Er. The magnetization of the sample is measured as a function of inverse temperature for various magnetizing fields. The dots are measured points and the solid line is the predicted response.

Au:Er vs Ag:Er

The majority of work in MMCs has been carried out with Au:Er as the paramagnet sensor material. As the performance of these detectors has improved, certain, undesirable properties of the Au:Er system have been discovered. The specific heat of Au:Er behaves as expected until temperatures below 100 mK, at which point, the specific heat starts to increase. Figure 2.4 shows a plot of the specific heat of different Au:Er samples below 100 mK. This behavior is counterproductive, as decreases

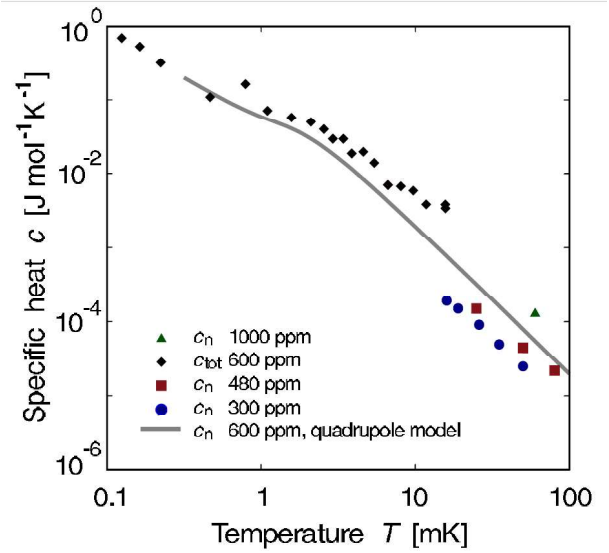

Figure 2.4: A plot of the specific heat of Au:Er samples, of varying concentrations, at temperatures below 100 mK. Notice how the specific heat increases with decreasing temperature. The solid line is a calculated specific heat for 600 ppm Er due to quadrupole splitting in Au, due to the electric field of the nearby Er atoms. Graphics reproduced from Flesichmann *et al.* [3].

in the temperatures usually decreases the specific heat, which increases the energy resolution, as seen in Equation 2.12, but this trend of increasing specific heat below 100 mK serves to partially cancel out the benefit of going to lower temperatures. Strange low temperature behavior can also be seen in the shape of pulses recorded with Au:Er MMCs. The left panel of Figure 2.5 shows normalized pulse heights taken with a Au:Er MMC at 45 mK and 6 mK. An immediate dip in the pulse height can be seen in the 6 mK pulse profile. This fast relaxation time is evidence of a second system extracting energy from the particle impacts, which is non-magnetic, is lost to detection and degrades the performance of the device.

These undesirable phenomena have been attributed to the nuclear electric quadrupole moment of gold. Natural gold is monoisotopic, with the one isotope having an intrinsic nuclear spin $I = 3/2$. Any nucleus with a nuclear spin $I > 1/2$ will have a

nuclear electric quadrupole moment. In a solid solution of erbium in gold, the erbium atoms substitute for gold atoms at lattice sites. These local erbium ions each create a radial electric field gradient, which splits the quadrupole moment of the nearby gold nuclei.

This splitting is thought to be the origin of both the high heat capacity and the fast relaxation time seen in Figure 2.5. In order to circumvent this, one strategy is to switch to a new base metal, that does not have a nuclear electric quadrupole moment. An easy first choice would be silver as both natural isotopes of silver have a nuclear spin $I = 1/2$, which does not support an electric quadrupole moment. Erbium also creates a solid solution in silver as seen in Figure 2.2, which shows that Ag:Er paramagnet can be created. Enss *et al.* has created an MMC using Ag:Er and shown that the the undesirable effects have been resolved [4]. The right portion of Figure 2.5 shows superimposed pulses, one taken with a Au:Er MMC and one taken with a Ag:Er MMC in similar conditions, demonstrating the resolution of the fast relaxation time arising from splitting of the nuclear quadrupole.

Switching to silver has a few technical downsides. First, silver has higher RKKY coupling than gold, roughly 2.6 times higher [36]. This increased coupling causes Ag:Er to underperform Au:Er at temperatures above 10 mK. Silver also has a high affinity for oxygen and erbium is a very effective reducer. During creation of the alloy, oxygen scavenged from the environment or released from the silver could cause the erbium in solution to oxidize, which in turn, will change the performance of the material. Due to this, Ag:Er should be created in a more tightly controlled environment. One large thrust of this dissertation work is in the creation of a vacuum induction furnace system to create Ag:Er paramagnet in a highly controlled atmosphere. This work will be described in greater detail in Chapter 3.

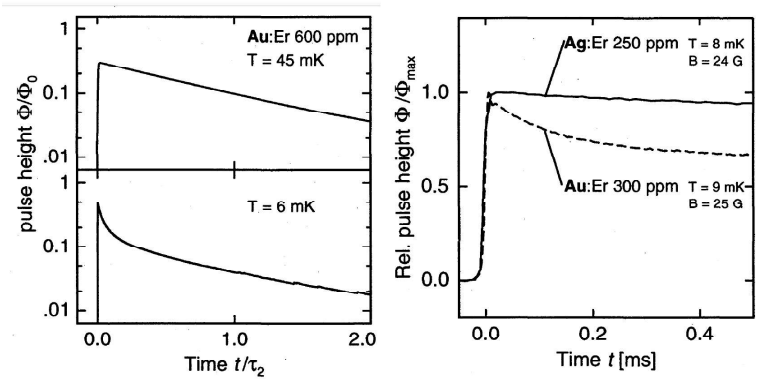

Figure 2.5: **Left**: Two plots of normalized pulse height vs relaxation time for a standard pulse taken from an MMC with 600 ppm of Au:Er. The top plot is taken at 45 mK and the bottom at 6 mK. Notice the "fast relaxation time" in the bottom plot, evidenced by the dip after the peak. **Right**: Two normalized pulses taken from two different MMCs, one with 250 ppm Ag:Er at 8 mK (solid) and one with 300 ppm Au:Er taken at 8 mK (dashed). Notice that "fast relaxation time" dip in the Au:Er pulse is not present in the Ag:Er pulse. Graphics reproduced from Enss *et al.* [4].

2.4.4 Absorber Selection

The choice of absorber for the MMCs must be weighed by the following factors: heat capacity, thermal conductance, particle stopping power, and fabrication difficulty. Dielectric and superconducting absorbers offer very low heat capacities, but have very poor thermal conductances. Low thermal conductance can cause the signal from a captured particle to become position dependent. Use of a normal metal is more desirable, as the thermal conductivity and particle stopping power can be quite high. Using the heat capacity per stopping power as a figure of merit, gold is the best choice. Gold is also widely used in microfabrication, making the implementation into MMCs straightforward.

The attenuation of incident photons into an absorber increases exponentially with the thickness of the absorber and is given by

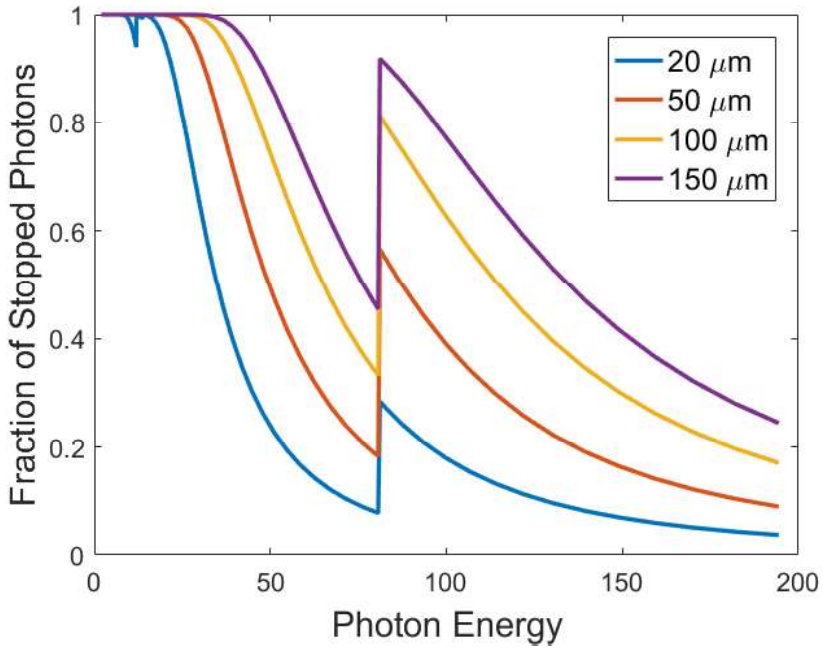

Figure 2.6: A plot the stopping power of different thicknesses of gold absorbers vs. incident photon energy. The sharp feature near 80 keV corresponds to the absorption edge of the K shell of Au.

$$\frac{I}{I_0} = e^{-\mu t} \tag{2.23}$$

Where I_0 is the incident intensity, I is the intensity after passing through the absorber, t is the thickness, and μ is the material dependent attenuation coefficient. Using this equation and a table of attenuation coefficients provided by NIST [37], absorber thicknesses can be optimized for the particles being detected. For the initial characterization of devices, an Fe-55 xray source is used, with a primary line at 6 keV. As seen in Figure 2.6, absorbers with a thickness of 20 μm are enough to stop those x-rays, but for characterization of γ-rays, an ^{241}Am source would be needed, with a characteristic line of 60 keV. At these higher energies, a 20 μm absorber would only stop 15% of the particles. The processes developed within this dissertation aim

to create absorbers of 100 μm thick, which would stop 60% of the 60 keV photons.

Chapter 3

Paramagnet Synthesis and Testing

3.1 Background

Historically, the metallic paramagnetic of choice for MMCs is gold doped with erbium, usually in concentrations of less than 0.1%. Electronic properties of erbium in gold have been studied previously and the fabrication of these alloys in has been performed in an arc melting furnace [38]. An arc melting furnace consists of a small airtight chamber that houses a water cooled copper hearth and a arc welding tip. Small quantities of the base metal and magnetic dopant are put onto the copper hearth and the chamber is closed and pumped to a rough vacuum. An argon flow is established before an electric arc is struck between the welding tip and hearth to melt the sample. Mixing and homogenization is achieved by chasing the sample with the arc and final alloy creation is accomplished by melting together multiple samples across multiple melts.

Although samples of gold and erbium created in this fashion have performed very well [3, 23, 39, 24], the control over processing conditions leaves much to be desired. Creation of a final alloy over multiple runs increases the chances of contami-

nation. The vacuum chambers employed are generally not designed for high vacuum applications, thus atmospheric cleanliness is limited. Tight control over processing conditions and environments becomes much more important when working with less inert samples, such as silver. Silver has a high affinity for oxygen [40], especially while molten. Any oxygen that is present in the molten silver, or that is scavenged from the environment, can bind to dopants, such as erbium, which can change the properties of said dopant. In order to combat this, we have developed an induction furnace system equipped that can operate under high vacuum or purified argon gas for the production of extremely clean paramagnetic alloys of both Au:Er and Ag:Er.

A great amount of care was taken to allow maximum control over the atmosphere during material processing. The system is attached to a turbopump that allows samples to be processed under high vacuum and is equipped with a heated argon purifier to allow processing under a flow of ultra pure argon. The system is designed to process enough paramagnetic alloy to create a 1" diameter sputtering target in one melt, but is flexible enough to accommodate other geometries.

3.2 Vacuum Induction Furnace Overview

The induction vacuum system was designed to be modular "system on rails" to which components can be easily added or removed. All of the components are attached to an aluminum T-slot frame, which is equipped with casters. The casters allow the system to be moved to the turbo pumping station during use, and stored away when not in use. The system has five major components: the RF induction heater, quartz tube vacuum chamber, heated argon gas purifier, rotating sample mount, and tilting frame. An overview photograph of the system is provided in Figure 3.1. A brief description of each major component will be given in the following paragraphs.

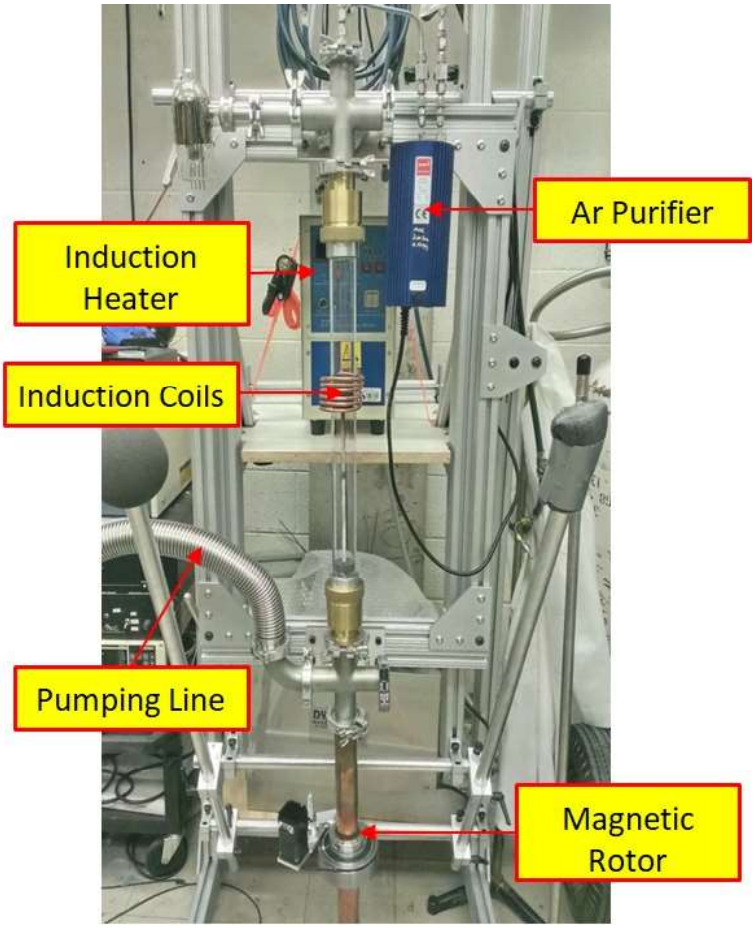

Figure 3.1: Overview photograph of the fully assembled vacuum induction furnace system. The induction heater and induction coils are centrally located, surrounding the quartz tube that acts as the vacuum chamber. Purified argon gas is delivered from the blue heated purifier located to the upper right. Samples are suspended and rotated from below by a magnetic rotor. Pumping lines attach the chamber to a turbo pumping station located to the left, out of frame.

3.2.1 Induction Heater

The heart of the system is the RF induction heater (Across International model IH15 15KW 30-80kHz). The Induction heater runs a high frequency high current through the water cooled copper coils which creates an oscillating magnetic field that can be coupled to a conductive material. The oscillating field causes a large $\frac{d\phi}{dt}$, establishing a

Figure 3.2: Close up view of the induction heater unit and the copper heating coils. A quartz tube, not pictured here, that acts as the vacuum and sample chamber is placed within the coils.

large electromotive force, which causing eddy currents to form within any conductive material placed within the coils. These currents cause Joule heating in the material, raising the temperature high enough to melt metals. Induction heating is a long range, non-contact heating scheme, allowing the coil to reside outside of the vacuum space, allowing the vacuum space to be as clean as possible.

3.2.2 Quartz Tube Vacuum Chamber

A clear, quartz tube comprises the vacuum and sample chamber. The tube shown has a 38 mm inner diameter, which is appropriate for the creation of 1" diameter sputtering targets, but different copper coil/quartz tube configuration can be used to meet different form factors. The tube is vacuum sealed by two tubular compression fittings at the top and bottom that attach to the rest of the vacuum and gas handling

Figure 3.3: Photograph of the clear quartz tube that is used as the vacuum chamber for paramagnetic alloy preparation. The tube sits within the coils of the induction heater and its non-conductive nature allows the induction power to pass into the vacuum space uninhibited. The quartz tube is sealed at both ends with brass couplings that attach to the vacuum pumping lines (below) and argon gas delivery manifold (above) via KF-40 joints.

lines with KF-40 joints.

Quartz is a useful material, as its non-conductive nature allows us to apply the induction power external to the vacuum space and its natural optical transparency allows the inspection of samples in-situ. Quartz is also highly heat resistant: able to withstand temperatures of 900° C for extended periods and temperatures above 1100° C for brief periods. The system is designed to allow the quartz tubes to be interchangeable, facilitating the cleaning of dirty tubes, replacement of broken tubes, and using dedicated tubes for different sample materials.

3.2.3 Purified Argon Delivery

Figure 3.4: **Left**: Heated argon purifier and Ar delivery manifold. Ultra high purity argon is delivered from a gas bottle to the inlet of the purifier (red arrow). The purifier removes residual gasses, such as nitrogen and oxygen, before flowing into the vacuum chamber (green arrows). **Right**: Closeup of the SAES GC50 heater argon purifier.

The induction vacuum furnace was designed to have highest possible control over processing environments. In that vein, samples can be processed in a high vacuum environment or under an atmosphere of purified argon gas. Ultra high purity (99.999%) argon gas is fed into a heated argon purifier (SAES Purifier GC-50) which reduces oxygen and nitrogen impurities in the gas to less than 10 parts per billion [41]. This ultra pure argon is continuously flowed over the sample at a rate of 40 sccm during processing.

3.3 Sample Support and Rotation

3.3.1 Graphite Susceptor with Tantalum Insert

Figure 3.5: **Left**: 1.25" diameter graphite susceptor, with a machined well to house samples. **Right**: 1.125" diameter tantalum cup stamped from 0.005" thick tantalum foil. The tantalum acts a liner between samples and the graphite crucible.

The silver sample itself does not couple very well to the induction furnace field. Therefore, in order to intercept the RF power produced by the induction heater, the silver is placed within a dedicated susceptor. Graphite is used as the susceptor material as it is non-magnetic, easily machinable, conductive, and has an extremely high melting temperature. Graphite rods are machined to fit the quartz tube and bored to house the samples being processed.

Tantalum is used a liner between the graphite and the sample material. Tantalum foil, 0.005" thick, is formed into 1" diameter cups. Sample materials are placed within these tantalum cups before being placed into the graphite crucibles. Tantalum was

chosen because it has a substantially higher melting point than any material we wish to process, does not chemically react with our sample materials, and is commercially available as a foil that is soft enough to manipulate. Platinum is also a good choice of material for the liner, but its high cost deemed it prohibitive.

3.3.2 Magnetic Support and Rotation

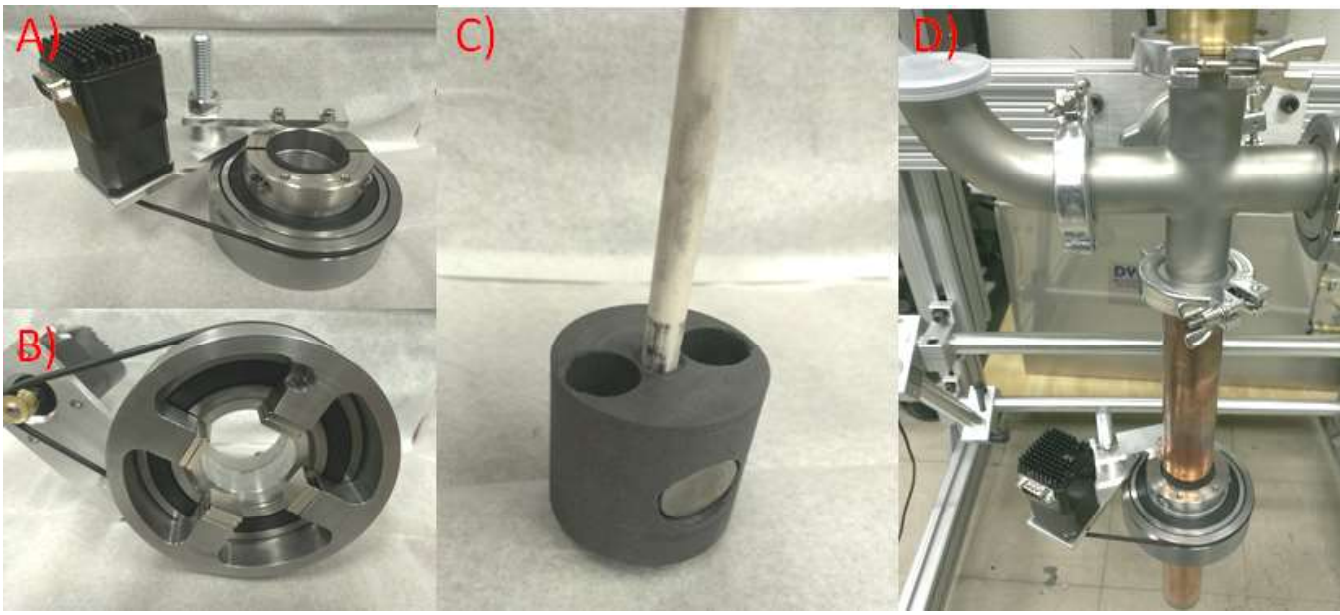

Figure 3.6: Components of the magnetic rotary feedthrough and sample support system. **A and B**: The magnetic bearing and drive motor for crucible rotation. 8 NdFeB magnets support the magnetic rotor externally of the vacuum space. **C**: Graphite rotor with iron pole piece for magnetic coupling that resides inside the vacuum space. The alumina rod supports graphite susceptor and sample from below. **D**: External view of the rotary system attached to the furnace

The susceptor and sample are mechanically supported within the vacuum space by 3' long, 0.25" diameter alumina rod. Radial centering of the rod and susceptor is achieved with graphite spacers, placed along the length of the alumina rod. These spacers not only center the rod but also act as thermal baffles to protect the less heat-

resistant components below them. The rod extends from a magnetic rotor housed in a larger copper pipe at the bottom of the system (See Figure 3.6) up into the quartz tube and into the bottom of the graphite susceptor.

External to the copper pipe is the magnetic rotary feedthrough and motor. A rotary bearing with 8 NdFeB magnets and a programmable stepper motor are attached to a large shaft collar. This collar attaches the magnetic bearing assembly to the outside of the copper pipe, allowing the magnets to hold the magnetic rotor inside the pipe in place. The rotary bearing is rotated by a drive belt propelled by a programmable stepper motor (Lin Engineering 102602), which in turn, rotates the graphite susceptor and sample. This rotation is used to homogenize molten samples in-situ, without any introduction of foreign material from a stirring arm.

3.3.3 Tilting Frame

The entire system, save the turbo pump, is built onto a structure made from aluminum T-slot framing. The T-slot design allows quick assembly and easy adjustments while also offering easy mounting points for the various components. The modularity of the system allows the addition or modification of components to accommodate different projects. The frame sits on casters that allow the system to be easily moved to the vacuum system and stored when not in use.

A novel feature of this frame is the ability to tilt it up to 30 degrees from vertical, see Figure 3.7. This tilt, combined with the rotation of the crucible, gives our samples a "cement mixer" action. In combination with the stirring effect of the induction heating field, this ensures excellent homogenization during heating. The frame tilt can be adjusted while samples are molten, allowing us to manipulate the form factor of the final sample.

Figure 3.7: Profile photographs of the support frame and system. **Left**: the system in its usual vertical position. **Right**: The system tilted to 30 degrees. The combination of tilt and sample rotation allows for a "cement mixing" action of molten samples. Yellow lines are drawn to guide the eye.

3.4 Temperature Measurement and Calibration

In order to measure the temperature of the samples, a high temperature tungsten/rhenium thermocouple was inserted into the bottom of a graphite susceptor and its temperature vs. induction heater current was measured. The thermocouple was threaded through an alumina rod with 2 channels, leaving the sensing end of the thermocouple exposed at the top. That rod was then inserted into the bottom of a susceptor to support it and bury the thermocouple within the susceptor. The bottom of the thermocouple terminated in a connector at the bottom of the quartz tube, which allowed electrical connection outside the vacuum space. The recorded temperature vs. furnace current is shown in Figure 3.8.

Due to the rotation used during sample processing, the thermocouple cannot

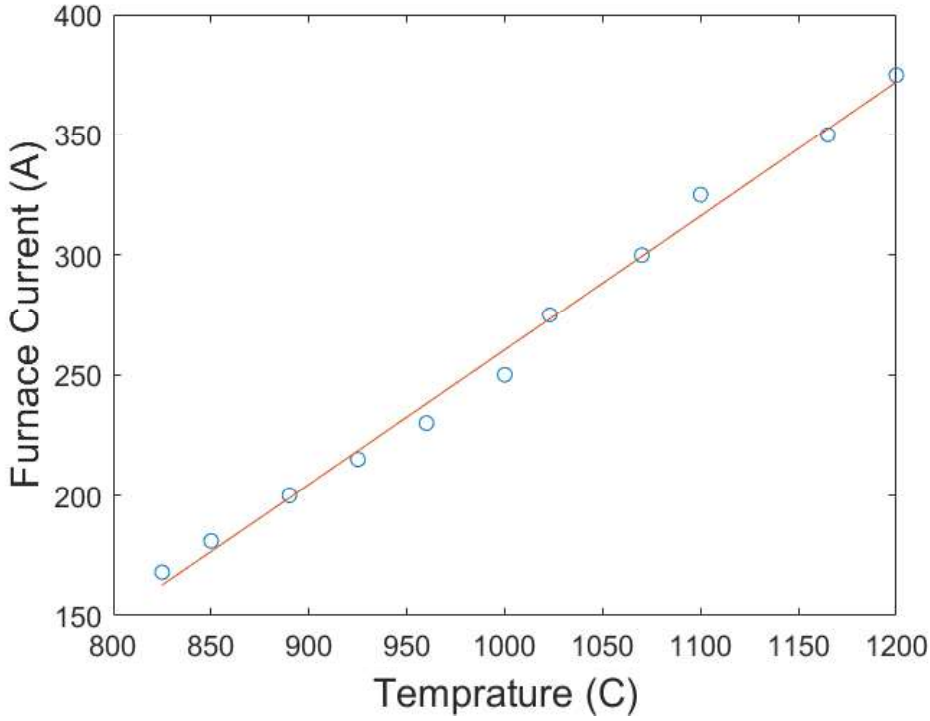

Figure 3.8: A plot of susceptor temperature vs induction heater current, taken with a tungsten rhenium thermocouple. The temperature and current trend linearly with a fit of $T = (0.5584)I - 298$, where T is the temperature and I is the furnace current.

be used in conjunction with the magnetic rotary setup as described above. A calibration curve is generated for a graphite susceptor and induction coil arrangement, then a sample is processed in that same arrangement, with the sample temperature extrapolated from the induction furnace current.

3.5 Recipe for Ag:Er

3.5.1 Prebake crucibles for cleanliness

To ensure cleanliness of the system and samples, all new tantalum cups and graphite susceptors are thoroughly cleaned before use. New tantalum cups are washed in a bath of acetone then isopropyl alcohol, before air drying. The graphite susceptors receive a more thorough cleaning. Newly machined susceptors are sonicated for 15 minutes in deionized water then in methanol for 15 minutes. After the methanol wash, they are immediately sonicated in clean, deionized water for 5 minutes before drying in a 120° C oven for 2 hours, under rough vacuum.

The susceptor and liner are assembled and go through a heating cycle in the induction furnace before any samples are added. The new parts are heated to 800° C under high vacuum for 10 mins to bake off any water and residual organics. The parts are then cooled under vacuum below 100° C before exposure to air and subsequent sample loading.

3.5.2 Silver Premelt

The base silver for the Ag:Er paramagnet is melted under high vacuum, without any magnetic dopant, to degas any trapped oxygen. 30 grams of 99.9999% pure silver pellets (Alfa Aesar) are placed into the tantalum cup, which is then placed into the graphite susceptor, then loaded into the system. The system is evacuated to a high vacuum state with the turbo pump before the application of any heating power. The sample is then slowly heated, at the minimum power of the furnace, to 800° C and held there for 10 minutes to drive off any residual moisture.

After the drying step, the sample is heated up to 1000° C to melt the silver. Once

the silver is molten, the frame is tilted to 30 degrees and the crucible is rotated at a rate of 6 revolutions per minute. This combination of tilt and rotation gives a "cement mixer" action to agitate the silver and allow any trapped oxygen to escape. The heating and stirring lasts for 10 minutes before the frame is returned to its upright position, rotation is stopped, and induction power cut. The sample is allowed to cool below 100° C under vacuum before the addition of magnetic dopants.

3.5.3 Paramagnet Melt

With the silver degassed and cooled, it is removed from the system to add in the magnetic dopant. A foil of naturally abundant erbium, 99.9% pure (Alfa Aesar), is cut and weighed out proportionally to the desired paramagnet concentration and placed on top of the clean silver. The sample is returned back to the system for the final melt. The system is pumped to a pressure $<1 \times 10^{-4}$ Torr before isolating the turbo pump and backfilling the system with high purity argon gas from a gas bottle to slightly above atmospheric pressure. Gas flow is then diverted into the heated argon purifier, which is set to flow purified argon past the sample at 40 sccm, with the excess gas being vented to atmosphere.

With purified argon flowing past the sample, the induction heater is energized and the sample is brought up to 1000° C to re-melt the silver. Although this is well below the melting point of erbium, the erbium foil dissolves into the molten silver. Once the silver completely melted, and the erbium has gone into solution, the frame is once again tilted and rotation is established. The sample temperature is now raised above 1250° C (1523 K) and held for 10 minutes. This higher temperature step is used to dissociate any high temperature intermetallics of erbium and silver, see Figure 3.9. Finer detail of these intermetallics and temperature ranges are given in a following section. After the high temperature soak, the temperature is lowered

back to 1000° C and the frame is returned to its vertical position before rotation and induction power is halted. The sample is cooled under flowing purified argon to a temperature below 100° C before extraction.

3.5.4 Shaping the Sputtering Target

Once the sample is cooled, it is extracted from the system and inspected. The tantalum cup has to be removed prior to forming of the sputtering target. The silver adheres to the cup quite strongly, necessitating the destruction of the cup to free the silver. In general, only the sides of the cup can be removed by hand, leaving the bottom intact. After hand removal of the tantalum sides, the last of the tantalum removal and final shaping of the target is done on a lathe.

The sample is held in a lathe using the pressure pads technique. A 0.75" diameter aluminum rod is held in the chuck of the lathe and a similar rod is held in the tailstock. The sample is placed axially between both rods and pressure is applied to sandwich the sample in place. Great care is taken to avoid contact of the sample with any steel tools, as iron contamination will alter the paramagnetic properties of the alloy. The sample diameter is machined down to 1" with diamond tipped tools. Once the sides have been machined, the sample can now be held in a standard brass collet so that the front and back surfaces can be planarized. This final step removes the bottom of the tantalum cup and reduces the thickness of the final target to 0.125".

3.6 Heating Strategy of Ag:Er Creation

The heating profile for the silver erbium paramagnetic alloy recipe has more subtlety than just heating to the highest melting point between the two materials. Since silver

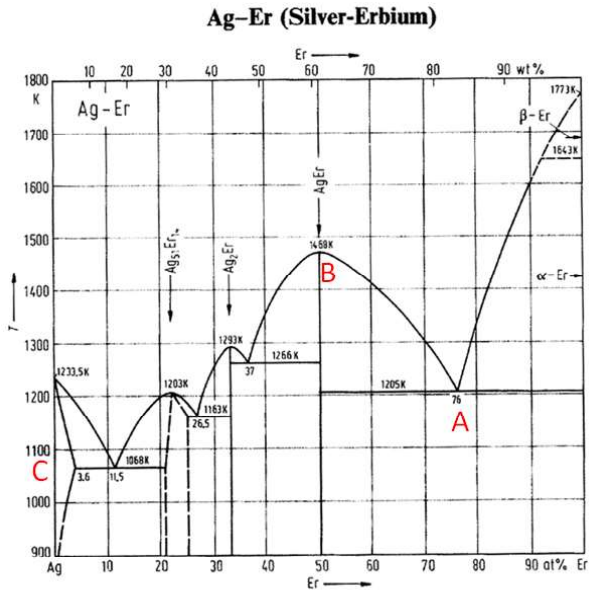

Figure 3.9: Binary phase diagram of the Ag-Er system, showing the solid and liquid states of any intermetallics between silver and erbium, as a function of erbium concentration and temperature. The solid, curved line represents the liquidus of the various concentrations of silver and erbium. Temperatures above this line indicate the mixture is completely liquid and temperatures below it are a mixture of solid and liquid. Point A is the eutectic point of silver and erbium at 1205 K (931° C). Point B is the very stable AgEr compound that is only completely liquid past 1500 K (1226° C). Point C is the solid solution phase of erbium in silver that is being targeted. Plot reproduced from Landolt and Bornstein, *Structure Data of Elements and Intermetallic Phases* [5].

and erbium have melting points of 961° C and 1529° C respectively, the seemingly obvious choice would be to increase the furnace temperature up to 1600° C to ensure the erbium is molten during processing. A huge consideration in avoiding this method is the vapor pressure of silver. The vapor pressure of silver at 1600° C is 100 times higher than it is near its melting point. At higher and higher temperatures, more silver is would be lost to vaporization. In order to reduce silver loss, which would in turn change the desired dopant concentration in the final sample, it is prudent to work at lower temperatures.

The binary phase diagram for silver-erbium, shown in Figure 3.9, shows what intermetallic compounds exists between silver and erbium as a function of erbium concentrations and temperature. The solid, curved line across the graph represents the liquidus line. At temperatures above this line, the compound exists as a liquid but below that line it exists as a mixture of solid and liquid. At 75% concentration of erbium in silver (point A), the liquidus line has a local minimum. This minimum is a eutectic point, showing us that this concentration of erbium and silver is completely liquid at 931° C, lower than both the melting points of pure silver and pure erbium. As we heat up the silver to its melting point, molten silver and solid erbium will locally create the eutectic, melting the erbium foil well below its normal melting point.

Stirring the molten material disperses the erbium from the local concentration of 75% erbium towards the desired global concentration, generally 0.1% erbium or less. As the erbium disperses, it will be locally diluted to 50%, which is point B on the phase diagram, a maximum on the liquidus line. This point shows that an intermetallic of AgEr at a 1:1 ratio is formed and that at temperatures less than 1500 K (1226° C), this is a mixture of both liquid and solid. For this reason, the entire sample must be heated above 1226° C to ensure that no solid precipitates remain and that molten erbium is free to continue to diffuse throughout the silver. After sufficient time at high temperatures with stirring, the erbium, now completely liquid, will diffuse throughout the sample to the target global concentration. The sample is then quickly cooled below the melting point of silver to solidify the sample as a solid solution of erbium dispersed in a silver matrix (point C).

Figure 3.10: Various intermediate samples created during refinement of the Ag:Er paramagnet recipe. **A)** Erbium oxide (pink) and **B)** erbium nitride (black) which led to the use of purified argon. **C)** Erbium carbide (brown) which led to the use a tantalum cup insert in the graphite susceptor. **D)** silver erbium 1:1 intermetallic (matte tan) forced the melting temperature to be above 1226° C while stirring.

3.7 Process Development and Findings

There were many alternative materials created during the development of the silver erbium paramagnetic recipe. The final product is pure silver with at most, 0.1% of paramagnetic dopant in a solid solution. Therefore, the silver is still at least 99.9% pure, and the final product should be visually indistinguishable from stock silver. During development, samples of varying colors were created, as seen in Figure 3.10, indicating improvements in the process were required. Samples that were pink or black, indicated the creation of erbium oxide and erbium nitride, respectively. This lead to the initial step of pre-melting the silver to remove any trapped oxygen and the implementation of the heated argon purifier to remove any residual oxygen and nitrogen in the argon to below 10 ppb. Brown samples arose from the creation of erbium carbide, leading to the use of the tantalum cup insert between the sample and the graphite susceptor. The final hurdle was a sample that came out with a tan, matte finish. This was attributed to the creation of the 1:1 AgEr intermetallic, which was remedied by increasing the final melt temperature above 1200° C and introducing the "cement mixer" by combing sample rotation and tilt in the frame, to homogenize the silver and erbium in-situ.

3.7.1 MPMS Analysis of Ag:Er Sample

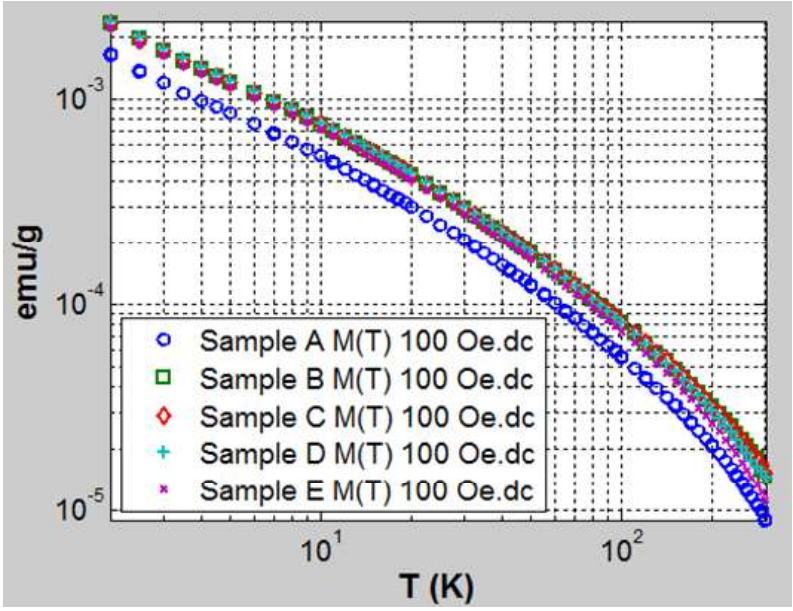

Figure 3.11: Mass susceptibility versus temperature for 5 silver erbium slugs taken at 4 T in the MPMS. Samples B, C, D, and E lie practically on top of each other, signifying good uniformity in the target. Sample A was physically smaller, thus skewing its results due to its lower mass.

After creating a sample that passed visual inspection, a more quantitative analysis was required. A silver sample with 1000 at. ppm of erbium was created specifically for measurements in a Quantum Design magnetic properties measurement system (MPMS). This instrument is not available at the University of New Mexico, so samples were sent to colleagues at Lawrence Livermore National Labs for analysis[1]. The MPMS measures the magnetic dipole moment of our samples in an external magnetic field as a function of temperature from 300 K to 2 K. Estimates of the concentration of active erbium in our samples can be derived from the magnetic response curve [35].

To create the MPMS sample, a 1" diameter by 0.125" thick sputtering target was

[1]A big thanks to Dr. Stephan Friedrich and colleagues for taking the measurements

fabricated in our induction furnace and from that, five smaller slugs were cut. The slugs, cut with electric wire discharge machining, received a quick wash in a diluted nitric acid bath to remove any surface contamination, prior to testing. Each of the slugs was placed in the MPMS and had their magnetic response to a 4 T external magnetic field recorded from 300 K to 2 K. Figure 3.11 shows the mass susceptibility versus temperature for all five samples, overlaid. The curves for samples B, C, D, and E are in very close agreement, signifying good uniformity of magnetic doping across the target. The outlier, Sample A, came from the center of the target which was physically shorter than the rest, due to a dimple left during the creation of the sample. Since this data is normalized by mass, the central sample was miscalculated due to its smaller size. Even if this aberration were real, the central region of a sputtering target does not contribute much to any films deposited from it, therefore it can be safely ruled that any discrepancy with sample A is of little consequence.

Focusing on a single sample and re-plotting the data as magnetization vs. inverse temperature, as seen in Figure 3.12, we present the data in its more canonical form. Following the work of Fleischmann *et al.* for erbium in gold at 4 T [35], we can fit the high temperature regimes and low temperature regimes of the data to extrapolate our concentration of active magnetic dopants. In the high temperature regime, the change in the magnetization versus inverse temperature follows a modified Curie Law due to the crystal field effects on the erbium, which can be expressed as the following:

$$\frac{\partial M}{\partial(1/T)} = \frac{Nc}{V}\frac{(g_\Lambda \mu_B)^2 B}{3\kappa} J(J+1) \tag{3.1}$$

where M is the magnetization, T is the temperature, $\frac{N}{V}$ number of Ag atoms per volume, g_Λ is the lande g factor, μ_B is the Bohr magneton, B is the applied magnetic field, κ is Boltzmanns constant, J is the total angular momentum and C, our fit pa-

rameter, the concentration of magnetic ions. From quantum mechanical calculations of the ground state of Er^{3+} found in the literature, the total angular momentum J is $^{15}/_{2}$ and the Lande g-factor is $^{6}/_{5}$. Fitting the slope of the highest temperature data, a concentration of 900 at. ppm of erbium in our sample is the best fit, very close to the targeted 1000 at. ppm.

The low temperature regime of the data, follows a simpler Curie Law, as some of the higher energy level splittings of the erbium ions fall out, leaving only the ground state doublet. The equation for the slope of the magnetization vs. inverse temperature is given as:

$$\frac{\delta M}{\delta(1/T)} = \frac{Nc}{V}\frac{(g\mu_b)^2 B}{3\kappa}\hat{S}(\hat{S}+1) \tag{3.2}$$

where now g=6.80 and $S = {}^{1}/_{2}$ for the doublet. A concentration of 900 at. ppm also fits the slope of the low temperature regime.

3.8 Conclusion

A vacuum induction furnace has been developed for the creation of ultra clean paramagnetic samples for use in MMCs. The furnace can process samples under high vacuum or ultra purified argon atmospheres. The unique combination of magnetic rotation and tilt of the system allows samples to be stirred at an angle, providing a "cement mixer" action that homogenizes samples without introducing any contaminates from a stir rod or other apparatus. The system described above is fitted to create samples suitable for 1" diameter by 0.125" thick sputtering targets in one operation, but is modular enough to be fitted for other form factors.

Successful samples of Ag:Er paramagnet have been created in the vacuum induc-

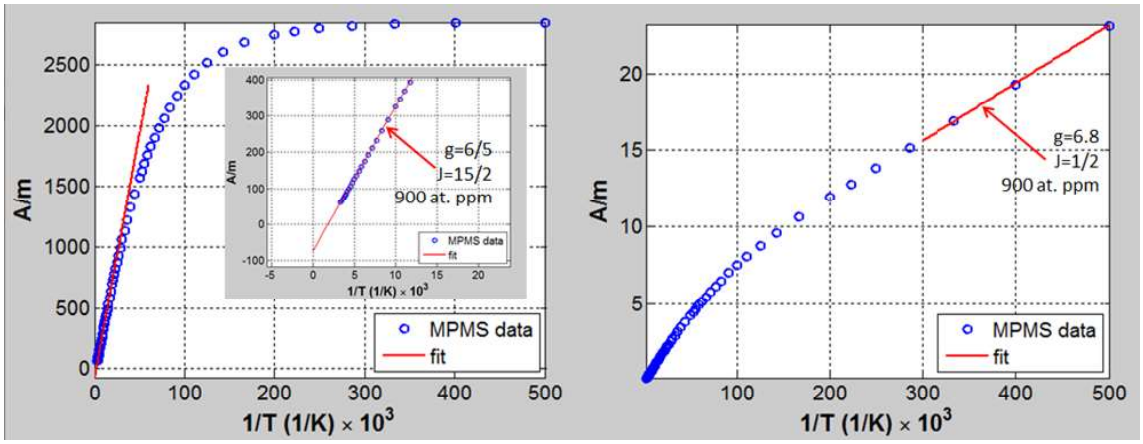

Figure 3.12: Replotted magnetization vs temperature data of a single 1000 at. ppm Ag:Er sample. **Left**: Fitting the slope of the magnetization in the high temperature regime. A fit parameter of 900 at. ppm Er in Ag matches the data well. **Right**: Fitting the slope of the magnetization at low temperature, Curie Law, regime. Once again, 900 at. ppm Er in Ag fits the data.

tion furnace. Samples which pass visual inspection have had magnetic properties measured in a commercial MPMS. Results indicate that samples have a uniform distribution of magnetic dopant at the targeted concentration.

Chapter 4

MMC Layout and Fabrication

4.1 Overview

This chapter will cover details of layout and construction of our Metallic Magnetic Calorimeters. Device architecture and component layout for two generations of devices will be discussed. A description of the microfabrication layers and absorber attachment will round out the chapter.

4.2 Base Device Architecture

Our MMCs are monolithic: all of the components of the detector reside on the same chip. A single, standalone device consists of: the SQUID core, signal pickup coils, magnetization coils with paramagnetic material, persistent current circuit for magnetization, particle absorbers attached to the paramagnet, and various thermal engineering/heat sinking features. These "single" devices, which are two-pixel detectors, are arrayed together to create larger, multi-pixel devices in order to increase

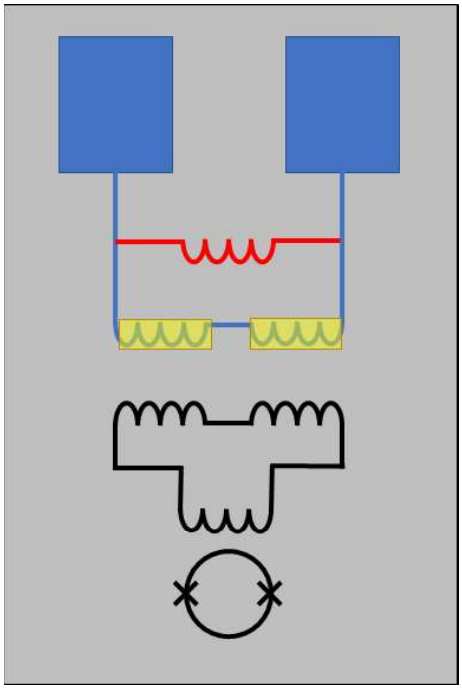

Figure 4.1: A schematic of a typical paramagnetic magnetometer that serves as the base of our MMCs. The blue pads and coils at the top are the excitation circuit with the red persistence shunt connecting the two coils. These excitation coils are also covered with the paramagnetic sensing material in yellow. The SQUID loop and pickup coils are on the bottom half of the device, in black

detection area and aggregate count rate.

To construct a full device, first the base SQUID magnetometer is fabricated, then paramagnet is deposited onto the device, then finally absorbers are attached. Figure 4.1 is a schematic of a typical UNM SQUID magnetometer, with paramagnet, but without absorbers. Each of the major components are described below.

SQUID Core/Pickup Coils

The SQUID consists of two Nb-AlOx-Nb Josephson Junctions that are created from a trilayer process. There are two main designs for our SQUIDs. We employ Ketchen

Style SQUIDs, which couple the sensing coils to the SQUIDs via a superconducting flux transformer [42] and also direct-coupled SQUIDs which have the SQUID loop and sensing coils as one.

Magnetization and Sensing Coils

The SQUID sensing coil are built directly above the paramagnet magnetization coil. A thin layer of Si oxide is deposited on top of the magnetization coils coils, to electrically isolate them, before the sensing coils are created. A second layer of Si oxide is then deposited over the sensing coils, before the paramagnetic sensor material is deposited on top.

After the paramagnet is deposited, another layer of Si oxide is deposited over the paramagnet to electrically isolate it. A layer of Nb is deposited on top of everything, encasing the coils and paramagnet. This "pancake coil" architecture, which was first developed by the UNM group [43], helps concentrate and parallelize the magnetic field from the magnetization coils, increasing both the flux per area in the paramagnet and the signal.

Persistent Current Circuit

A persistence current circuit for the magnetization circuit is built directly into the devices. A persistent current circuit consists of a superconducting shunt that shorts out the magnetization coils. This shunt is able to be switched into the normal state to allow currents that are injected into the magnetization circuit to flow into the coils. If the shunt is cold, it creates a closed superconducting loop with the magnetization coils. If a current is established in the coils while the shunt is in the normal state, and then allowed to cool back to the superconducting state, the external current can

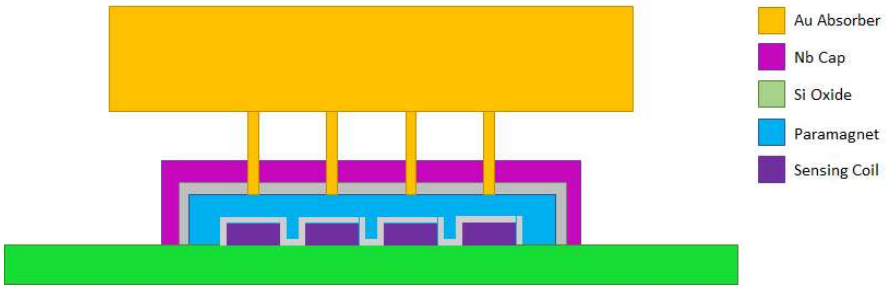

Figure 4.2: A cartoon representation of a gold absorber, cantilevered over the Nb cap, paramagnet, and sensing coil of an MMC. The absorber table sits on top of gold legs which provide a reduced-conductance thermal path to the paramagnet below.

be removed and due to conservation of flux, the closed shunt/coil loop is able to maintain a persistent current. This persistent current is highly stable and the fact that the circuit creates a closed superconducting loop also isolates the magnetization circuit from outside signals, both of which reduce the noise in measurements. The persistence current circuit is activated by small heating elements in first generation of devices (Chapter 5.3.3) or passive switches in the second generation (Chapter 6.2.1).

4.3 Absorber Architecture

To complete the construction of a full MMC, an absorber that will stop incoming particles must be attached to the base magnetometer. These absorbers take the form factor of a "table with legs", as shown in Figure 4.2. A large, flat gold table is cantilevered over the sensing coils by small gold legs. These legs, which are anchored directly to the paramagnetic alloy below, provide mechanical support and thermal contact.

Rather than attaching the table directly to the paramagnet sensor material, the legs are used to thermally isolate the absorber, giving absorbed particles time to thermalize within the gold table. This thermalization is crucial, as thermal contact

between the absorber and the paramagnet that is too strong will allow athermal phonons to escape and reduce the energy resolution of the detector [44].

Our devices incorporate the SQUID and sensor of the MMC onto the same die. The integrated SQUID and sensor presents complications to the absorber attachment process. The underlying SQUID is sensitive to elevated temperature processing and chemical attack. This limits the maximum processing temperature for a SQUID device to 150° C [45], eliminating the idea of attaching standalone absorbers to our devices with soldering or diffusion bonding [46].

Electroplating absorbers directly onto the devices is a technique that operates between 50-60° C and uses chemicals that are compatible with our microdevices. In order to electroplate these absorbers, a mold is created directly on the devices. This mold should be created using standard microfabrication techniques and be easily removed after the absorber plating process. A variation of the double mold process presented in C. Bates' PhD dissertation [47, 48] was employed for these devices and will be explained in more detail later in this chapter.

4.4 Microfabrication Layer Description

Fabrication of the MMCs is separated into two distinct stages: base device fabrication and paramagnet/absorber fabrication. The base devices and wiring layers, which are designed by the UNM team, are fabricated by STAR Cryoelectronics. The designs follow the STAR Cryoelectronics industrial Delta 1000 process [49], with only minimal variations. In particular, the thickness of the wiring layers are increased to a target thickness of 500 nm, to accommodate the "large" magnetizing currents of 100 mA required for the MMCs, and the thickness of insulating layers are reduced to a targeted 200 nm for improved magnetic coupling and increased step-edge coverage.

An entire wafer of SQUID devices is fabricated by STAR Cryoelectronics and then diced into smaller groups before the paramagnetic sensor material and gold absorbers are incorporated [50]. Adding on the paramagnet and absorbers onto a subset of the wafer enables the flexibility of customizing the paramagnet and absorber recipe on a device-to-device basis, rather than committing the entire wafer.

4.4.1 Base Device Fabrication

The base device, including SQUID, magnetizing and sensing coils, and parts of the heat flow path are fabricated by STAR Cryoelectronics using a modified version of their Delta 1000 Process [49]. The specific process used for the UNM devices are summarized below.

Layer 1: Tri-Layer

A Nb-AlO_x-Nb trilayer is sputter deposited onto a 4 silicon oxide wafer. To create the trilayer, the bottom Nb electrode, 500 nm thick, is sputter deposited onto the wafer, followed by 9.4 nm of sputtered Al. The Al is then oxidized, in-situ, before the top layer of 60 nm thick Nb is sputtered deposited.

Layer 2: Junction Definition

In order to create the Josephson Junctions, the trilayer is coated in a layer of positive photoresist, AZ 3312, and the junction areas are defined. A reactive ion etch (RIE), using CF_4, is used to remove the top layer of Nb, using the Al oxide underneath as an etch stop. The exposed Al oxide is then removed with an ion milling step, revealing the bottommost layer of Nb. The top two layers in the trilayer are removed in all areas that are not junctions, leaving the bottom layer exposed.

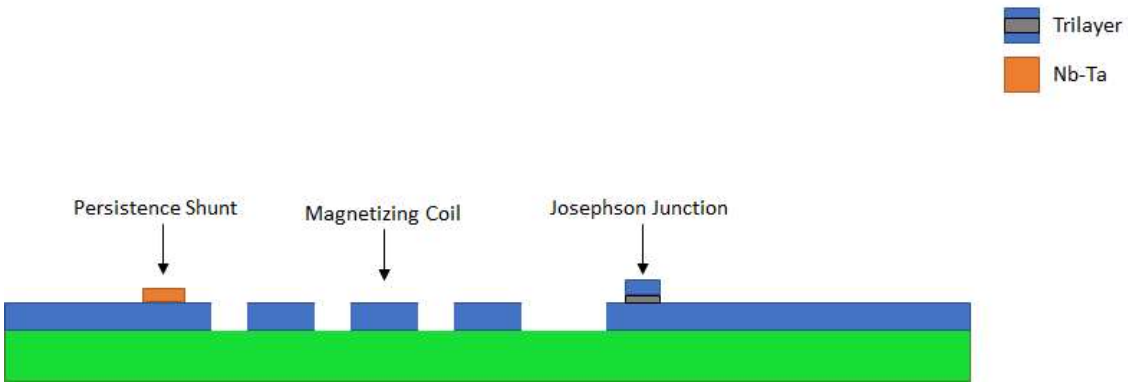

Figure 4.3: A cartoon representation of layers 1-4. The Trilayer is etched to form the Josephson Junctions and first wiring layer. The Nb-Ta persistence shunt is deposited over the first wiring layer.

Layer 3: Tri Layer Etch

The remaining trilayer base electrode is used as the first wiring layer. The base trilayer electrically connects the "bottom" of the junctions but is also be used to form the magnetization coils of the SQUID in certain designs. The wafer is coated in AZ 5214-E, in positive tone, and patterned to protect the junctions and expose the base Nb that will not be used in wiring. The exposed material is then removed with RIE.

Layer 4: Nb-Ta

This layer is a custom variation on the Delta 1000 process for some of the UNM devices. The wafer is coated with AZ 5214-E, in reverse image mode for liftoff, and a 250 nm thick layer of an alloy Nb and Ta (62 at. %) is sputter deposited. This alloy has a superconducting transition temperature of ∼5.3 K and is used to create passive persistence links. These links are used in the second generation of UNM devices [51] and will be discussed in more detail Section 6.2.1.

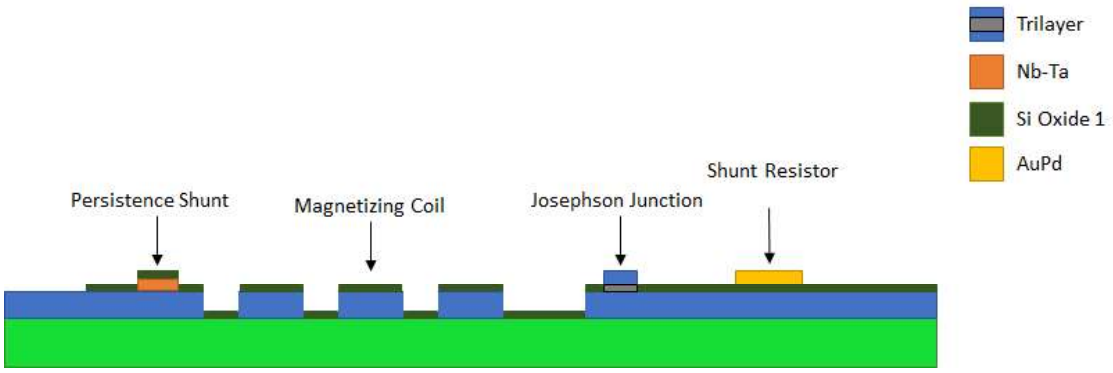

Figure 4.4: The addition of layers 5-7. Si oxide is blanket deposited then AuPd is deposited over the oxide for the SQUID shunt resistor. Vias in the oxide are then opened for connection to subsequent layers.

Layer 5: First SiO_2

A 100-200 nm thick layer of silicon dioxide is blanket deposited over the wafer with plasma enhanced chemical vapor deposition (PECVD). This oxide layer protects the underlying trilayer and serves as a platform for subsequent layers. In UNM devices, this layer is thinner than the standard Delta 1000 oxide of 300 nm. Thinner oxide is used to increase magnetic coupling and to increase the critical current of vias, by improving step-edge coverage between the two metal layers above and below, required by the UNM devices.

Layer 6: Au-Pd Resistors

The resistive elements of the devices are defined in this next layer. Junction shunt resistors, SQUID damping resistors, heating elements, and other resistive elements are created from AuPd. The wafer is patterned with AZ 5214 resist, in reverse imaging mode for liftoff. A layer of resistive AuPd, with a targeted sheet resistance of 1.0-1.3 Ω/square, is sputter deposited onto the wafer.

Layer 7: Etch First SiO_2

Vias in the first layer of oxide are opened to allow electrical contact between the trilayer and "top" of the junctions to the next Nb wiring layer. The wafer is patterned with a positive resist, AZ 3312, and RIE is used to remove the exposed oxide.

Layer 8: Niobium 2

The next layer is the second Nb wiring layer. In most designs, this layer is defines the sensing coils for the MMC. The wafer is patterned with AZ 5214-E resist, in reverse image mode for liftoff, and 500 nm of Nb is sputter deposited. This layer is thicker than the standard Delta 1000 process, as the UNM devices require high magnetizing currents of 100mA or greater.

Layers 9 and 10: Second SiO_2 and Vias

Another layer PECVD silicon dioxide is blanket deposited over the second wiring layer to protect it. This layer, is once again, thinner than the standard Delta 1000 process oxide of 300 nm. The wafer is coated and patterned with AZ 3312 positive resist, and the oxide is exposed where vias are needed to connect to the first wiring layer. The exposed oxide is removed with RIE.

Layer 11: Niobium 3

This third Nb wiring layer was used in the second generation of UNM devices to allow more wiring flexibility as was necessitated by the increase of complexity in those devices. To create this layer, the wafer is once again patterned with AZ 5214-E, in reverse image mode for liftoff, before 500 nm of Nb are sputter deposited over

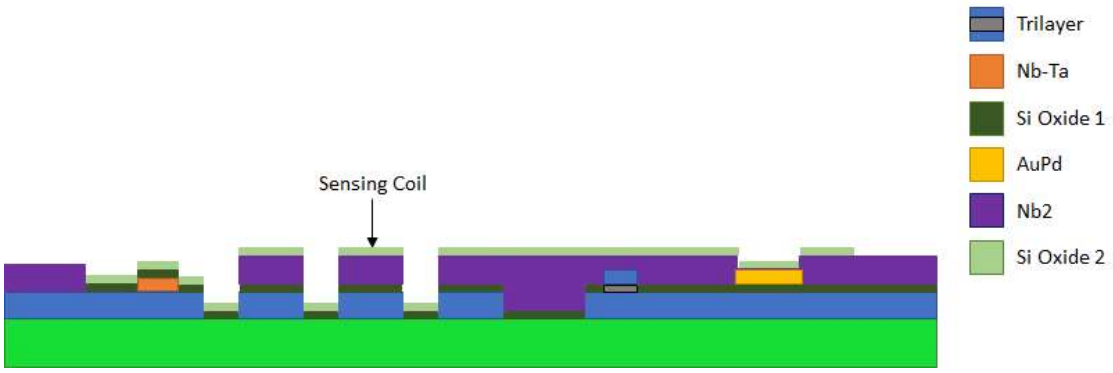

Figure 4.5: The addition of layers 8-10. The second Nb wiring layer is deposited and patterned, followed by the blanket deposition of the second Si oxide layer. Vias in the second oxide are then opened to allow connection to the Nb wiring layer underneath.

the wafer.

Layer 12: Au Pad

In the final layer of the process, Au is used for wire bond pads and thermal links. The wafer is patterned with AZ 5214-E, in reverse image mode for liftoff, before 400 nm of Au is sputter deposited. In the standard Delta 1000 process, an adhesion layer of 40 nm of Ti is used, but for the UNM devices, 40 nm of Nb is used instead. The use of Nb over Ti is due to the fact that Ti will alloy with Au and reduce the Au's thermal conductivity [52, 53].

4.4.2 Paramagnet and Absorber Fabrication

The above layers complete the construction of a fully functional SQUID magnetometer. The completed wafer of base devices is then diced into cm-scale chips to then be processed individually to add on the paramagnetic sensing material, Nb cap, and particle absorbers.

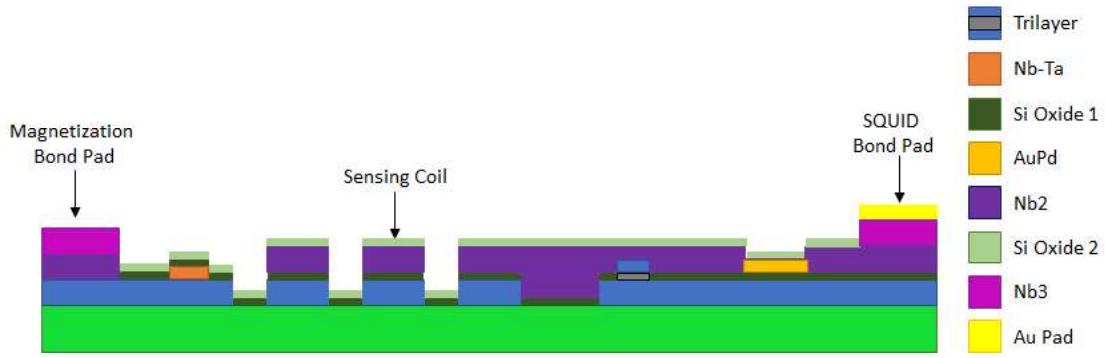

Figure 4.6: The addition of layers 11 and 12. The third Nb wiring layer is deposited and patterned, followed by the Au Pad layer. This completes the construction of a base SQUID magnetometer.

As most of the construction herein will be directed over the sensing coils of the base device, the figures will be concentrated in these areas.

Layer 13: Paramagnet

The paramagnetic sensing material is sputtered onto the oxide layer covering the sensing coils of the devices. The chips are patterned with AZ5214-E resist, in reverse imaging mode for liftoff, and loaded into UNMs dedicated paramagnetic materials sputtering system [54]. The UNM sputtering system is equipped with two 1" sputter guns, allowing the paramagnet to be co-sputtered to adjust rare-earth concentrations. For Au:Er, co-deposition occurs from a target of Au:Er 1% and a pure Au target, in a ratio of 1:10. Ag:Er is deposited from a single target with the desired concentration, usually 1000 ppm. Typical paramagnet thicknesses for UNM devices are 1.25 - 1.5 μm. Prior to the deposition of any paramagnetic material, an adhesion layer of Nb, 2 nm thick, is sputtered onto the cm-scale chip.

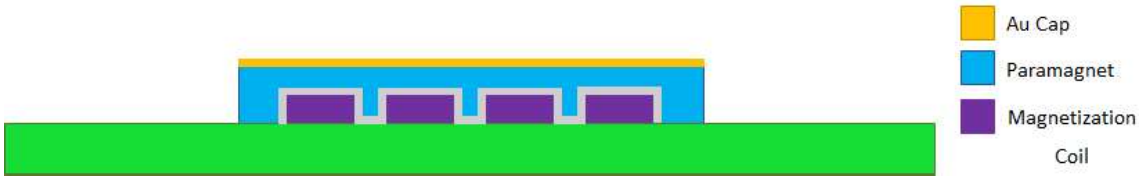

Figure 4.7: A cartoon of the sensing coils with paramagnet sputtered on top. The Au Cap has also been electroplated to the top of the paramagnet for increased thermalization.

Layer 14: Au Cap

Developed for the second generation of UNM devices, a layer of pure Au is electrodeposited over the top of the paramagnet for improved thermalization of the sensor material during particle absorption events. AZ5214-E resist is spun and patterned, in reverse image mode, over the device and a layer of pure Au is electroplated over the paramagnet. A commercial electroplating solution, Technic 25ES RTU, is used to DC electroplate 250 nm layer of pure Au. This is the same process used to electroplate the full absorbers, with more detail on the process below. Rather than sputter depositing the Au Cap, electroplated Au is used as it can have a very high residual resistivity ration (RRR) [48], which increases its thermal conductivity. While sputtered gold typically has a RRR of 2, Brown *et al.* was able to get a RRR as high as 56 and a sample plated at UNM had a RRR of 24.

Layer 15: Third SiO_2

A 100-200 nm thick layer of PECVD silicon dioxide is blanket deposited over the chip to protect the paramagnet and Au Cap. The chip is then patterned with AZ 3312 resist and vias are opened in the oxide with RIE. Au bond wire pads are also freed of oxide.

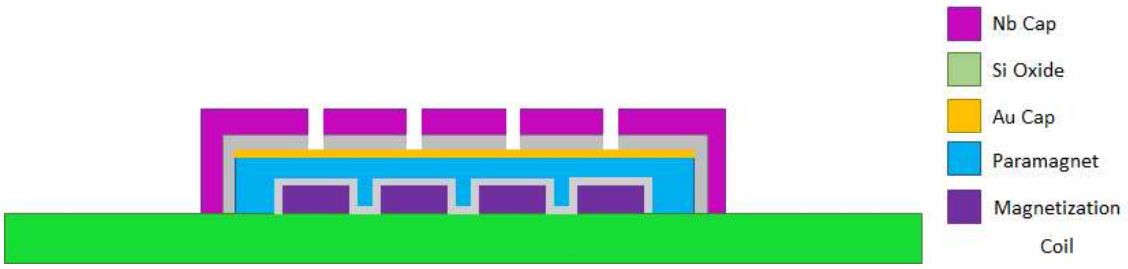

Figure 4.8: The addition of layers 15 and 16. Si oxide is deposited to protect the paramagnet and vias are etched to allow access to the paramagnet below. Nb cap is then deposited and patterned with holes for the absorber legs.

Layer 16: Nb Cap

A superconducting cap is placed on top of the sensing coils in order to concentrate the magnetizing field within the paramagnet, increasing the signal from the devices [43]. The chips are patterned with AZ 5214-E, in reverse image mode for liftoff, and 350 nm of Nb is sputter deposited. The caps cover the entirety of the sensor coils/paramagnet, but holes are left to allow the absorber legs to make direct contact, though the holes in the cap, to the paramagnet below.

Layer 17: Cu Absorber Legs Mold

With the paramagnetic sensor complete, the creation of the mold for the electroplated absorbers begins. This next layer will be used to define the legs of the absorbers and also support the mold for the body of the absorbers. A blanket layer of copper, 5 μm thick, is sputter deposited onto the devices. The copper is then patterned with AZ 3330-F positive photoresist, opening holes that are concentric to the holes in the Nb cap where the absorber legs will pass through.

To pattern the underlying copper, the chip is ion milled to remove the exposed copper. The UNM paramagnetic sputtering system is equipped with a 1.5 cm ion

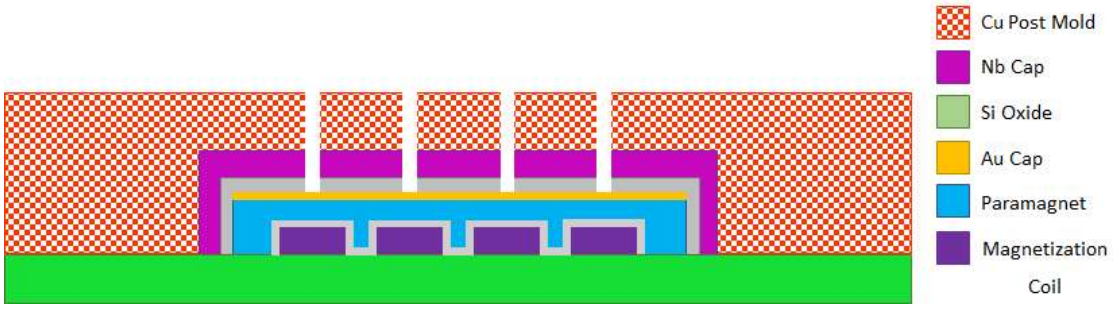

Figure 4.9: The addition of layer 17. 5 μm thick Cu is deposited over the entire chip and holes are patterned with ion milling and chemical wet etch to define the legs of the absorber.

gun, which is run at a beam current of 15 mA and beam voltage of 800 V. The working gas, argon, flows past the gun at 1 sccm. This setup mills the copper at a rate of 220 A per minute. Although the substrate is cooled to 0 °C during this operation, to insure the devices do not overheat, milling is regulated to 2 minute pulses with 5 minute rests in-between. To insure that the ion mill does not damage the underlying chip, the copper milling is halted when the remaining thickness is approximately 0.5 μm. The remaining copper is removed via a wet etch of Transene APS-100 Copper Etchant, diluted 1:3 in deionized water.

Layer 18: Electroplating Au Seed

A seed layer of gold is sputter deposited over the copper leg layer to promote the growth of high quality gold during the absorber electroplating procedure. This seed layer also ensures a continuous metal path from the paramagnet up into the absorbers. The photoresist AZ 5214-E is patterned, in reverse image mode for liftoff, over the chip and 200 nm of gold is sputter deposited only where the absorbers will be grown. Limiting gold coverage, as opposed to a blanket deposit, exposes more of the copper leg layer which facilitates quicker removal of the copper during the wet

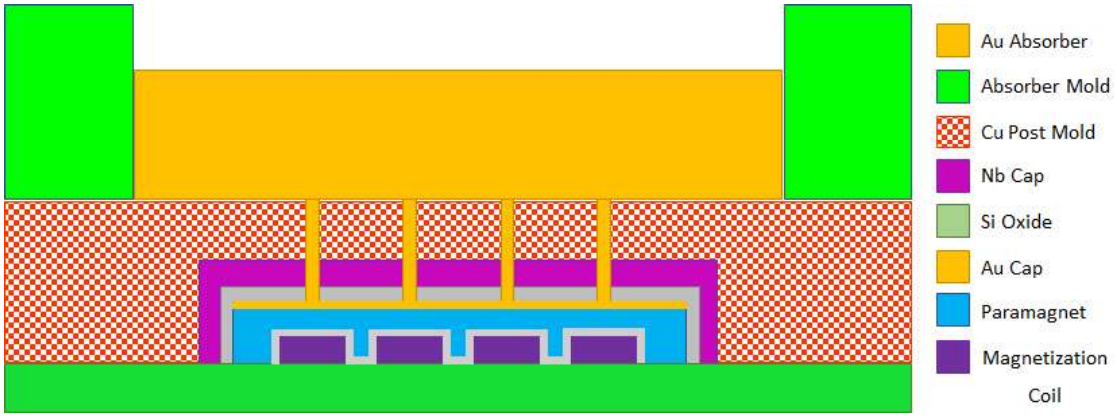

Figure 4.10: The addition of layers 18-20. 200 nm of Au is sputtered over the Cu layer as a seed for the absorber electroplating. The ultra-thick AZ 125nXT is patterned over the seed/Cu to define the mold for the absorber body. The absorber legs and body are then created in a single electroplating operation.

etch removal step.

Layer 19: Au Absorbers Mold

The mold for the absorber body is formed on top of the copper absorber leg mold. The ultra-thick photoresist, AZ 125nXT, is spun on approximately 200 μm thick and wells are patterned to form the mold for the body of the absorbers. Working with AZ 125nXT is notoriously difficult, therefore Section 4.5 is devoted to the specifics of using this resist.

Layer 20: Electroplated Au Absorbers

With the AZ 125nXT absorber mold formed on top of the array chip, the absorber bodies and legs are electroplated. The entire chip is submerged into a commercially available electroplating solution, Technic 25ES RTU, at 60° C. Details of the electroplating process are described in Section 4.6.

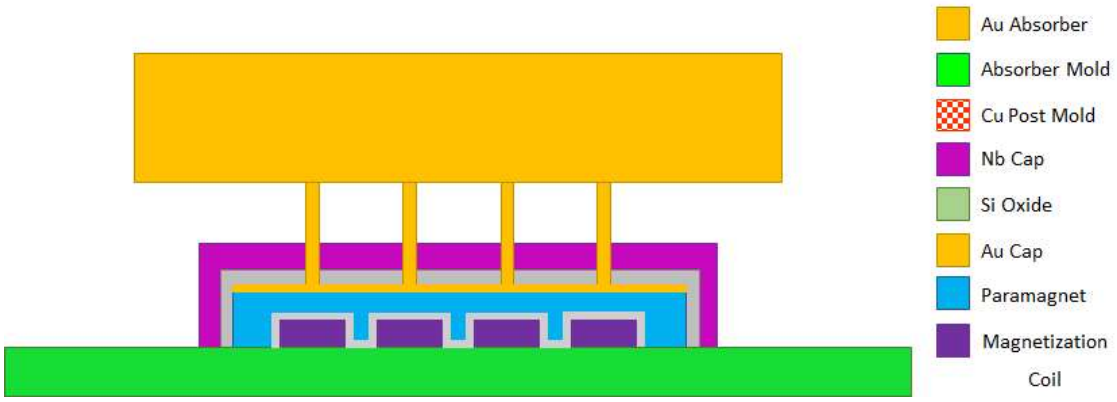

Figure 4.11: Freeing the absorber from the molds. The AZ 125nXT absorber body mold is removed via soaking in DMSO. The underlying copper leg mold is removed via soaking in a bath of 1:3 Transene APS-100 Copper Etchant and deionized water.

Once the absorbers are plated, the AZ 125nXT mold is removed by soaking the entire chip in dimethyl sulfoxide (DMSO). The mold will spall off and light agitation is used to displace sections that have been separated. Acetone will also remove AZ125-nXT, but can cause the mold to swell, which in turn, can damage the plated absorbers.

With the absorber body mold removed, the copper layer that defines the legs must be removed. The entire chip is soaked overnight in a solution of Transene APS-100 Copper Etchant, diluted 1:3 in deionized water. This process produces bubbles, so a dilute solution is used to avoid forming large trapped bubbles which could damage the absorbers. The chip remains in the solution until no new bubbles are observed.

4.5 Processing AZ 125nXT

AZ 125nXT is an extremely viscous negative photoresist that can be processed to be 100s of microns thick in one spin coating operation, can support high aspect ratios, and is developed to be resistant to electroplating baths. Compared to standard

microfabrication photoresists, the high viscosity of AZ 125nXT requires additional care to use effectively. The literature provides a very good starting guide for working with the resist [55], but additional development was still required to accommodate the processes described above. The procedure that was developed for handling AZ 125nXT for the UNM MMCs is described in the following subsections.

4.5.1 Procedure

The first major concern while using this viscous photoresist are trapping air bubbles while applying the resist to the wafer. Prior to use, the resist is allowed to sit for 8-12 hours at room temperature, to allow any trapped bubbles to rise to the surface and leave the resist. Once the resist is degassed, it is poured onto the wafer directly from the bottle, rather than with a dispenser. Pouring by hand allows the resist to stay laminar and prevent trapping bubbles between the wafer and the resist. Once the resist is poured onto the wafer, the wafer is rotated by hand to spread the resist before being placed on a standard spin coater. The wafer is then rotated at 1500 rpm with an acceleration of 1000 rpm/s for 15 s. This yields a resist $\sim$200 μm thick over a 2" wafer. Resist thickness are adjusted by changing the spin time.

After spin coating, the wafer is covered with a glass dish and set on a level plate at room temperature for 30 minutes. This allows the resist thickness to even out, which helps reduce the edge bead and makes subsequent contact alignment much easier [56].

After the room temperature leveling step, the resist is baked in a covered dish placed on top of a leveled hotplate. The resist is 45% solvent by weight and much too soft for a contact aligner in the as-spun state. To remove the excess solvents, the wafer is baked at 105° C, periodically weighed until the resist is between 20-25% solvent by weight. Care must be taken to not reduce the solvents below 12.5%, as

the resist will lose photosensitivity. The bake takes approximately 25 minutes for a 200 μm thick film on a 2" wafer.

Even with most of the solvents removed from the resist, it is still very soft and sticky. To prevent the resist and wafer from sticking to the mask, a barrier must be put between the two. The literature suggests using a thin sheet of clear mylar, 12.7 μm thick, between the wafer and the mask [55, 47]. This approach does prevent the wafer from adhering to the mask without blocking too much of the exposure light, but comes with a large flaw. During contact alignment, the Mylar can crinkle if there are any irregularities on the underlying resist. These crinkles can transfer patterns onto the resist, which can cause huge defects.

Due to the complication that can arise from using mylar, the top antireflective coating, AZ Aquatar was used as an alternative barrier. Aquatar was chosen as it is a clear, flexible barrier that does not interfere with exposure of the resist. It is also water soluble and will be removed during the resist development step. After the resist is baked to the proper solvent level, Aquatar is dispensed from a filtered syringe onto the wafer. The wafer is placed back onto the spin coater and then spun for 60 s at 1000 rpm before a short bake at 105° C for 1 minute to dry the Aquatar.

The wafer, now with a protective layer ontop of the AZ 125nXT, is placed onto a contact aligner, where it is exposed for 600 s at an exposure energy of 16.6 mW/cm^2. The exposed resist is then developed with MIF300 developer for 20 minutes. The wafer is suspended in a beaker of developer on a stir plate. This constant stirring allows the developer to reach the deep wells in the resist evenly. Once developed, the wafer is soaked in deionized water to remove all the residual developer and then spun at 1000 rpm to air dry. Any remaining water is removed by slowly baking the wafer above a 100° C hot plate.

A final long bake is performed to remove any built up stresses in the ultra thick

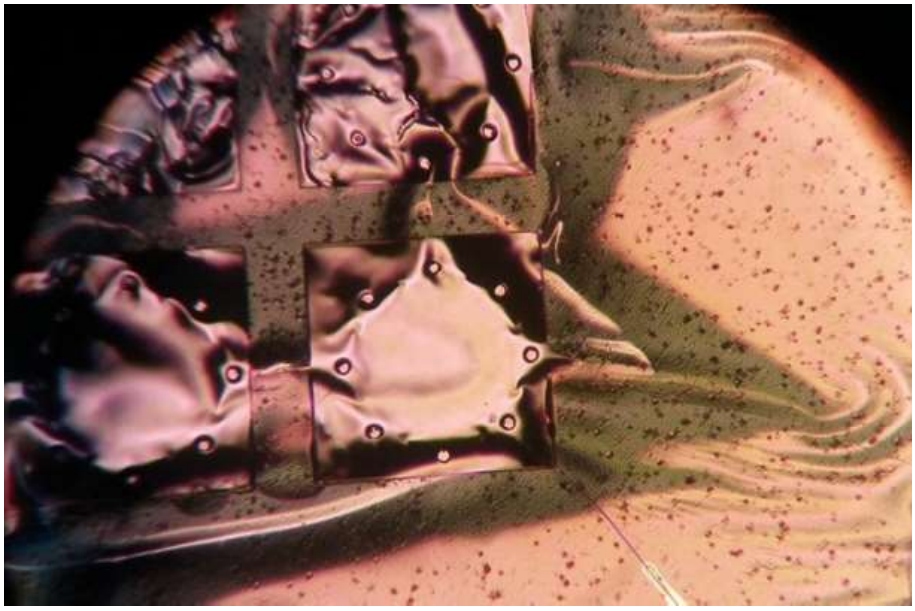

Figure 4.12: Optical micrograph of AZ 125nXT molds patterned over 200 nm of Au that was deposited over a layer of patterned AZ 5214-E. The dark corners of the square molds are evidence of the solvents from the AZ 125nXT dissolving the underlying AZ 5214-E, which caused the Au seed layer to deform.

resist. The wafer is placed into a small convection oven and the temperature is slowly increased up to 110° C over the course of 2 hours. The wafer is then baked for 8 hours at 110 °C before power is removed from the oven and is allowed to slowly cool over the course of another 8 hours, to prevent thermal shocks. The wafer is removed once the oven has cooled below 30 °C.

4.5.2 Cu Leg Mold

The recipe for creating stacked molds for the electroplated absorbers was adapted from the PhD dissertation of C. Bates [47]. His approach uses AZ 5214-E to define the layer for the absorber legs, a blanket layer of Au as the seed for electroplating, then the AZ 125nXT over the top to define the bodies of the absorbers.

Following this technique, a layer of AZ 5214-E was spun and patterned to define the absorber legs, followed by a 200 nm thick sputtered Au film as the seed layer for electroplating and as a barrier to protect the AZ 5214-E. The AZ 125nXT was then patterned over the seed layer to define the body of the absorbers. A major problem was found when the solvents from the AZ 125nXT seeped into the AZ 5214 below and started to dissolve the underlying layer. This was evident from the crinkling of the intermediate gold seed layer as seen in Figure 4.12.

A more resilient underlayer in which to define the absorber legs was now required. The famously resilient photoresist, SU-8, has been successfully used in the past as an electroplating resist for MMCs [39]. SU-8 is resistant to the solvents in AZ 125nXT but is also very resistant to common cleanroom solvents, such as acetone. At the end of the absorber electroplating, the resist molds need to be stripped away to free the absorbers. The only stripper that was found that could remove the SU-8 in any reasonable amount of time was the Piranha etch (3:1 H_2SO_4:H_2O_2). Unfortunately, Piranha is extremely aggressive and will destroy the underlying SQUID devices along with the molds.

Several different photoresists were tested with this process before transitioning to a metal mask. Copper can be sputter deposited as a film of a controllable thickness and be patterned to create the mold for the absorber legs. Copper is fully immune to the solvents in the AZ 125nXT but can be removed at the end, with extremely high selectivity, via the commercial wet etch, Transene APS 100. Copper masks are a technique used by STAR Cryoelectronics for some of their commercial devices, therefore it is completely compatible with the UNM MMC process.

4.6 Electroplating Absorbers

Electroplating is a good technique for the creation of the absorbers, as it allows the attachment of many absorbers within one electroplating step. Solutions that are chemically mild, compatible with photoresist, that can be used between 50-65° C, and are commercially available and come with industrial support from the vendors during development.

To electroplate the absorbers into the mold, electrical contact to the gold seed layer is obtained by attaching a 20 AWG copper wire to a section of exposed copper in the corner of the chip. A conductive 2-part silver epoxy (Mg Chemicals 8331) is used to create an electrically conductive joint before the wire and joint are then sealed with a non-conductive epoxy, Stycast 1266, to prevent electroplating onto these areas. A mild cleaning step is performed, prior to plating, by dipping the entire chip in a commercial electroplating acid dip solution (Midas Acid Dip 335-157) at room temperature for 1 minute, then a rinse in deionized water. This solution helps clean and activate the exposed metal surfaces but is mild enough that it does not attack the photoresist or epoxy.

The chip is held in a Teflon jig, approximately 2 inches from a platinized anode, immersed into the commercial gold plating solution, Technic 25ES RTU. The solution is heated to 60° C and mildly agitated during plating. For a uniform, low stress plated films, the manufacturer suggests plating with a pulsed power supply instead of a constant DC current. Current pulses of 0.25 A/decimeter with a cycle time of 500 μs on with 200 μs rests, provided growth at a rate of $\sim$160 nm per minute.

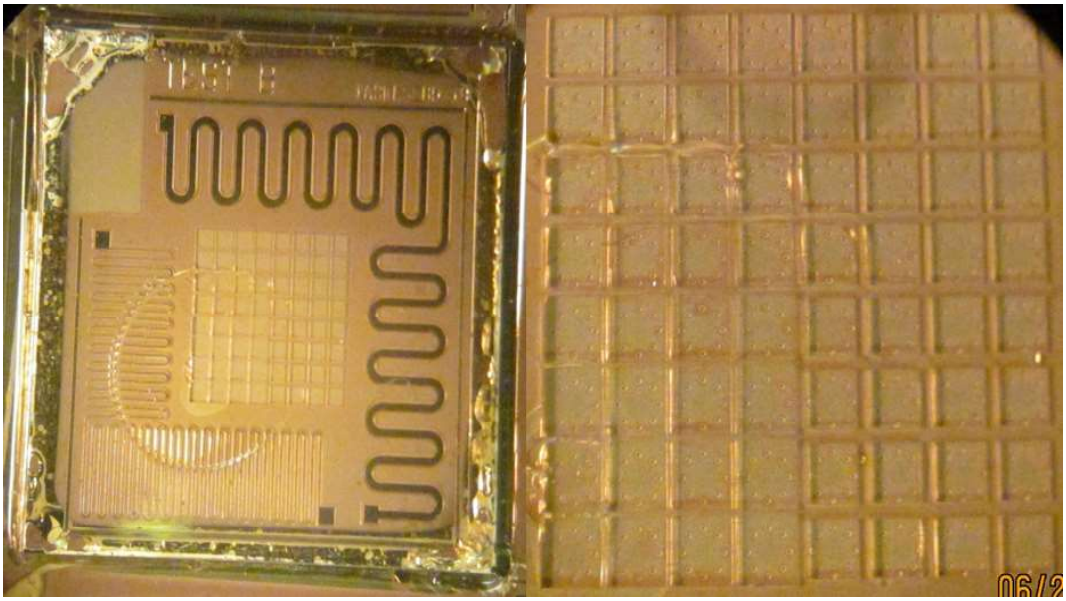

Figure 4.13: **Left:** Photo of a 1 inch squared test chip with two electroplating molds. The chip has a thick layer of sputtered copper, thin sputtered gold, then the ultra thick AZ125 nxT photoresist patterend on top. **Right**: A zoom in of the middle, looking closely at the field of absorber molds.

4.6.1 Au Plating Test Chip

A test chip was created using the two mold technique for gold electroplating tests. A 1 inch square silicon chip was sputtered with Cu and ion-milled to define the legs of the absorbers. A gold seed layer was sputtered over the top of the copper and a layer of AZ125 nXT was spun and patterned with various features, including different sized absorbers and meander patterns to test the RRR of the electroplated gold. This test chip was electroplated with 20 μm thick gold and the molds were removed to free the absorber structures. Figure 4.13 is a photograph of the test chip before electroplating and Figure 4.14 after. The square absorbers can be clearly seen with the legs shown as a ring of 8 circles in the middle of the absorbers.

Once the AZ125 nXT and the Cu is removed, the absorbers and meanders are free. To test the quality of the electroplated gold the electrical resistance of the large

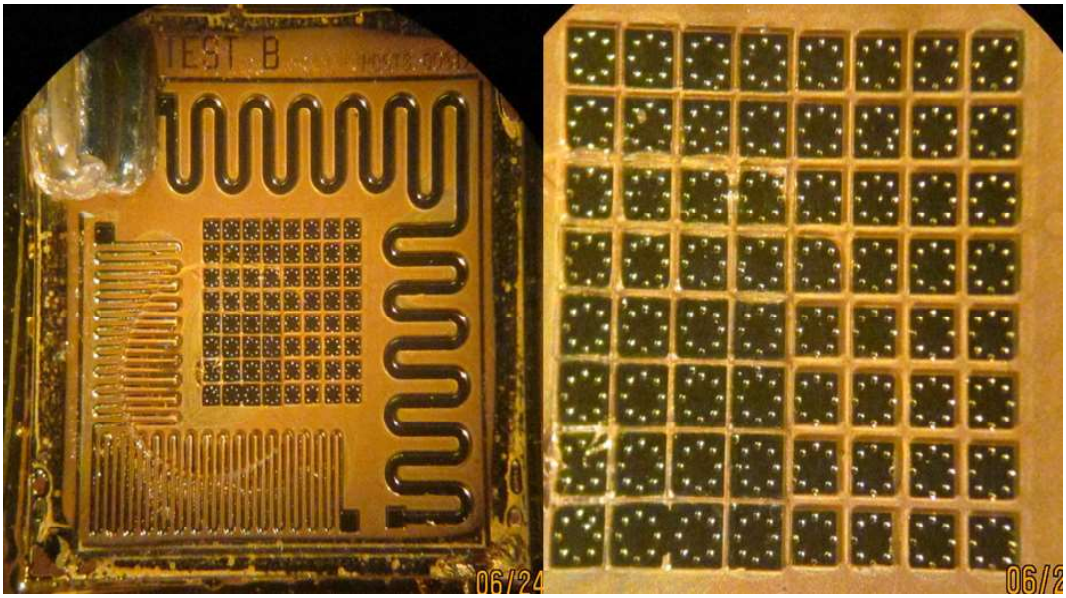

Figure 4.14: **Left**: Photo of the 1 inch squared test chip from Figure 4.13 after gold electroplating. 20 μm thick gold was grown before the molds were removed. **Right**: A zoom in on the middle, looking closely at the field of Au absorbers. The ring of 8 dimples are the legs that hold up the body of the absorbers.

meander was measured at room temperature and again in liquid helium at 4 K. The ratio of the resistances is known as the gold's RRR, which for this sample was found to be 24.

The electroplated absorbers were also inspected with a scanning electron microscope, as shown in Figure 4.15. Focus was directed to a subsection of the central absorber field, looking at 450 μm square absorbers that have 25 μm spacing. These absorbers are supported by 50 μm diameter legs that are 5 μm tall. A zoom in one a single absorber shows a shadow near the bottom of the absorber. This shadow indicates that the absorber is cantilevered above the chip, with no visible sagging in the absorber body.

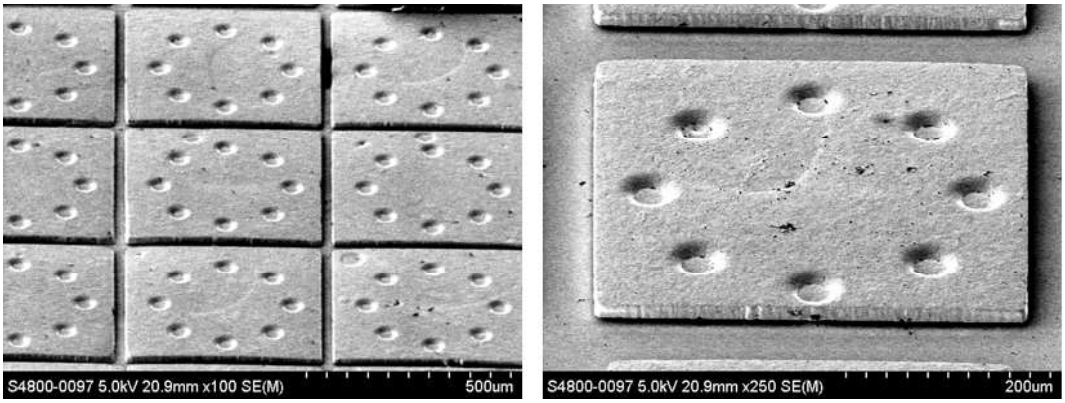

Figure 4.15: **Left**: Scanning electron microscope image of a field of 450 μm square, 20 μm thick, electroplated gold absorbers, spaced 25 μm apart. The absorbers are supported by 50 μm diameter legs that are 5 μm tall. **Right**: A zoom in on one of the absorbers. Notice the shadow cast on the bottom of the absorber, indicating that it is cantilevered above the chip, with no visible sag in the absorber body itself.

Chapter 5

UNM Devices Gen 1: Paramagnetic Sensors

5.1 Overview

This chapter will cover specific details and testing of the first generation of prototype devices designed by UNM. These devices were not meant to be full particle detectors, rather they were a test bed to explore a wide array of different designs. The device architecture is similar across all devices but with components varying. The various versions of the devices will be described along with the results from testing. Aspects of these designs that did and did not work will be discussed, as they pertain to the second generation of devices.

5.2 Design Space

The device layout of this generation of devices is based on previous work with MMCs in collaboration with STAR Cryoelectronics [57].Figure 5.1 shows a schematic of a typical device from this wafer. Following this layout, the magnetization/sensing coils are centered vertically on the device, with the SQUID junction centered horizontally, below the coils. Excitation wiring and bond pads for both the magnetizing circuit and persistence switch circuit are located at the top of the device whereas wiring and bond pads for the SQUID are located at the bottom of the device. Major additions include the new persistence circuit, located on the right and left sides of the device, and the large gold thermal bus in the center.

The major components, which are described in Chapter 4, that were varied among the different designs are: 6 different SQUID junction areas, 28 sensing coil designs, and the 5 different persistent current circuit designs. Creating and testing all possible combinations of components would be an impossible task, therefore a baseline device was created that closely mimicked devices that had been shown to work previously [57]. Starting from this "safe" design, exploratory designs, including selected subsets of the new features, were included on the wafer.

Along with changing the specific components of the device, variations of the wiring topology between the sensing coil and SQUID junctions were explored. The devices could have one of three different wiring topologies, mainly varying the degree of isolation of the SQUID loop from the sensing and excitation circuits, and the addition and location of the persistent current circuit, as described in Figure 5.2.

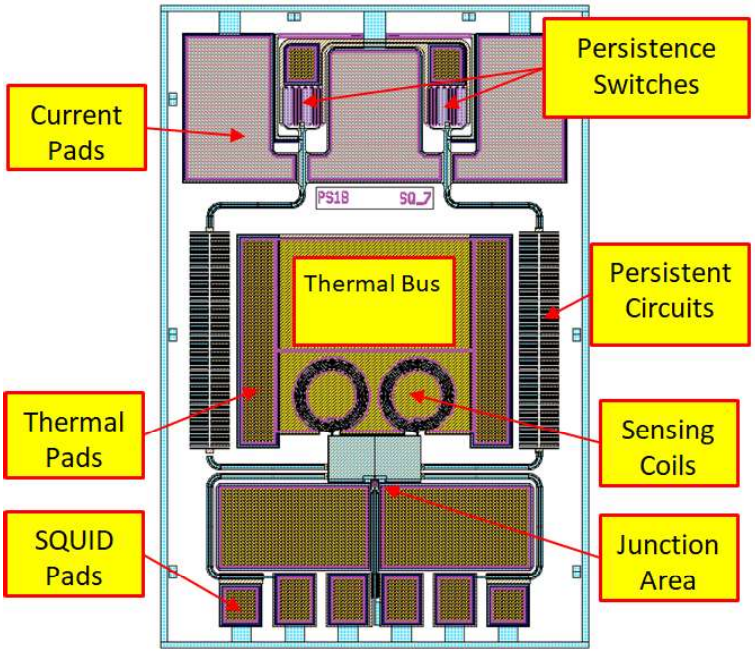

Figure 5.1: A schematic of a typical device from this wafer, without absorbers. The large coils in the center are the sensing coils for the SQUID, whose junctions lie below the coils. The magnetization coils for the paramagnet lie underneath the sensing coils and the persistence current circuit runs along the outside of the device. Bonding pads for magnetization coils and persistence current circuits are at the top of the device whereas the SQUID bond pads are found on the bottom.

5.3 Testing Results

The first, and most important, test of the devices is whether or not the SQUID functions. For rapid characterization, the devices are dipped into liquid helium in an RF shielded room and tested with a modulation electronics package provided by STAR Cryoelectronics. Once cooled to 4 K, an external flux source is applied to the SQUID and the response is recorded. The height and periodicity of this "transfer function" is used to assess the health and quality of the SQUID.

The SQUIDs are then operated in flux locked loop mode and their white noise spectra are recorded with a spectrum analyzer. The noise spectra, and thus the per-

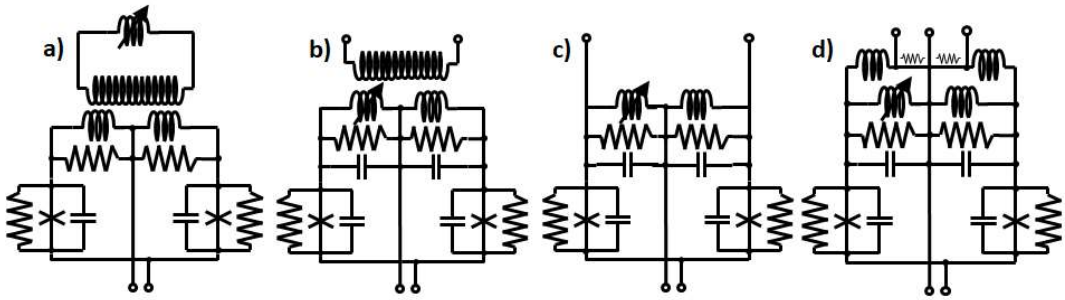

Figure 5.2: A schematic of the three different sensing coil topologies in this generation of devices, ranging from the "safest" to the most "risky". **A)**: for reference, the standard topology for MMCs, which is not included in this wafer. The excitation circuit, sensing circuit, and SQUID are all electrically isolated. The SQUID is coupled to the sensing circuit through a superconducting transformer. Excitation circuit now shown here. **B)**: the SQUID loop is extended out to act as the sensing coil. The excitation circuit is still isolated from the SQUID/sensing circuit. **C)**: the SQUID loop is extended to act as both the sensing coil and excitation coil simultaneously. **D)**: the SQUID loop is extended to act as both the sensing coil and excitation coil as before, but with the addition of the persistent current circuit.

formance of the device, are rated by the 1/f noise shoulder, flatness of the spectrum from 10-1000 Hz and the high frequency rolloff shoulder. For quick comparison between devices, the noise at 1 kHz, in units of $\mu\Phi_0/\sqrt{Hz}$, is generally quoted, where Φ_0 is the magnetic flux quantum. Figure 5.3 are typical noise spectra and transfer functions recorded for these devices.

Devices with paramagnetic alloys and/or with persistent current circuits that pass initial testing in liquid helium, are tested more throughly in UNM's dry ADR cryostat. SQUID response to the paramagnet and current trapping are then measured from 3 K down to 50 mK in vacuum. In the following section, noise spectra from several devices, with varying components, are presented. Even though not every individual device could be tested, a picture of the effect of these component changes can be painted.

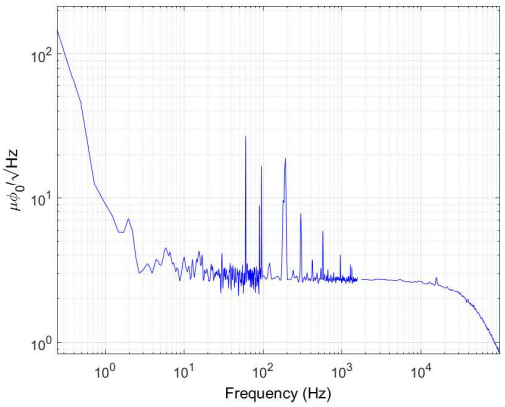

(a) Typical Noise Spectra

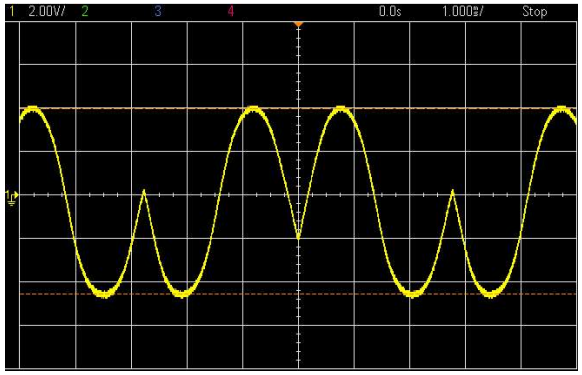

(b) SQUID Transfer Function

Figure 5.3: **Left**: Noise spectrum taken at 4 K for a device without paramagnetic alloy. The log-log scale is $\mu\Phi_0/\sqrt{Hz}$ on the Y-axis and Hz on the X-axis. **Right**: SQUID transfer function, its response to an external flux signal, taken at 4 K, recorded as a voltage signal on an oscilloscope. The scale is 2 V/div on the Y-axis and 1 ms/div on the X-axis.

5.3.1 SQUID Junction-Area Variations

The SQUIDs on this wafer varied in their topology, being designed either a "normal" or a "narrow" versions, each themselves with capacitances of 1 pF, 7 pF, or 30 pF. The "narrow" version of the SQUIDs had a more restrictive wiring topology, which is a useful avenue to explore for more complicated designs in the future. The main figure of merit for these different designs were their effect on the noise spectra of bare devices. To demonstrate this, Figure 5.4 shows noise plots from SQUIDs of the same "style", with three different bypass capacitances, taken at 4 K. The 1 pF SQUID, in blue, is the quietest, where the highest noise comes from the 30 pF SQUID in green. The 7 pf SQUID, in red, is only slightly noisier than the 1 pF device, but all three are very similar and all high performing. There was also no noticeable difference in noise performance between the normal and "narrow" variations of the SQUIDs.

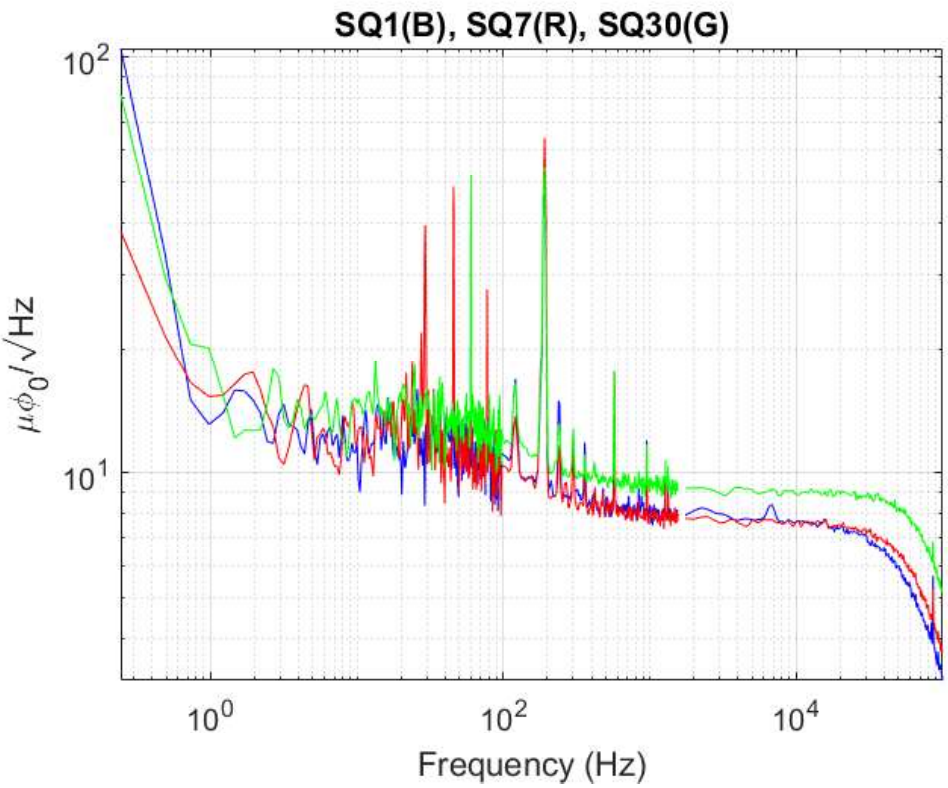

Figure 5.4: Noise spectra for three different SQUIDs without paramagnet, overlayed ontop of each other, at 4 K from devices that only varied in the SQUID bypass capacitance. The best performing device is the 1 pF SQUID in blue, followed by the 7 pF SQUID in red, and finally the 30 pF SQUID in green. All devices performed similarly to each other and just as well as commercial devices designed by STAR Cryoelectronics.

5.3.2 Sensing Coils

The sensing coils on this wafer of devices come in three different form factors: rectangular meanders, spiral coils, and microstrip devices. These coils were created in various sizes that corresponded to an inductance of 100, 200, 300, or 500 pH. Each individual device contains two, astatic, coils wired in series. This astatic pair arrangement helps shield the input circuit from external magnetic field noise, as measurements are of a differential nature. A protective oxide layer is deposited onto

the coils before the paramagnetic sensor material is sputtered on. The dual coil arrangement allows a single device to act as a pair of detectors, as the sign of the signal is opposite between the two.

The majority of testing was done on devices that had the rectangular meander coil geometry, as that geometry was the "safest" to test, on an otherwise experimental set of devices. As one would expect, the larger coils are noisier, due to their larger enclosed area which picks up more magnetic noise, but there were no designs that did not function adequately.

Paramagnetic Au:Er was sputter deposited onto some devices and tested in the UNM ADR Cryostat at temperatures as low as 50 mK. Current was applied to the excitation coils to polarize the deposited paramagnet and the SQUID response to changes in the magnetization of the paramagnet as a function of temperature were recorded. Since this response was reproducible and a function of the temperature, and the magnetization of the paramagnet follows a Curie Law, it showed that both the circuitry and the paramagnetic alloy were in working order. This result was extended into creating a paramagnetic thermometer, as discussed in Section 5.3.5.

5.3.3 Persistent Current Circuit

A persistent current circuit consists of a superconducting shunt, with a heater element on top of it, that short circuits the two coils in the magnetization circuit, as shown in Figure 5.5. Applied current will flow across the shunt and bypass the magnetization coil unless the heater is activated to drive the underlying shunt into the normal state. To trap a persistent current, an external current is applied to the magnetization circuit while the heaters are activated. Once the desired magnetization current is established, the heaters are deactivated, allowing the shunt to become superconducting again. With the shunt superconducting, the applied current is slowly

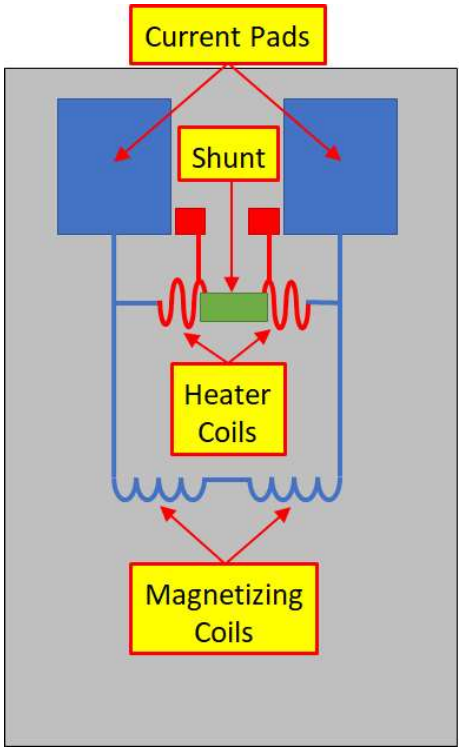

Figure 5.5: A schematic of a typical persistent current circuit (ballast inductors not shown). The magnetization circuit is shown in blue and the heater circuit is shown in red. The 4 pads at the top are current injection pads, the red meanders are the heater elements and the blue coils at the bottom are the magnetization coils. Magnetization current that is applied while the heaters are not active is shorted through the shunt at the top.

removed and conservation of flux causes a screening current to flow in the shunt, maintaining current through the magnetization coils.

The persistent current circuit in these devices are heater elements at the top of the device. The heater elements are two astatic rectangular meanders that sit above a mirrored trace in the excitation circuit that acts as the shunt. This heater is designed such that an injected current is split between the two heaters elements in such a way as to generate zero net magnetic flux. This zero-flux design was in response to old designs that would disrupt the SQUIDs during heating, as those old

designs would impart magnetic flux. The heaters are activated with periodic short pulses of current to drive the local wiring normal, without driving the entire chip normal. The ballasts on the side of the device are also an astatic pair. The entire circuit is meant to have a net loop area of zero, to minimize noise pickup.

In general, the addition of the persistent current circuit increased the noise of all devices. This is thought to have been caused by the large array of ballast inductors. Although the backside of the wafer has a layer of sputtered Nb to act as a superconducting shield, the ballast inductors being located at the edge of the chip and above the Nb shield, were picking up environmental noise. The addition of a piece of lead underneath the devices, which was larger than the chip, helped reduce the noise. It was also found that a design error resulted in one of the ballasts to have one fewer turns, breaking the zero loop area symmetry, causing this design to be noisier than intended.

Current trapping experiments were conducted in the UNM cryostat, under vacuum, and at temperatures below 4 K. Excitation current is applied to the devices from a room temperature battery while current pulses were applied to the persistence heater from a function generator. Ideally, during the heater pulses, the shunt is momentarily resistive which diverts some of the applied current into the excitation circuit. With this method, the excitation circuit can be slowly energized, reducing the risk of quenching the chip from heating.

Unfortunately, no evidence of current injection or trapping was recorded. When current is applied to the excitation coils of devices without the persistent current circuit, a flux signal is applied to the SQUID and can be seen with our STAR Cryoelectronics modulation electronics package, indicating current flowing within the magnetizing coils. When current is applied to a device with a persistence current circuit, with or without the heater running, no change in SQUID signal can be seen. Five different variations of the heater were designed, which varied in the amount

of wire in the heater blocks. None of the different heater designs seemed to allow current into the excitation circuit using any non-disruptive heating schemes.

To attempt to diagnose the cause of the poor performance, the persistence current circuit was designed such that traces near the heater could be physically broken, permanently disabling the heater and shunt and allowing current to be directly injected through the magnetization coil. When devices that had persistence current circuits, which previously showed no evidence of current injection, had their switches broken and retested, current was seen entering the magnetization coils. In retrospect, the design of the heaters and ballast inductors, were fundamentally flawed. First, the meander heater design caused the inductance of the shunt to be comparable to induction of magnetization coils. The persistent current that is trapped is proportional to the inductance of the shunt and of the magnetization coils in the following relation:

$$I_{\text{Persistent}} = I_{\text{Applied}} * \frac{L_{\text{Coil}}}{L_{\text{Coil}}+L_{\text{Shunt}}} \tag{5.1}$$

Which shows that any applied current would only be fractionally trapped within the coils. The ballasts themselves were created with 2 different wiring layers, crisscrossing over each other. This large number of crossovers in the wiring layer will reduce the critical current of the circuit, which will further reduce the amount of current that could be trapped. Given the difficulty of this design and its poor performance, this approach was abandoned in favor of passive persistence switches and a much simpler magnetizing circuit design for the second generation of devices.

5.3.4 Topology Variations

One of most enterprising changes to these devices are the different variations in wiring topology. As sketched out in Figure 5.2, are the four different topologies, increasing

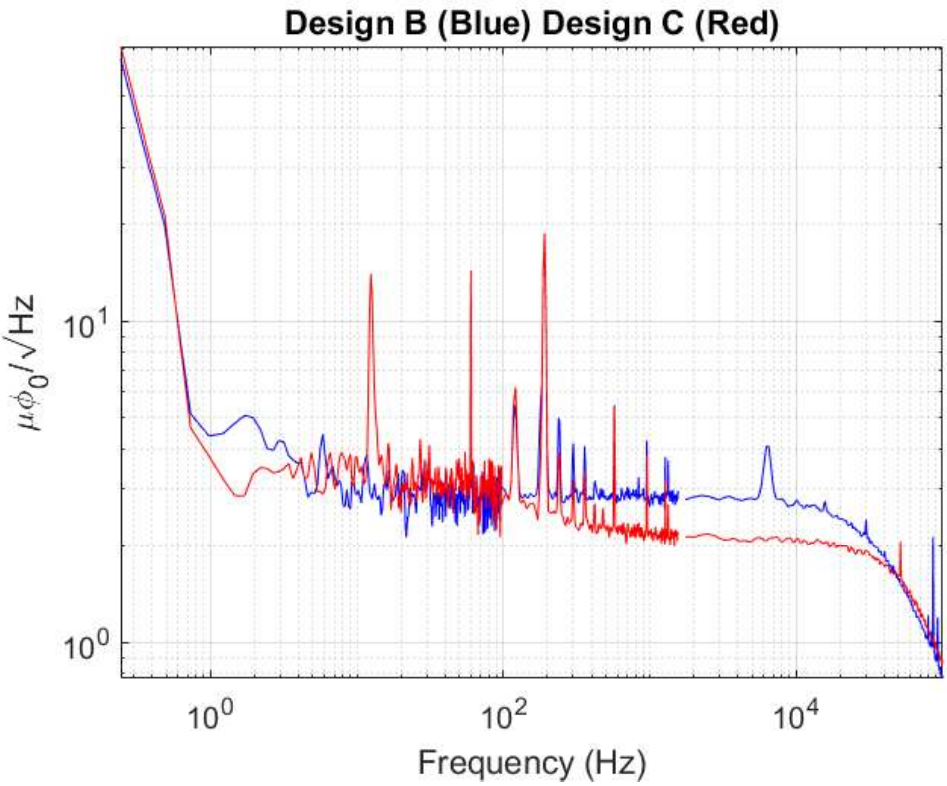

Figure 5.6: Noise spectra taken from devices without paramagnet at 4 K. A Design B device is shown in blue and a device with Design C, in red. Design B is the most "conservative" design, having the SQUID/sensing loop, separated from the excitation circuit. Design C uses the SQUID/sensing loop as the excitation loop. Design C, being more complicated, does not hinder the noise performance of the devices, and in this case, performs better.

in complexity from left to right. The latter three designs are explored on this wafer. Design A is the "standard" topology used in the field, where the excitation circuit, sensing circuit, and SQUID loop are all separate. The SQUID is coupled to the sensing circuit through a superconducting flux transformer. Design B extends the SQUID loop to also act as the input coil, with separate excitation coils. Design C has the SQUID coil extended as before, but it serves as both the sensing and excitation coil. Design D is the same as C but incorporates the persistent current circuit.

Design B is the most conservative design and is used as the benchmark against which the other designs on this wafer are compared. Design B devices are usually the quietest, performing as well as the STAR Cryoelectronics commercial line of SQUID devices. Testing Design C, which has the extended SQUID loop act as both he sensing and excitation coil, did not show any degradation of the device performance. As seen in Figure 5.6, Design C performs as well as, and in this case exceeds, Design B, with all other components being the same.

Design D incorporates the persistence current circuit into the devices. As detailed in Section 5.3.3, the addition of the persistence circuit hindered the performance of all devices and does not provide persistent currents. As such, the persistence current circuit will be redesigned for future devices and does not warrant further discussion here.

5.3.5 Paramagnetic Thermometry

As a proof of concept experiment, a set of these devices were purposed as paramagnetic thermometers. Design B devices, consisting of fairly large rectangular meander coils (400 pH), had a layer of Au:Er paramagnet sputter deposited onto one of the two coils. The paramagnet was 1.2 μm thick with a concentration of 1 at.% Er, much higher than would be used in an MMC.

The coils were excited astatically with a 50 Hz sine wave, in a bridge configuration, and a resistor network was used to balance the signal from the bare coil. The device was cooled to 100 mK and the bridge was adjusted such that the signal from the two coils would null each other. From there, the temperature was slowly changed and the SQUID voltage difference would be recorded as the thermometer signal. The temperature was recorded with resistive semiconductor thermometers with commercial resistance bridges and compared to the voltage signal of the device

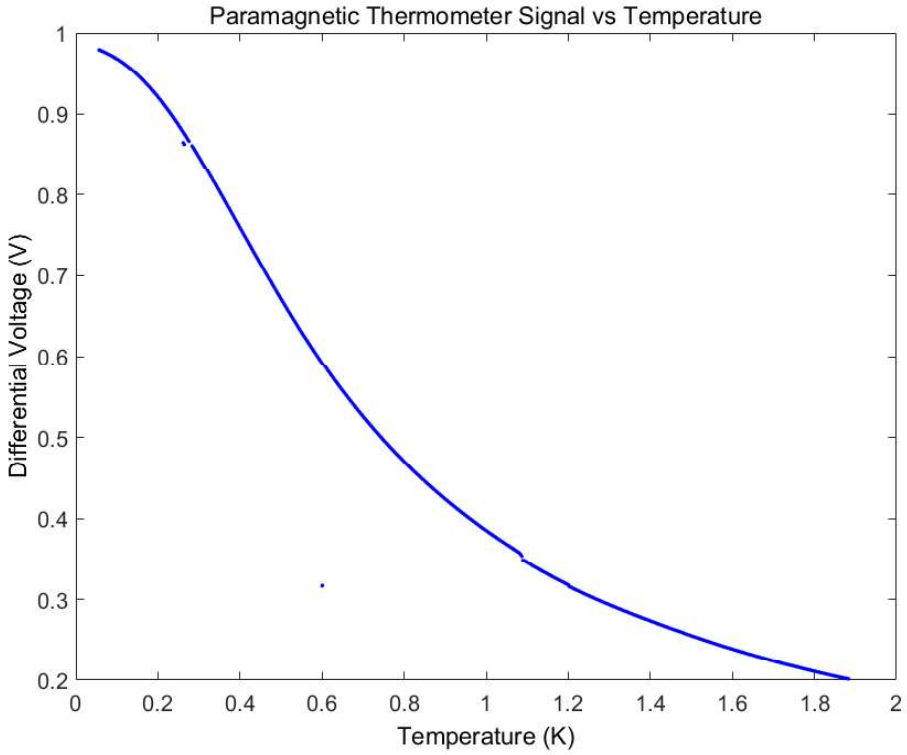

Figure 5.7: A plot of the signal from a paramagnetic thermometer equipped with 1 at.% Er in Au vs temperature. This paramagnetic thermometer has a temperature range of 50 mK to 2 K. Although the device is not optimized for thermometry, and the resistance bridge is homemade, it has a temperature resolution of 0.37 μK which outperforms commercial semiconductor thermometers with commercial instrumentation.

to create a temperature calibration.

The devices were not designed with thermometry in mind but still performed remarkably well. The device demonstrated a usable range of 50 mK (the base temperature of the cryostat) up to 2 K. An analysis of the slope of the voltage vs. temperature and RMS noise near the balancing point of 100 mK produced an energy resolution of 0.37 μK, which is comparable or better than the best readout of commercial semiconductor thermometers with commercial instrumentation.

5.4 Conclusion

This first wafer was a proving ground for the first set of devices designed by UNM and as a test bed for features that could be incorporated into future designs. Devices were varied, including 6 different SQUID designs, 28 sensing coil designs, 5 persistence current circuit designs and 3 different topologies. All the SQUID designs function very well, showing very little difference from each other, and all comparable to the STAR Cryoelectronics commercial SQUIDs. The bulk of the testing occurred on rectangular meander coils, all of which showed good performance. Changing the topology from a segregated sensing coil and excitation coil, to an integrated one did not degrade device performance. The persistence switch design was not successful as it increased noise and was not able to trap persistent current.

Chapter 6

UNM Devices Gen 2: Prototype MMC Arrays

6.1 Overview

This chapter will cover UNM's second generation of devices: multi-pixel MMC arrays. This second generation of devices expands in the developments explored on the first generation of devices. Most importantly, this set of devices are designed to be fully functioning MMCs, rather than experimental paramagnetic sensors. Devices in this generation consist of 7 + 1 SQUIDs arrayed together to create a 14 pixel MMC detector with an on-board paramagnetic thermometer. These arrays include new design features not seen in the first generation such as thermal engineering of the gold fill and passive persistent current switches. This dissertation will cover the initial work in developing these devices into full MMCs, including an attempt to electroplate gold absorbers to the array and an initial Fe-55 spectra taken with a device without absorbers.

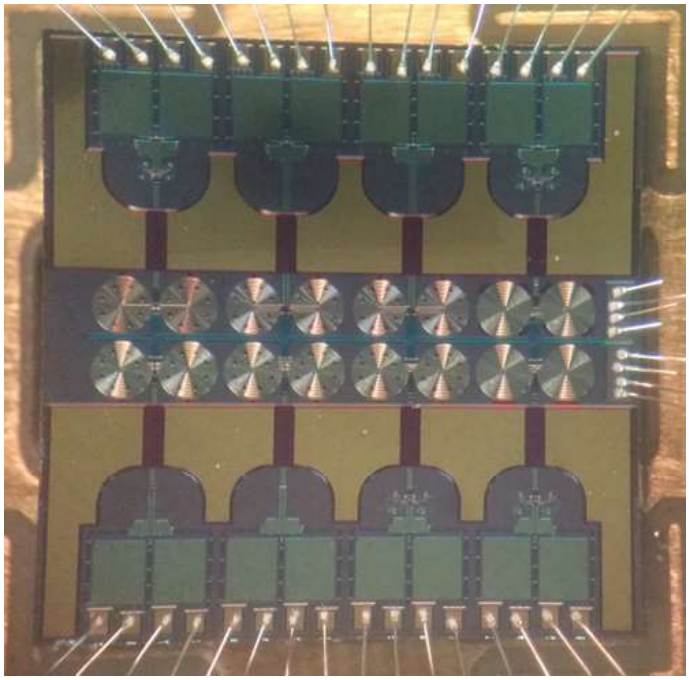

Figure 6.1: A photograph of a wire bonded second generation array, without gold absorbers. This 5 mm x 5 mm array, consists of 8 SQUID devices, 7 of which are MMCs and 1 as a dedicated paramagnetic thermometer, to create a 14 pixel array. The 16 magnetization coils are wired in series and energized by a single pair of leads.

6.2 Design Changes from Gen 1

The second generation of devices combines 8 individual SQUID devices onto one die to create an array of MMCs. Each array is equipped with 7 two-pixel MMCs and 1 paramagnetic thermometer. In the first generation, 4 different SQUID wiring topologies were discussed (see Section 5.3.4). Devices on these arrays are either Design A, SQUID transformer coupled to the magnetization circuit, or Design B, SQUID directly coupled to the magnetization circuit. Designs C and D are not present as the magnetization and persistence current circuits have been redesigned.

All 16 magnetization coils are wired together in series and energized from a single pair of leads. Each gradiometric pair of coils is shunted by a passive persistence

switch, which allows persistent current to be trapped and each pair to be electrically isolated from its neighbors. This change greatly reduces the wiring requirements of energizing 8 generation one devices and their persistent current heaters from 32 leads, down to 2.

A large amount of gold fill spans the array available for thermal engineering. This fill not only allows the entire chip to be thermally anchored to the cryostat, but provides room for thermal links to the gold absorbers. Large structures and links are added during the same gold electroplating stage that is used to place the gold absorbers.

6.2.1 Passive Persistent Current Shunts

The persistence current circuits in the second generation of devices have been completely redesigned from the lessons of the first generation. The most significant change is forgoing the heater activated persistent shunts for a passive approach [51]. The persistence current loop is now shunted with a superconducting link made of a different material, with a different transition temperature from the underlying wiring. With this setup, the entire device is heated above the transition temperature of the shunt, but below the transition temperature of the wiring, to force current into the magnetizing loops. These shunts are made from an alloy of Nb and Ta, with a targeted transition temperature of 5.5 K [51], much lower than the transition temperature of the Nb wiring of 9 K. Figure 6.2 illustrates the use of the shunts in the persistence current circuit for the magnetization coils. Each gradiometric pair of magnetizing coils is shunted, allowing each pair to be its own closed superconducting loop. This imposes noise immunity while simultaneously attenuating any possible cross talk from one gradiometric pair to the other.

No testing of these switches were performed in the course of this dissertation,

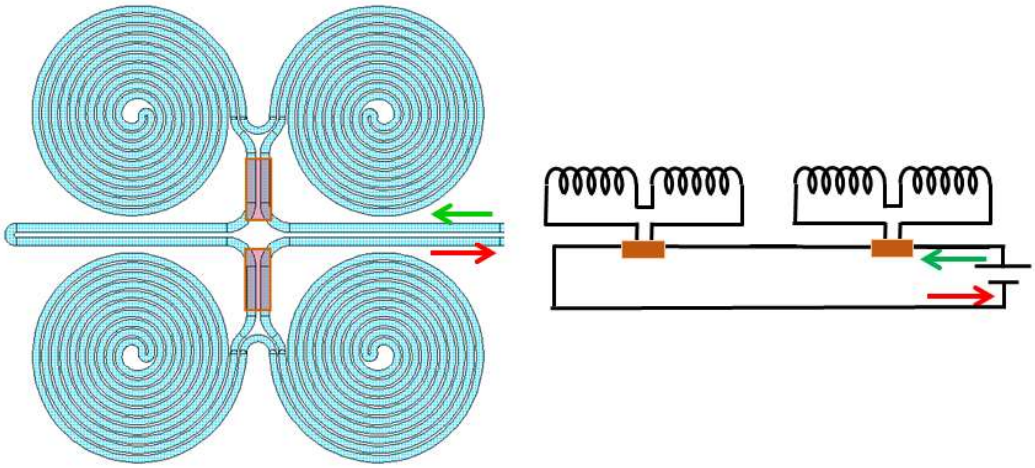

Figure 6.2: A diagram of 4 magnetization coils from a second generation device with the passive persistent current shunts, in brown. When the device is heated above the transition temperature of the shunts, but below the transition temperature of the wiring, external current can be injected into the coils. With the current flowing, the temperature can be lowered back below the transition temperature of the shunts and the gradiometric coil pairs are now isolated superconducting loops. The external current is now trapped, pairwise, in the magnetization coils which are isolated from other pairs.

but only mentioned here to mark the continuation of the work described in the first generation of devices. For a more complete description of the passive persistence circuit please refer to the work of Hummatov *et al.* [51, 58].

6.3 Performance and Testing

The new arrays receive a similar battery of testing to the first generation of devices. Each array is wire bonded to a carrier and dipped in liquid helium to measure SQUID noise, one core at a time. Additionally, as a proof of concept test, a rough Fe-55 spectrum was recorded on an array with paramagnet but without absorbers.

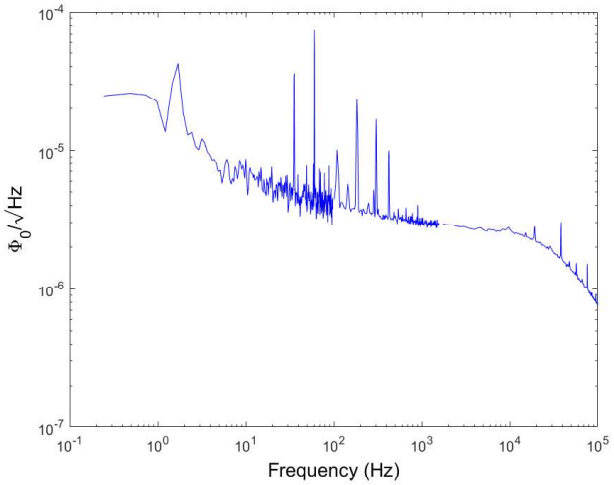

Figure 6.3: Noise spectrum taken from a single 2-pixel device off of a Gen 2 array. This device has 1.55 μm of 1000 ppm Au:Er paramagnet with a 330 nm thick Nb Cap. The noise spectrum was recorded at 4 K with no magnetization current in the paramagnet. A noise of 2.96 $\mu\Phi_0/\sqrt{Hz}$ at 1 kHz was recorded, which is very similar to the noise of similar devices without paramagnet. This device was used to record the Fe-55 spectrum shown in Figure 6.4.

6.3.1 Noise Performance

In order to check the health and performance of these devices, the SQUID cores are tested. The entire array is mounted to a chip carrier and each device is wire bonded to give electrical access. The entire chip is then submerged into liquid helium and the performance of one SQUID core, which services two pixels, is tested at a time. Evaluation of the device is carried out exactly as previously described in Section 5.3.

A noise spectrum taken from a device with 1.55 μm of 1000 ppm Au:Er paramagnet with a 330 nm thick Nb Cap, shown in Figure 6.3. This device was tested in liquid helium without any magnetization current. A noise of 2.96 $\mu\Phi_0/\sqrt{Hz}$ at 1 kHZ was recorded, which is in line with other devices from this generation. Although slightly noisier than the generation 1 devices, less than a factor of 2, they still perform well despite the addition of much more complication.

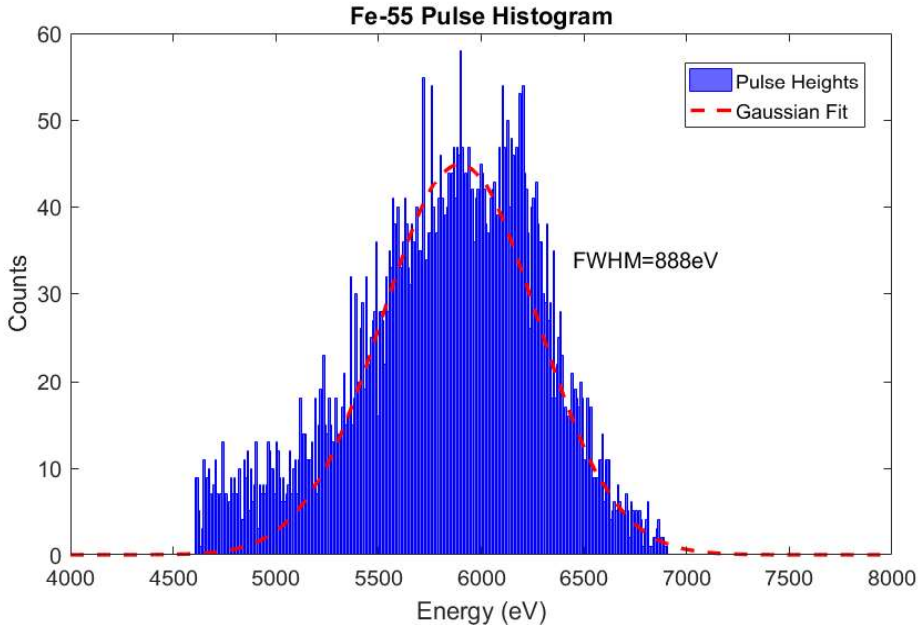

Figure 6.4: A histogram of 7000 Fe-55 pulses recorded from a single two pixel device on an MMC array. The device was prepared with 1000 ppm Au:Er paramagnet but did not include the gold absorbers. The array was cooled to 50 mK and 100 mA of current was trapped to record pulses overnight. The pulse heights are histogrammed and fit to a Gaussian centered at 5895 eV to provide an energy resolution of 888 eV.

6.3.2 Fe-55 Spectrum

In order to demonstrate functionality of the arrays, one array was prepared with 1000 ppm Au:Er paramagnet, 1.55 μm thick, and a Nb Cap, 330 nm thick, to be exposed to Fe-55 particles in the UNM cryostat. This device did not have the gold absorbers, but was still able to record particle impacts by using the paramagnet itself as an absorber. The entire array chip was magnetized with 100 mA of persistent current and cooled to 50 mK. An oversized collimator was placed in front of the devices to try to limit the X-rays impacts off paramagnet from a 1 mCi Fe-55 source, placed 10 cm away.

Due to wiring constraints in the testing setup, only two pixels were recorded for

this trial. Most of the particle events that were recorded were discarded as not all of them hit the paramagnet itself. Any low voltage signals, which were attributed to hits off of the paramagnet, along with pulses that occurred too closely to one another temporally (pile-up events), were omitted from the final data set. After this basic leveling of filtering, a data set that was recorded overnight was distilled down to roughly 7000 pulses remaining for analysis.

A simple analysis was performed on this initial set of data. The height was extracted by fitting two exponentials to the pulse, one to the rise of the pulse and another to the decay of the pulse, then finding the intercept. The height versus number of events was plotted into a histogram and fit to a Gaussian, see Figure 6.4. The Gaussian's peak is set at a value of 5895 eV, the main emission line of Fe-55, and the FWHM is calculated to give a rough energy resolution of 888 eV.

6.4 Array-Wide Electroplated Gold

One of the largest hurdles to overcome with the creation of these new devices is the attachment of electroplated gold features across the entire device, within one plating step. A process, see 4.5.2, was developed to use a two-tiered mold of copper, to define the legs of the absorbers, and the ultra thick photo resist AZ 125nXT, to define the body of the absorbers. After the creation of the two-tiered mold, the device was electroplated in the commercial gold plating solution, Technic 25ES RTU, see 4.6, and plated with 20 μm of gold.

The mold creation and electroplating of the device did not have any anomalies, but problems arose during the removal of the molds. As seen in Fig 6.5, crinkling and peeling of the top-most layer of protective SiO_2 developed. This damage to the oxide layer also spread down into the device layers, rendering those devices unusable. Adhesion of the gold absorbers to the device was also compromised.

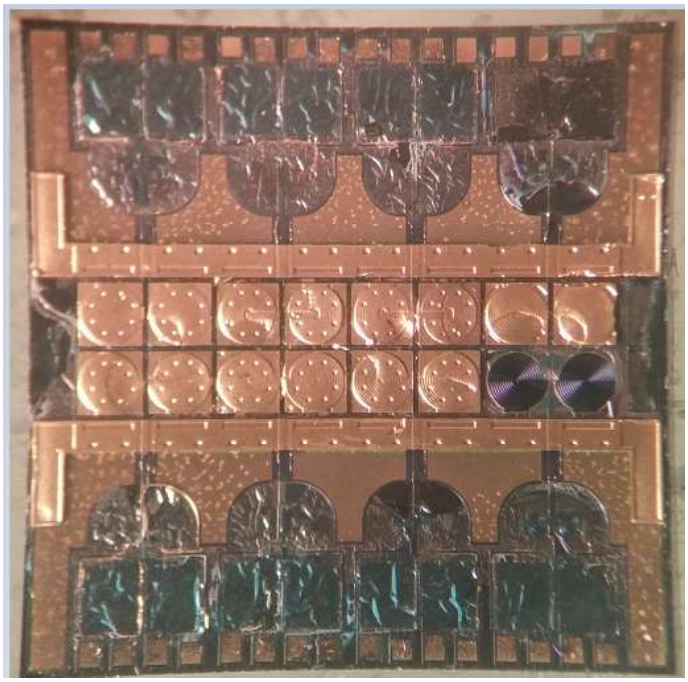

Figure 6.5: A photograph of a second generation array after a failed attempt at gold electroplating. The pixels in the center of the array have absorbers that are 475 μm x 475 μm x 20 μm thick, supported by a ring of 8 x 30 μm diameter x 5 μm tall legs. The bottom right device that does not have absorbers was intentionally left empty, as that is the on board paramagnetic thermometer. Complications with adhesion during the copper mold process, as described in 4.5.2, caused some delamination as evidenced by the crinkling seen at the top and bottom of the device.

These complications prevented the creation of full MMCs with Au Absorbers within the time frame of the work for this dissertation. Alternative approaches for the creation of the absorber molds have been investigated, such as returning to a traditional photoresist in lieu of the copper and switching to a dry, roll-on film resist to replace the thick AZ 125nxT that is used for the absorber molds. This work, carried out by another student in the lab, has shown good success and is documented in his dissertation [58].

6.5 Discussion and Conclusion

A second generation of UNM devices has been fabricated and initial testing has been carried out. These devices build on the lessons of the first generation and are also now 14-pixel arrays consisting of 7 two-pixel devices and 1 paramagnetic thermometer device. Noise testing of the individual two-pixel devices show that the SQUID cores are still high performing and the additional complexities added only slightly degrade the noise performance.

A pixel with 1000 ppm Au:Er paramagnet but without absorbers was tested in with an Fe-55 source and an initial spectra was recorded. Although this spectrum did not resolve the spectrum with a high resolution, it still demonstrated the devices ability to record particle impacts. A full MMC with electroplated gold absorbers was constructed, but complications in the absorber process rendered that device non-functional. Although outside of the time frame for this work, improvements have been explored and full MMC particle detectors from this set of devices have been realized.

Chapter 7

Experimental Setup

7.1 Introduction

In order to fully characterize the detectors described in the previous chapters, they must be cooled to much lower temperatures than liquid helium, alone, can offer. These devices have optimal performance at temperatures below 100 mK and due to their extreme sensitivity, require robust isolation from external sources of electromagnetic and vibrational noise. Devices undergo more thorough testing within the UNM cryostat, which is able to cool and stably hold the devices at 50 mK for over two days. The cryostat is also built as a large Faraday cage to block out electromagnetic signals and is suspended on floating air legs to dampen any vibrations introduced from the external environment. The UNM cryostat has been developed over several years by a number of different people. This chapter will describe the main features of the UNM cryostat and the various cryogenic technology needed to cool the devices for testing. The experimental stage, where the devices are housed and exposed to radioactive sources, will also be discussed.

7.2 Cryostat Overview

The UNM cryostat is a dry cryostat, as it does not use any liquid coolants, such as liquid helium or liquid nitrogen, to get to its base operating temperature. Instead, it is equipped with a two stage pulse tube refrigerator (PTR), that provides a first stage at 65 K and second stage at 4 K. In order to get to a base temperature of 50 mK, the UNM cyrostat is equipped with an adiabatic demagnetization refrigerator (ADR) which resides on the Magnet Stage, that is attached below the 4 K stage.

7.2.1 Support and Vibration Isolation

At the operating temperature of the devices, any mechanical noise, such as vibrations, translate into heating. In order to get the best performance from the devices, not only does the environment have to be electrically quiet, but also mechanically quiet. Although a PTR is a very convenient way to cool the cryostat, it is a mechanical device that does have some motion associated with it. Therefore, the experimental stage needs to be vibrationally isolated from not only the external environment, but also from the PTR cooler.

The UNM cryostat is suspended below a large metal table that is supported by three large wooden columns. These columns are filled with sand, in order to dampen any vibrations that can travel through the ground. The table is supported by 3 air legs that allow it to float with the addition of several lead bricks increasing the mass and moments of inertia of the table, helping to mitigate any vibrations coming in from the room. Figure 7.1 shows the support system.

To reduce vibrations that come from the PTR, the two temperature stages of the PTR are not directly coupled to the corresponding temperature stages of the cryostat. Instead, the heat is transfered via helium gas within an exchange gas volume (XGV).

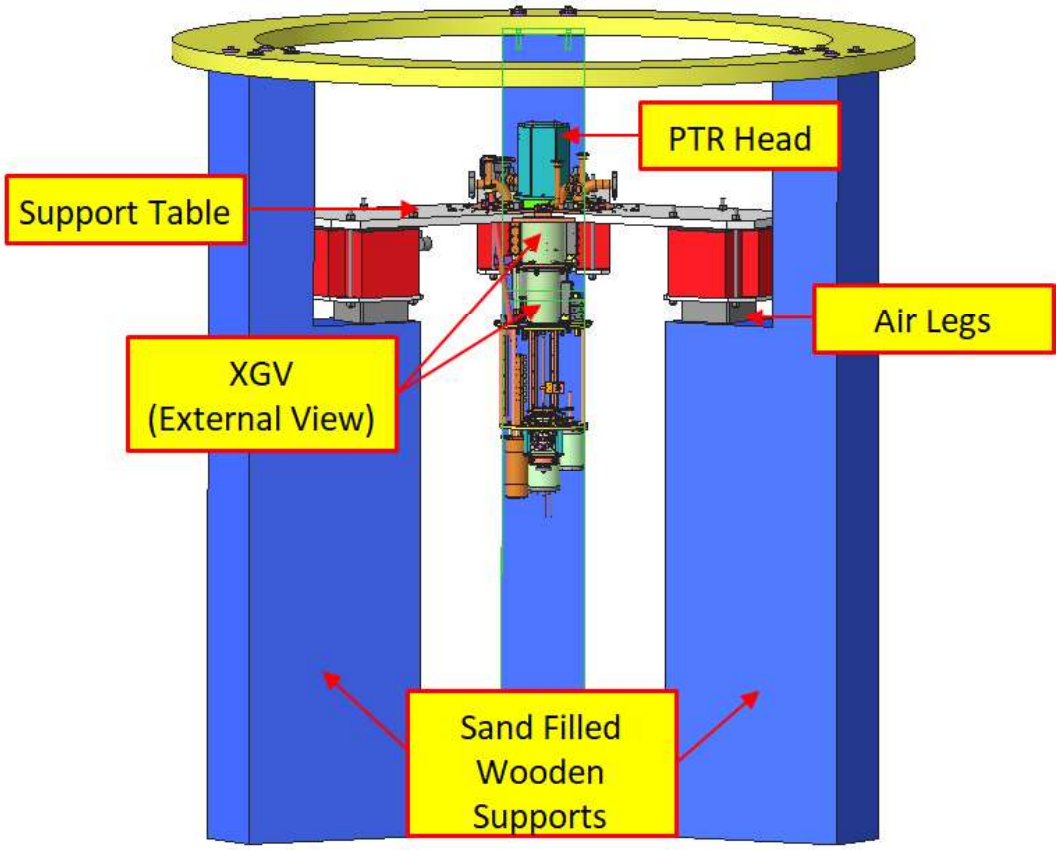

Figure 7.1: A 3D model of the cryostat and its vibrational isolation support frame. The PTR head is placed within the XGV, which is supported on an aluminum table, that sits on air legs to float it. The table is held up by three wooden supports, which are filled with sand to offer extra vibrational dampening.

An array of fins are attached to the two stages of the PTR and placed in a cylindrical volume. Penetrating that vessel are another set of fins that are attached to the cold stages of the cryostat. These fins are aligned such that they are interdigitated, but do not actually touch. The cylinder is filled with a partial pressure of helium to facilitate heat transfer. This allows the PTR to be mechanically separated from the cryostat, except for the weak contact point around the seal of the cylindrical volume. Figure 7.2 shows how the fins are aligned within the XGV and an example of a fin that is attached to the PTR cold head itself.

7.2.2 Vacuum and Thermal Radiation Protection

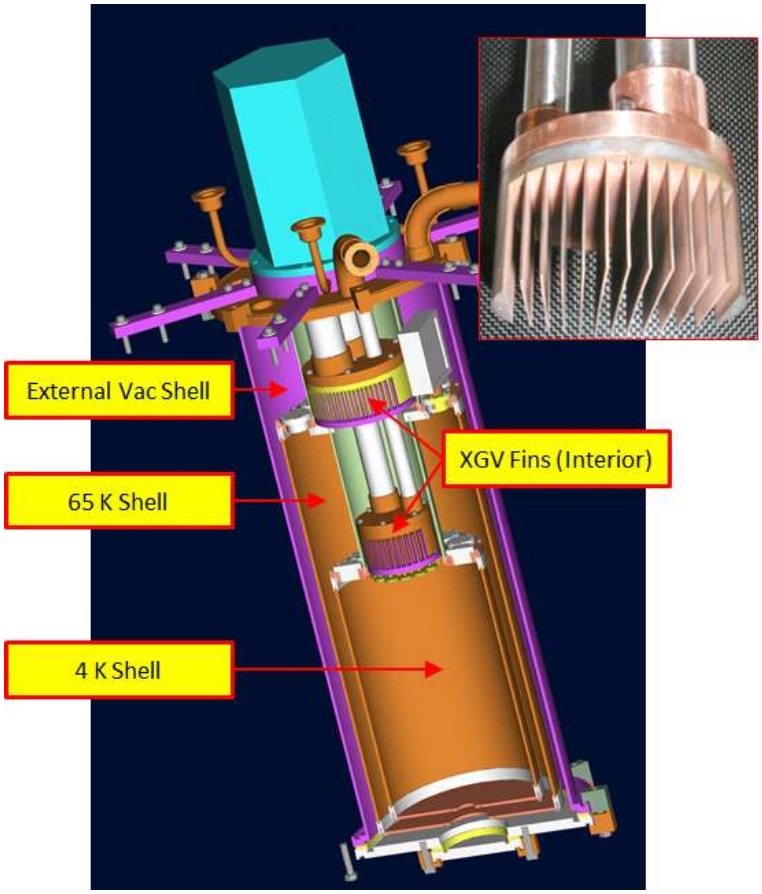

Figure 7.2: A 3D model of the UNM Cryostat showing the various vacuum shells that protect the interior. Also shown is an interior view of the XGV, highlighting the interdigitated fins that allow for heat transfer between the PTR and cold stages. The inset to the right is a photograph of one such exchanger that is mounted to the 4 K Stage of the PTR.

The cryostat is thermally and electrically shielded by three concentric aluminum shells that are attached to the three main stages of the PTR, as seen in Figure 7.2. The outermost shell is a large and heavy vacuum shell that attaches at room temperature. This shell has a vacuum port that allows the cryostat to be pumped out and run under vacuum to reduce heat transfer from any gases inside. The second shell, which attaches to the 65 K Stage, is wrapped with aluminized Mylar to reflect

thermal radiation from the room temperature outer shell. The innermost shell is attached below the 4 K Stage and surrounds the Magnet Stage. This shell, in addition to the aluminized Mylar on its exterior, also has a thin liner of Nb on the inside that acts as a superconducting shield to block any external magnetic fields. All three shells act as Faraday cages to improve the electrical isolation of the devices inside.

7.2.3 Cold Stages

The cryostat has the largest and warmest stages at the top and the colder, smaller stages below. As shown in Figure 7.1, there is a large table at room temperature, which supports the PTR cold head and has ports for all wiring to enter the cryostat. Figure 7.3 shows the cryostat from below this support table. The first stage is at 65 K and below that, the second stage is at 4 K. Both of these stages serve as thermal anchor points for wiring that extends further into the cryostat. Underneath the 4 K Stage is the Magnet Stage, which is attached to the 4 K Stage via 5 large copper bars, which provide adequate thermal contact. The Magnet Stage itself support 3 additional temperature stages of 1.2 K, 250 mK, and 50 mK.

To achieve 1.2 K, a single shot liquid helium "1 K pot" is used. The 1 K pot is a cylindrical copper vessel which is attached to the Magnet Stage that can hold approximately 1 L of liquid helium. Helium gas is fed to the 1 K pot from room temperature, where it is allowed to condense. Thermal contact to the 1 K pot and the Magnet Stage is provided by a solenoid-driven mechanical heat switch. This heat switch compresses two copper shoes, which are connected to the Magnet Stage at 4 K, to a copper tongue that is connected to the 1 K pot. After filling the 1 K pot to capacity, the heat switch is opened, breaking the thermal contact and isolating the 1 K pot from the 4 K Magnet Stage. The helium inlet line is then attached to a rough vacuum pump and evacuated, lowering the collected liquid helium's temperature

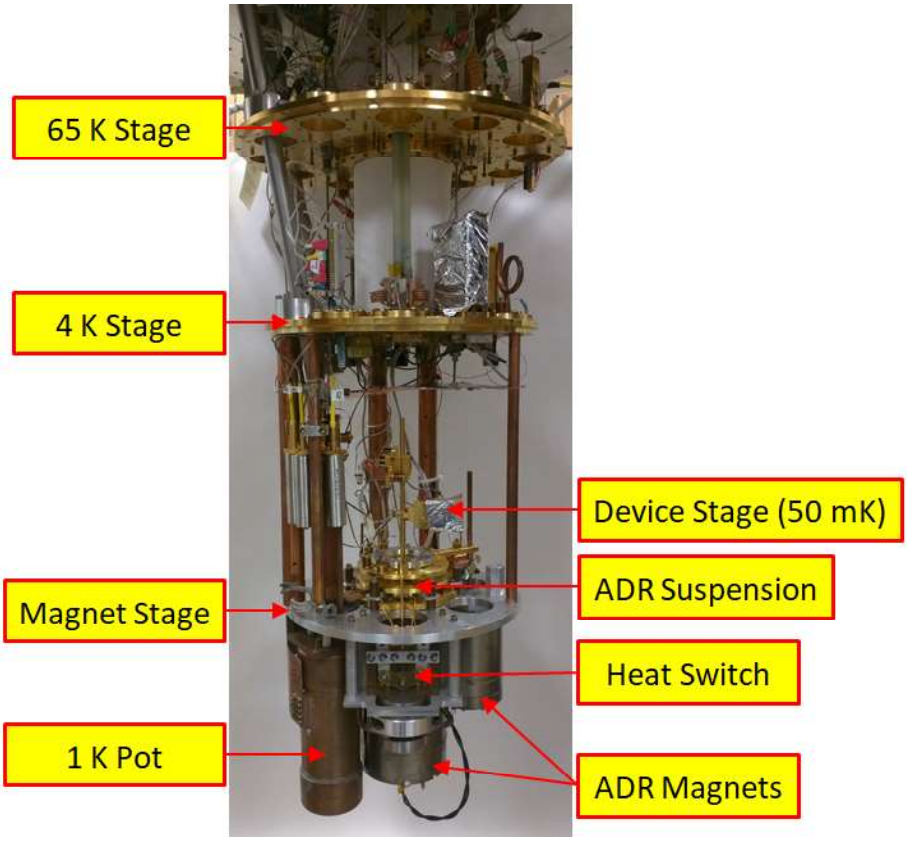

Figure 7.3: A photograph of the cryostat without any of the protective shells. Above (not shown) is the floating support table that holds the pulse tube refrigerator (PTR) cold head. The temperature decreases from top to bottom, starting with the 65 K Stage, the 4 K Stage, the Magnet Stage (4K) and Device Stage (50 mK). The adiabatic demagnetization refrigerator (ADR) magnets sit below the Magnet Stage and house the paramagnetic crystals. These crystals have rods that extend up past the magnets to allow attachment of the Device Stage.

from 4 K to 1.2 K. It takes approximately 24 hours to condense a full charge of liquid helium, which can then be used continuous for 5 days.

The 250 mK and 50 mK stages are attached to the ADR suspension and cooled by two paramagnetic crystals, gadolinium gallium garnet (GGG) for 250 mK and chromium potassium alum (CPA) or ferrious ammonium alum (FAA) for 50 mK. The ADR and its suspension are described in the following sections.

7.3 Adiabatic Demagnetization Refrigerator

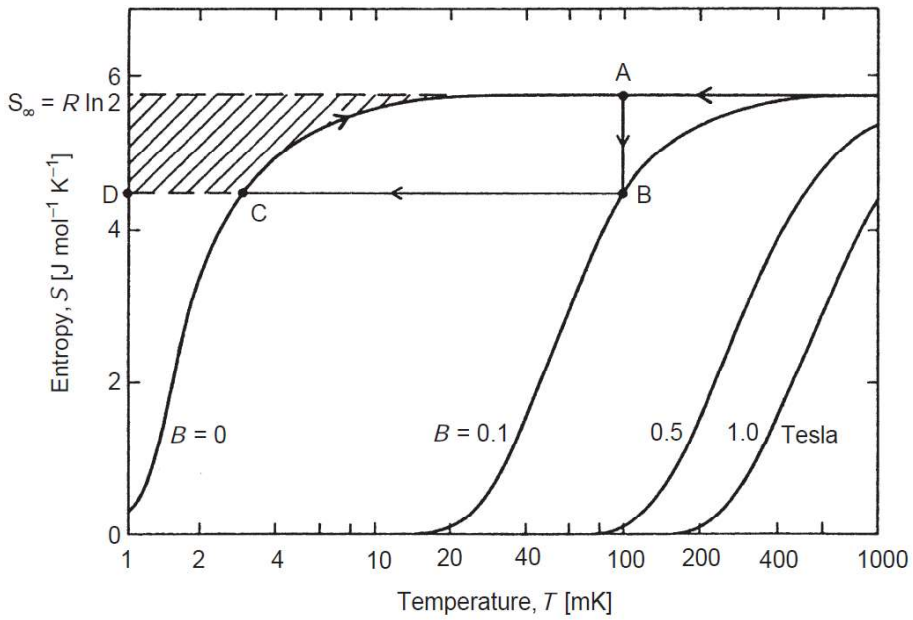

Figure 7.4: A plot of the entropy of a paramagnetic crystal (Chromium Manganese Nitrate) as a function of temperature for several different values of an externally applied magnetic field. The entropy of the magnetic moments, for a given external magnetic field, follows the curves. For adiabatic demagnetization refrigeration, the paramagnet is magnetized isothermally (A to B) before being thermally isolated. The magnetic field can then be reduced adiabatically (B to C) and the temperature of the paramagnet will decrease. Graphics reproduced from F. Pobell [6].

The PTR is used to cool the cryostat down to 4 K, and the 1 K pot provides cooling down to 1.2 K, but the experiment is performed at 50 mK. In order to cool the devices below 1.2 K, an adiabatic demagnetization refrigerator is used. The ADR relies on the magnetic disorder entropy of a paramagnetic system for refrigeration. As the temperature of the paramagnet is decreased, the interaction energy of the magnetic moments approaches $k_B T$, causing the magnetic moments to spontaneously order. As the temperature continues to decrease, and the ordering increases, the entropy will eventually drop to zero. Applying an external magnetic field to the system will cause the magnetic moments to partially align to the applied field. This

alignment puts the magnetic moments in a more ordered state, lowering the entropy of the system for a given temperature, as illustrated in Figure 7.4. Therefore, taking a paramagnetic system at temperature T and applying a magnetic field to it will decrease its entropy. If the paramagnet is magnetized isothermally (A to B), by allowing the heat to flow into the temperature bath at T, and then thermally isolated, the magnetic field can be reduced adiabatically (B to C) and the temperature of the paramagnet will decrease.

Attached below the 4 K Stage is the Magnet Stage, aptly named as it not only supports the experimental stage but also the two 50 A, 4 T, superconducting magnets that power the ADR. Although the UNM cryostat is equipped with two magnet stages, it is presently not being used as a true two-stage ADR. The heat switches are parallel, rather than in series, and the magnets are also connected in series. The main ADR, where the experiment stage is attached, uses either the paramagnetic crystal chromium potassium alum (CPA) or ferrous ammonium alum (FAA). As seen in Figure 7.5, this crystal is housed in a stainless steel enclosure that sits within the bore of the central superconducting magnet. A gold plated copper rod is attached to the end of the canister, which extends up past the magnet, allowing the attachment of the Device Stage. The second ADR uses the crystal gadolinium gallium garnet (GGG) which reaches a base temperature of 250 mK and is used as a thermal guard to the Device Stage that sits at 50 mK.

The ADR requires a suspension system that mechanically supports the paramagnetic crystals while keeping them thermally isolated as seen in Figure 7.6. The UNM cryostat uses a unique suspension that is made a stack of 5 metal plates that are separated from each other with columns of sapphire disks with sapphire powder between them. The stacks and disks are clamped together with metal screws, which allows the suspension to be mechanically robust while still having strong thermal isolation due to the sapphire disk stacks. The suspension supports 3 different tem-

Figure 7.5: A photograph of a paramagnetic crystal canister outside of the ADR magnet bore. The crystal material is housed within the stainless steel canister and the gold plated copper rod extends past the magnet bore to allow attachment of experiments. A wires brush of 100 wires inside the canister are used to make thermal contact from the crystal within to the copper rod.

perature stages: 1.2 K on the top and bottom plates, 250 mK on the middle two stages, and 50 mK on the central stage. More detail about the construction and testing of the suspension can be found in R. Hummatov's PhD dissertation [58].

7.3.1 ADR Cooling Cycle

This section will briefly describe the ADR cycle used in the UNM cryostat to cool the devices to 50 mK. The two ADR paramagnetic crystals are held separately from each other via the suspension system that was described above. Each rod end of the paramagnetic crystals has a copper tongue that allows establishment of a thermal link. These tongues extend to a solenoid-driven mechanical heat switch that clamps them between two copper shoes thermally linking them to the 1 K pot. The heat switch is opened before cooling the crystals to thermally isolate them from the cryostat and each other.

While attached to the 1 K pot, the two superconducting magnets are slowly energized to 4 T. After the crystals expel all their heat and cool back to 1.2 K,

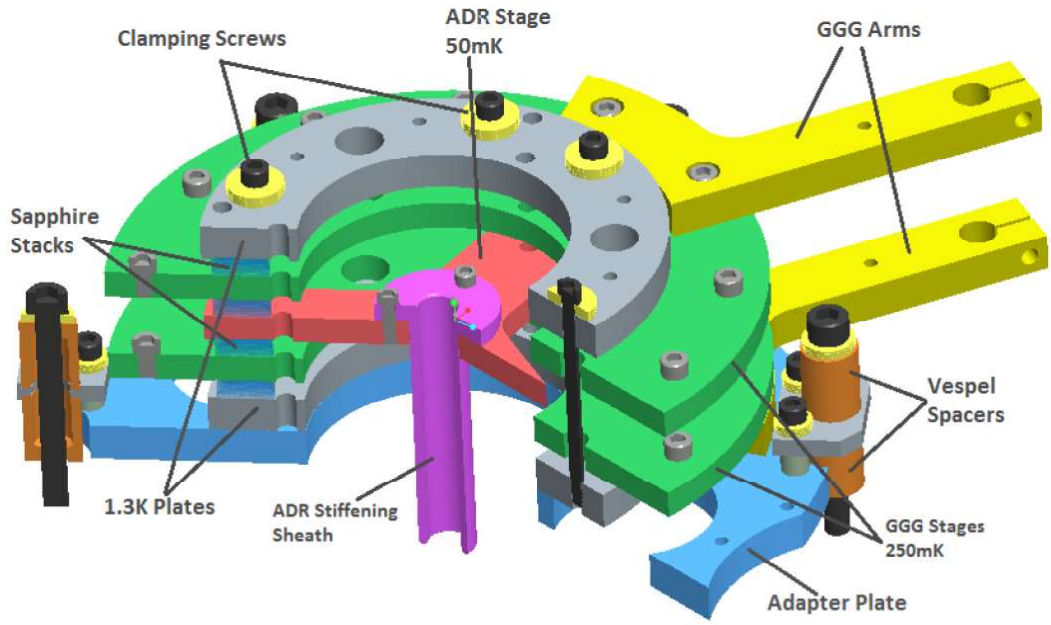

Figure 7.6: A 3D model and cross section of the Sapphire Stack ADR suspension. The suspension is made up of 5 differently shaped copper stages that are clamped together between columns of sapphire disk-sapphire powder-sapphire disk structures that allow the suspension to be mechanically robust but still achieve thermal isolation between the disks. The suspension has 3 temperature stages: 50 mK, in the center in red, 250 mK on top and bottom of the central stage in green, and 1.3 K, which are attached to the 1 K pot, as the outermost 2 stages seen in gray. The entire suspension is thermally isolated from the Magnet Stage via Vespel spacers.

the mechanical heat switch is opened, isolating the crystals from the 1 K pot and each other. Once isolated, the magnetic field is slowly lowered back to zero, over the course of half an hour, and the crystals begin to cool. The GGG crystal will reach a temperature of 250 mK and the central FAA or CPA crystal will reach the experiment temperature of 50 mK. It is worth noting that a temperature of 50 mK can be reached even starting at 4 K, but starting at 1.2 K extends the holding time at 50 mK to over 2 days.

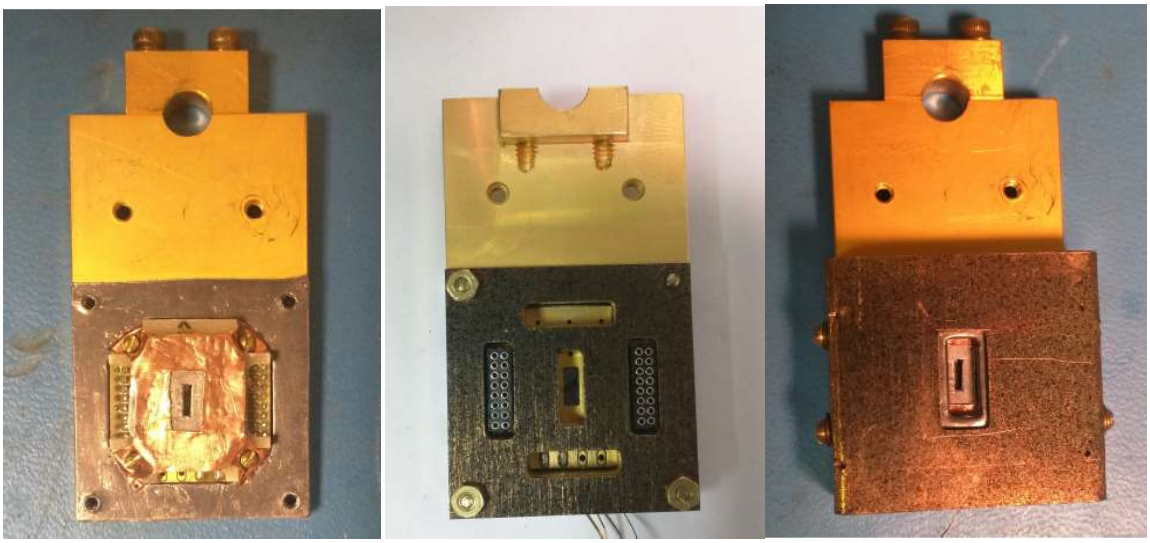

(a) Device Stage with Array (b) Device Stage (Bottom View) (c) Covered Device Stage

Figure 7.7: **(a)**: Top view of the device stage with a device mounted. The device sits on top of a sheet of lead as part of the protective shielding. The clamp at the top is used to secure the stage to the ADR copper rod. **(b)**: The underside of the Device Stage. Connectors from the PCB can be seen. A wiring harness is plugged into the bottom of the stage to allow electrical access to the devices. The gray mu-metal shield can be seen. **(c):** The Device Stage with its full protective cover attached. A lead cover is placed over the arrays before the mu-metal cover (as seen) is attached. Windowing to allow particles for detection to enter is shown.

7.4 Device Stage

The Device Stage is a gold plated copper platform that is clamped onto the gold plated copper rod that extends from the central ADR paramagnetic crystal of CPA or FAA. It is designed to hold one array of MMC devices and all the wiring required to operate it. The devices are covered in a superconducting shell, to shield from external magnetic fields, that is also windowed to allow particles from a nearby radioactive source to be detected. Signals from the array are amplified through a Star Cryoelectronics commercial SQUID array and recorded at room temperature.

Further description and construction of the Device Stage can be found in the PhD dissertation of R. Hummatov [58]. A brief description of the stage will be provided here for completeness.

The devices are attached and wired bonded to a custom printed circuit board (PCB) that mates onto a matching PCB on the stage. Using PCBs allows for quick and easy exchange of devices while also organizing the many wires required to run them. To shield the devices from external thermal radiation and magnetic fields, it is enclosed within a multilayer box. A layer of lead is used to surround the device as a superconducting shield to block any external magnetic fields. Surrounding the lead box is another box made from the mu metal Cryoperm12, a material that has high magnetic permeability. The mu metal box intercepts and redirects any magnetic fields that may have been present before the lead transitions into the superconducting state, preventing flux pinning into the lead shield. Figure 7.7 shows the Device Stage, PCB, and shielded box.

The shielding around the devices has a window cut into to allow particles from a nearby radioactive source to hit the detector. For the tests described in the previous chapter, the Device Stage sat 10 cm below an Fe-55 source that was mounted at 4 K. The 1 mCi source was housed in an aluminum shell with a window of Kapton to protect and contain it, while still allowing transmission of the x-rays. A rotary motor, mounted on the Magnet Stage, rotated a disk of aluminum over the top of the window to shutter particles.

To magnetize the paramagnet, the devices have to be above 4 K, where the passive persistent-current switch across the magnetization coils is in the normal state, but the coils themselves are still in the superconducting state. A battery operated, op-amp driven, current source at room tempertaure, slowly applies 100 mA of current into the magnetization circuit. Once the coils are charged, the devices are cooled to 1.2 K, which is below the transition temperature of the switch, and the external

current source is slowly decreased back to zero. Since the shunt is superconducting, the magnetization circuit is a completely superconducting loop, flux conservation traps the applied current within the coils. The now charged devices are then cooled to the base temperature of 50 mK and the shutter is moved to allow the devices to collect data.

Chapter 8

Conclusion

8.1 Summary

The accurate measurement of isotopic concentrations in radioactive materials, such as the ratio of Pu-239 to Pu-240, is of great concern to the fields of nuclear forensics and nuclear safeguards. There is a technology shift from using destructive assays, such as mass spectrometry, to a non-destructive assay, such as γ-ray spectroscopy. The benchmark technology for γ-ray spectroscopy, the HPGe detector, does not have a high enough energy resolution to give an accurate ratio of Pu-239 to Pu-240. Cryogenic Microcalorimeters, which do not have some of the fundamental limitations that HPGe does, are a technology that can resolve the γ-ray spectra much more effectively than the HPGe detectors.

The two microcalorimeter technologies used for γ-ray spectrometry are the transition edge sensor (TES) and the metallic magnetic calorimeter (MMC). The TES is the more mature technology of the two, showing high energy resolution and has been constructed into large arrays of detectors. The MMC is still in development, but has recently been shown to surpass the energy resolution of the TES. The TES

has a few fundamental issues, such as the Joule heating generated during operation and the complexity of the physics governing the measurements, that the MMC does not, placing the MMC on a firm footing to surpass the TES as leading detector.

The paramagnetic system currently used in MMCs is a dilute mixture of erbium in a gold matrix. While this material has been shown to work very well, as the detectors themselves improve, new issues with the paramagnet have been discovered. Namely, the heat capacity of Au:Er has been shown to increase at temperatures below 100 mK. This behavior degrades the performance of the devices at low temperatures, even though low temperatures are otherwise needed to improve MMC performance. This increased heat capacity is attributed to the nuclear electric quadrupole moment of gold interacting with the electric field from the erbium ions. This can be remedied by using silver instead of gold, as neither of the two naturally occurring isotopes of silver have a nuclear electric quadrupole moment.

However, silver is a more difficult material than gold to process because it has a high affinity for oxygen. Excess oxygen during synthesis of the paramagnetic alloy can oxidize the erbium ions, which would change their magnetic properties. In order to create high-performing samples of Ag:Er, a vacuum induction furnace was developed. This system processes the alloy in an airtight chamber that can be evacuated and filled with purified argon gas. An induction heater heats the sample from the outside of the vacuum chamber, increasing the cleanliness of processing. The system can also tilt and rotate the samples, providing a "cement mixer" action to homogenize large samples in a single operation. Ag:Er made in this furnace has been tested in a Quantum Design MPMS and found to have good uniformity throughout a 1" diameter sputtering target with the targeted magnetic properties.

The UNM group has been developing an MMC that integrates the SQUID and parmagnetic sensor onto a single chip. This will improve the coupling of paramagnet to the sensor, which will improve detector performance. The cost of this change is

the increased complexity of design and possible heating due to power dissipated in the SQUID shunt resistors. The SQUID itself is sensitive to environmental factors, which forces the chips to be processed below 150° C and without harsh chemicals. This is most apparent when trying to attach gold absorbers to the paramagnet. The absorbers cannot be attached with high temperature techniques such as welding or soldering. In order to create absorbers, a two-mold system has been developed to electroplate the absorbers directly onto the devices as electroplating can be done at 50-60° C and there are solutions that are chemically mild and compatible with other microfabrication technologies, such as photoresist. The two-mold system uses an ion-milled copper layer that defines the legs of the absorbers with the ultra thick photoresist AZ125 nXT to define the body of the absorbers.

Two generations of devices were developed in the course of this work. The first generation explored the base SQUID magnetometer that is used to read the paramagnet sensor. A wide array of design variants, including changes to the SQUID, coils, and magnetization circuit were explored. A proof of concept device was created and tested, marrying the SQUID sensor with a paramagnet of Au:Er onto one chip as a paramagnetic thermometer. This thermometer device was successfully able to reproducibly measure the change in magnetization of the alloy, creating a high performing thermometer on a device that was not optimized to be a thermometer.

The second generation of devices were arrays of detectors, based on the first generation. The arrays are 14-pixel MMCs that consist of 7 two-pixel devices and 1 paramagnetic thermometer. The magnetization coils for the devices are connected in series to ensure that all pixels are magnetized at the same current and to reduce the wiring required. A new approach in the persistence current circuit was implemented on this wafer. Instead of using heater-activated persistence current switches, as the first generation and other devices have done before, a passive approach was used. A link of superconducting material, with a superconducting transition temperature

lower than the niobium wiring, was used to shunt each gradiometric pair of magnetizing coils, allowing each pair to be a closed superconducting loop. This imposes noise immunity while simultaneously attenuating any possible cross talk from one gradiometric pair to the other. An array with paramagnet but no absorbers was created to demonstrate particle detection with these arrays and a spectrum of an Fe-55 source was shown. An attempt to attach absorbers to these arrays did not succeed.

8.2 Future Work

The second generation of devices did not get a full battery of testing within the time frame of this dissertation. The next natural step is to diagnose and fix the absorber attachment issues that caused failure during the electroplating process described in Chapter 6.4 and create a full MMC. The UNM Cryostat is not currently equipped to readout the entire array. This limits the potential tests that could be performed, therefore a wiring upgrade or a secondary cryostat devoted to device testing is required. This dissertation described the creation of a paramagnetic alloy of silver and erbium and initial measurements of the alloy, but it had not been used in a full MMC detector as of the end of this work. Au:Er was used to compare the devices one-to-one with other published works, but Ag:Er would be the next step after establishing a baseline performance.

During the writing of this dissertation, a full MMC was created from a second generation devices [59]. This device has 30 μm thick electroplated gold absorbers that were created with the improved two-mold system that was described in Chapter 6.4. This device used Ag:Er paramagnet created in the induction vacuum furnace and was able to record the 59.5 keV line from an ^{241}Am source with an outstanding energy resolution of 37.5 eV FWHM at 10 mK.

References

[1] C. Bates, C. Pies, S. Kempf, D. Hengstler, A. Fleischmann, L. Gastaldo, C. Enss, and S. Friedrich, "Direct detection of Pu-242 with a metallic magnetic calorimeter gamma-ray detector," *Journal of Low Temperature Physics*, vol. 184, no. 1-2, pp. 351–355, 2016.

[2] K. D. Irwin and G. C. Hilton, "Transition-edge sensors," in *Cryogenic particle detection*, pp. 63–150, Springer, 2005.

[3] A. Fleischmann, C. Enss, and G. Seidel, "Metallic magnetic calorimeters," in *Cryogenic particle detection*, pp. 151–216, Springer, 2005.

[4] C. Enss, A. Fleischmann, T. Görlach, Y. Kim, G. Seidel, and H. Braun, "Thermalization of magnetic calorimeters," in *AIP Conference Proceedings*, vol. 605, pp. 71–74, AIP, 2002.

[5] P. Eckerlin and H. Kandler, "AlC-ErC," in *Structure Data of Elements and Intermetallic Phases*, pp. 79–93, Springer.

[6] F. Pobell, *Matter and Methods at Low Temperatures*, ch. 9 Refrigeration by Adiabatic Demagnetization of a Paramagnetic Salt. Springer-Verlag, 2007.

[7] W. Sutcliffe and T. Trapp, "Extraction and utility of reactor-grade plutonium for weapons of mass destruction," *Lawrence Livermore National Laboratory*, April, 1995.

[8] M. May, R. Abedin-Zadeh, D. Barr, A. Carnesale, P. E. Coyle, J. Davis, W. Dorland, W. Dunlop, S. Fetter, A. Glaser, *et al.*, "Nuclear forensics: role, state of the art, and program needs," *American Association for the Advancement of Science and the American Physical Society, Washington, DC*, 2008.

[9] D. McCammon, "Thermal equilibrium calorimeters–an introduction," in *Cryogenic particle detection*, pp. 1–34, Springer, 2005.

[10] F. Pobell, *Matter and Methods at Low Temperatures*, ch. 3.1.2 Metals. Springer-Verlag, 2007.

[11] T. Niinikoski and F. Udo, "Cryogenic detection of neutrinos," *European Organization for Nuclear Research*, vol. 74, no. 6, 1974.

[12] S. Moseley, J. C. Mather, and D. McCammon, "Thermal detectors as x-ray spectrometers," *Journal of Applied Physics*, vol. 56, no. 5, pp. 1257–1262, 1984.

[13] F. J. Low, "Low-temperature germanium bolometer," *Journal of the Optical Society of America*, vol. 51, no. 11, pp. 1300–1304, 1961.

[14] D. McCammon, "Semiconductor thermistors," *Cryogenic particle detection*, pp. 3–23, 2005.

[15] D. Andrews, R. Fowler, and M. Williams, "The effect of alpha-particles on a superconductor," *Physical Review*, vol. 76, no. 1, p. 154, 1949.

[16] W. Seidel, G. Forster, W. Christen, F. Von Feilitzsch, H. Göbel, F. Pröbst, and R. Mößbauer, "Phase transition thermometers with high temperature resolution for calorimetric particle detectors employing dielectric absorbers," *Physics Letters B*, vol. 236, no. 4, pp. 483–487, 1990.

[17] K. Irwin, "An application of electrothermal feedback for high resolution cryogenic particle detection," *Applied Physics Letters*, vol. 66, no. 15, pp. 1998–2000, 1995.

[18] D. Parker and L. Corruccini, "Recent advances in thermometry below 0.1 K," *Cryogenics*, vol. 15, no. 9, pp. 499–507, 1975.

[19] M. Bühler and E. Umlauf, "A magnetic bolometer for single-particle detection," *Europhysics Letters*, vol. 5, no. 4, p. 297, 1988.

[20] S. Bandler, C. Enss, R. Lanou, H. Maris, T. More, F. Porter, and G. Seidel, "Metallic magnetic bolometers for particle detection," *Journal of Low Temperature Physics*, vol. 93, no. 3, pp. 709–714, 1993.

[21] J. Adams, S. Bandler, C. Enss, A. Fleischmann, S. Hunklinger, Y. Kim, J. Schönefeld, and G. Seidel, "Particle detection using cryogenic magnetic calorimeters," *Physica B: Condensed Matter*, vol. 263, pp. 604–606, 1999.

[22] G. C. Hilton, J. M. Martinis, K. D. Irwin, N. F. Bergren, D. A. Wollman, M. Huber, S. Deiker, and S. Nam, "Microfabricated transition-edge X-ray detectors," *IEEE Transactions on Applied Superconductivity*, vol. 11, no. 1, pp. 739–742, 2001.

[23] A. Fleischmann, L. Gastaldo, S. Kempf, A. Kirsch, A. Pabinger, C. Pies, J.-P. Porst, P. Ranitzsch, S. Schäfer, F. v. Seggern, *et al.*, "Metallic magnetic calorimeters," in *AIP Conference Proceedings*, vol. 1185, pp. 571–578, AIP, 2009.

[24] S. Kempf, A. Ferring, A. Fleischmann, and C. Enss, "Direct-current superconducting quantum interference devices for the readout of metallic magnetic calorimeters," *Superconductor Science and Technology*, vol. 28, no. 4, p. 045008, 2015.

[25] G. F. Knoll, *Radiation Detection and Measurement*, ch. 8 Scintillation Detection Principles. John Wiley & Sons, 2010.

[26] P. Lerch and A. Zehnder, "Quantum Giaever detectors: STJs," in *Cryogenic particle detection*, pp. 217–266, Springer, 2005.

[27] B. A. Mazin, *Microwave kinetic inductance detectors*. PhD thesis, California Institute of Technology, 2005.

[28] Y. Zhao, C. Allen, M. Amiri, J. Appel, E. Battistelli, B. Burger, J. Chervenak, A. Dahlen, S. Denny, M. Devlin, *et al.*, "Characterization of transition edge sensors for the Millimeter Bolometer Array Camera on the Atacama Cosmology Telescope," in *Millimeter and Submillimeter Detectors and Instrumentation for Astronomy IV*, vol. 7020, p. 70200O, International Society for Optics and Photonics, 2008.

[29] H. Tatsuno, W. B. Doriese, D. A. Bennett, C. Curceanu, J. W. Fowler, J. Gard, F. P. Gustafsson, T. Hashimoto, R. S. Hayano, J. P. Hays-Wehle, *et al.*, "Absolute energy calibration of x-ray TESs with 0.04 eV uncertainty at 6.4 keV in a hadron-beam environment," *Journal of Low Temperature Physics*, vol. 184, no. 3-4, pp. 930–937, 2016.

[30] N. Hoteling, M. Bacrania, A. Hoover, M. Rabin, M. Croce, P. Karpius, J. Ullom, D. Bennett, R. Horansky, L. Vale, *et al.*, "Issues in energy calibration, nonlinearity, and signal processing for gamma-ray microcalorimeter detectors," in *AIP Conference Proceedings*, vol. 1185, pp. 711–714, AIP, 2009.

[31] M. Strongin, O. Kammerer, and A. Paskin, "Superconducting transition temperature of thin films," *Physical Review Letters*, vol. 14, no. 23, p. 949, 1965.

[32] N. Werthamer, "Theory of the superconducting transition temperature and energy gap function of superposed metal films," *Physical Review*, vol. 132, no. 6, p. 2440, 1963.

[33] T. Chui, D. Swanson, M. Adriaans, J. Nissen, and J. Lipa, "Temperature fluctuations in the canonical ensemble," *Physical review letters*, vol. 69, no. 21, p. 3005, 1992.

[34] F. Pobell, *Matter and Methods at Low Temperatures*, ch. 3.1.5 Magnetic Specific Heat. Springer-Verlag, 2007.

[35] A. Fleischmann, J. Schönefeld, J. Sollner, C. Enss, J. Adams, S. Bandler, Y. Kim, and G. Seidel, "Low temperature properties of erbium in gold," *Journal of low temperature physics*, vol. 118, no. 1-2, pp. 7–21, 2000.

[36] L. Tao, D. Davidov, R. Orbach, and E. Chock, "Hyperfine splitting of Er and Yb resonances in Au: A separation between the atomic and covalent contributions to the exchange integral," *Physical Review B*, vol. 4, no. 1, p. 5, 1971.

[37] J. H. Hubbell and S. M. Seltzer, "Tables of X-ray mass attenuation coefficients and mass energy-absorption coefficients 1 keV to 20 MeV for elements Z= 1 to 92 and 48 additional substances of dosimetric interest," tech. rep., National Inst. of Standards and Technology-PL, Gaithersburg, MD (United States). Ionizing Radiation Div., 1995.

[38] A. Raizman, J. Suss, D. Seidman, D. Shaltiel, V. Zevin, and R. Orbach, "EPR study of cold-worked dilute gold-erbium alloys," *Journal of Applied Physics*, vol. 50, no. B11, pp. 7735–7737, 1979.

[39] C. Pies, A. Pabinger, S. Kempf, A. Fleischmann, L. Gastaldo, C. Enss, B. Young, B. Cabrera, and A. Miller, "Metallic magnetic calorimeters for high precision QED tests at GSI/FAIR," in *AIP Conference Proceedings*, vol. 1185, pp. 603–606, AIP, 2009.

[40] J. Simons, "The solutions of oxygen in silver," *The Journal of Physical Chemistry*, vol. 36, no. 2, pp. 652–657, 1932.

[41] S. Group, *PS2-GC50-R/N Specification Guide*.

[42] M. Ketchen and J. Jaycox, "Ultra-low-noise tunnel junction dc SQUID with a tightly coupled planar input coil," *Applied Physics Letters*, vol. 40, no. 8, pp. 736–738, 1982.

[43] STP Boyd and R. Cantor, "Microcalorimeter magnetic sensor geometries using superconducting elements," in *AIP Conference Proceedings*, vol. 1185, pp. 595–598, AIP, 2009.

[44] S. Smith, J. Adams, C. Bailey, S. Bandler, J. Chervenak, M. Eckart, F. Finkbeiner, R. Kelley, C. Kilbourne, F. Porter, *et al.*, "Small pitch transition-edge sensors with broadband high spectral resolution for solar physics," *Journal of Low Temperature Physics*, vol. 167, no. 3-4, pp. 168–175, 2012.

[45] R. Cantor. Personal Communication, Jan. 2015.

[46] M. Croce, E. Bond, A. Hoover, G. Kunde, W. Moody, M. Rabin, D. Bennett, J. Hayes-Wehle, V. Kotsubo, D. Schmidt, *et al.*, "Integration of radioactive material with microcalorimeter detectors," *Journal of Low Temperature Physics*, vol. 176, no. 5-6, pp. 1009–1014, 2014.

[47] C. R. Bates, *Development of metallic magnetic calorimeters for nuclear safeguards applications*. PhD thesis, University of California, Berkely, 2015.

[48] A.-D. Brown, S. Bandler, R. Brekosky, J. Chervenak, E. Figueroa-Feliciano, F. Finkbeiner, N. Iyomoto, R. Kelley, C. Kilbourne, F. Porter, *et al.*, "Absorber materials for transition-edge sensor x-ray microcalorimeters," *Journal of Low Temperature Physics*, vol. 151, no. 1, pp. 413–417, 2008.

[49] R. Cantor and J. Hall, "Six-layer process for the fabrication of Nb/Al-AlO_x/Nb Josephson junction devices," *IEEE transactions on applied superconductivity*, vol. 15, no. 2, pp. 82–85, 2005.

[50] L. Le, R. Hummatov, J. Hall, R. Cantor, and STP Boyd, "Development of magnetic microcalorimeters for gamma-ray spectroscopy," *Journal of Low Temperature Physics*, vol. 184, no. 1-2, pp. 108–113, 2016.

[51] R. Hummatov, L. N. Le, J. A. Hall, S. Friedrich, R. A. Cantor, and STP Boyd, "Tantalum passive persistence shunts for on-chip current trapping in metallic magnetic calorimetry," *IEEE Transactions on Applied Superconductivity*, vol. 27, no. 4, pp. 1–5, 2017.

[52] P. Franke, D. Neuschütz, and Scientific Group Thermodata Europe, "Au-Ti (Gold-Titanium)," in *Binary Systems. Part 5: Binary Systems Supplement 1*, pp. 1–5, Springer, 2007.

[53] Heidelberg MMC Group. Personal Communication, 2009.

[54] F. Jaeckel, V. Kotsubo, J. Hall, R. Cantor, and STP Boyd, "Dedicated co-deposition system for metallic paramagnetic films," *Journal of Low Temperature Physics*, vol. 167, no. 3-4, pp. 286–291, 2012.

[55] M. Staab, F. Greiner, M. Schlosser, and H. F. Schlaak, "Applications of novel high-aspect-ratio ultrathick UV photoresist for microelectroplating," *Journal of Microelectromechanical Systems*, vol. 20, no. 4, pp. 794–796, 2011.

[56] Microchemicals GmbH, Silicon Valley, *Thick Resist Processing*, July 2013. microchemicals.com/technical_information/thick_resist_processing.pdf.

[57] STP Boyd, V. Kotsubo, R. Cantor, A. Theodorou, and J. A. Hall, "Miniature thin-film SQUID susceptometer for magnetic microcalorimetry and thermometry," *IEEE Transactions on Applied Superconductivity*, vol. 19, no. 3, pp. 697–701, 2009.

[58] R. Hummatov, *Gamma-Ray Metallic Magnetic Calorimeters with NbTa Passive Persistent Switches and Electroformed Au Absorbers*. PhD thesis, University of New Mexico, Albuquerque, 2018.

[59] STP Boyd, R. Hummatov, G. Kim, J. Hall, R. Cantor, and S. Friedrich, "Integrated squid/sensor metallic magnetic microcalorimeter for gamma-ray spectroscopy," tech. rep., Lawrence Livermore National Lab.(LLNL), Livermore, CA (United States), 2017.